Victoria University of Wellington

Masters Thesis

The ice thickness distribution of a debris-covered glacier: Tasman Glacier, New Zealand.

Author:
Rory Hart

Supervisors:
Huw Horgan
Brian Anderson
Andrew Mackintosh

A thesis submitted in partial fulfilment of the requirements for the degree of Master of Science

in the

Antarctic Research Centre
School of Geography, Environment and Earth Sciences

April 2014

Declaration of Authorship

I, Rory Hart, declare that this thesis titled, 'The ice thickness distribution of a debris-covered glacier: Tasman Glacier, New Zealand' and the work presented in it are my own. I confirm that:

- This work was done wholly or mainly while in candidature for a research degree at this University.
- Where any part of this thesis has previously been submitted for a degree or any other qualification at this University or any other institution, this has been clearly stated.
- Where I have consulted the published work of others, this is always clearly attributed.
- Where I have quoted from the work of others, the source is always given. With the exception of such quotations, this thesis is entirely my own work.
- I have acknowledged all main sources of help.
- Where the thesis is based on work done by myself jointly with others, I have made clear exactly what was done by others and what I have contributed myself.

Signed: _____

Date: _____

"Glaciers are delicate and individual things, like humans. Instability is built into them."

Will Harrison

Abstract

The ice thickness distribution of mountain valley glaciers is an important physical constraint for modelling their flow. Ice thickness measurements are used to calculate the geometry and ultimately the driving stress of a glacier. This information is all required if realistic models are to forecast the response of glaciers to climate forcings. For New Zealand's Tasman Glacier, two factors complicate its response to climate: 1) A layer of insulative rocky debris covers the lower half of the glacier, retarding surface melt, and 2) the glacier has recently entered a period of iceberg calving into a proglacial lake, introducing complex mechanical processes. These complications, along with the uncertainty of the current bed topography of the Tasman Glacier, make future predictions of its retreat behaviour difficult. The bed of the Tasman Glacier has not been fully imaged but ice thickness measurements obtained through seismic and gravity surveys have provided constraints for parts of the glacier. This study applies a range of geophysical methods (gravity and refraction seismics) to measure and model the ice thickness distribution of the lower Tasman Glacier. We surveyed orthogonal to glacier flow to obtain 12 transects within the lower 5 km of the glacier. Two-dimensional and three-dimensional gravity models generally indicate a U-shaped valley with ice thicknesses of 92–722 m from the present day terminus to the most upstream transect respectively. These results were used as input data to a simple mass flux model to assess its performance in estimating ice thickness and volume for the Tasman Glacier. The mass-flux model estimated a volume of 14.96 km^3 for the Tasman Glacier, but generally underestimated ice thickness with an RMSE of 148 m between the modelled and the gravity-derived ice thickness. This discrepancy could be reduced by constraining ice thickness for a larger area of the glacier and providing a more recent DEM to the mass flux model. Studies such as this highlight the importance of constraining ice thickness in order to improve glacio-dynamic models and global volume estimates.

Acknowledgements

One thing that surprised me when I embarked on this project was the diversity of people I would meet along the way. Many of these people have provided a part of their expertise to this final product, whether it was technical advice or simply a few suggestions. In some ways, I think this encapsulates the process of contributing a Master's thesis to science, where one adds to the great 'science stack' of ever expanding knowledge.

Firstly, I would like to thank my supervisors, Huw Horgan, Brian Anderson and Andrew Mackintosh who initially established this project in 2011. Since then, they have provided countless hours of expertise to help me complete this thesis. A 3-week fieldwork component with Huw, Brian and Gideon Geerling established the data set which made this work possible. Fieldwork was additionally supported by Mt. Cook Ski Planes who were instrumental in delivering our field gear and team onto the glacier.

A number of people generously provided their time to the data analysis component of this thesis. Euan Smith, who always has an open door, gave generous discussions on the concepts of gravity and error analysis. Many stimulating discussions around glaciology were provided by Huw, Brian and Andrew. Any technical issues I encountered with Matlab, maps or licences were supported with help from Adrian Benson and Aleksandr Beliaev while financial support was provided by Tim Stern for the gravity modelling software 'Geosoft'.

I couldn't have had a better group of office colleagues to pass the time with. Grant, Brook, Kolja, Claire and Rachel were always there to provide the banter and the occasional almond, piece of chocolate or beer to sustain me through the year. Cheers.

Lastly to my friends and family who were always there for support. Thanks for keeping me motivated and thinking about the wider scope of why I did this. And lastly, to my wonderful mum. Thank you.

Contents

List of Figures

List of Tables

Chapter 1

Introduction

1.1 Motivation

During the 20th and early 21st centuries, mountain glaciers have experienced overwhelming retreat in response to a warming climate (Alley et al., 2007). Their contribution to future sea level rise is predicted to be of the order 0.6 ± 0.07 m Sea Level Equivalent (SLE) (Radić and Hock, 2010) having the potential to contribute more to sea level rise in the coming decades than the major ice sheets of Greenland and Antarctica (Meier et al., 2007). Other estimates of 0.43 ± 0.06 m SLE from Huss and Farinotti (2012) and 0.35 ± 0.07 m SLE from Grinsted (2013), indicate that there are significant uncertainties associated with calculating this contribution.

In regions such as New Zealand, where tourism and hydroelectric power generation are important economic assets, glaciers also display a net retreat pattern (Dykes and Brook, 2010; Chinn et al., 2012). Many of New Zealand's large, debris covered glaciers are presently calving into proglacial lakes (Dykes et al., 2010; Quincey and Glasser, 2009) decreasing the long-term storage of ice. In scenarios where climate change is expected to exacerbate current stresses on water resources, knowledge of the ice thickness and total ice volume of these debris-covered glaciers is critical to the future management of glacial catchments.

When direct observations are unavailable, glacier volume changes are calculated using scaling relations or ice-dynamical relationships. These changes have been calibrated using several hundred ice-thickness measurements (Alley et al., 2007), but of the 170,000 glaciers worldwide, this small subset of ice-thickness information means that uncertainties remain large (Grinsted, 2013). Additionally, ice-thickness measurements are biased towards clean-surface glaciers which are small and/or easily accessible. Given that a large proportion of the world's glaciers are debris-covered or tidewater-calving, their total volume remains uncertain due to the lack of direct ice-thickness measurements (Radić and Hock, 2010; Yde and Paasche, 2010).

This study is motivated by the current uncertainties involved with calculating the ice thickness and volume of temperate valley glaciers, in particular, debris-covered glaciers. To address these issues on a local scale, I focus on the debris-covered Tasman Glacier in New Zealand. Here I explore the ice-thickness distribution of the glacier using geophysical methods and compare these results to other ice volume estimates for the Tasman Glacier. This chapter explores (1) the regional setting of the Tasman Glacier, (2) the glacial processes which require knowledge of ice thickness and (3) the techniques available for estimating ice volume. I then identify the questions to be answered in this study in a series of research objectives.

1.2 Regional Setting

New Zealand lies on an active plate boundary between the Pacific and Australian plates (Walcott, 1998). The plate convergence has a narrow band of NNE-SSW compression marked by the Alpine Fault and other faults (Norris and Cooper, 2001) which has subsequently formed the Southern Alps. This 700 km-long, $\simeq$ 2500-m high orographic boundary intercepts the dominant westerly atmospheric circulation (Sturman and Tapper, 2006). Moist air which flows regularly across this boundary generates a high precipitation band for the Mt. Cook region. Annual precipitation in the Mt. Cook climate station is monitored by the National

Institute of Water and Atmospheric research (NIWA) and has a mean annual rate of 4127 ± 913 mm/year (for the period 1930-2012). The mean temperature here is 8.6 °C ± 5.2 °C and shows an increasing trend of 1.3 °C/100 years for the same period.

The Tasman Glacier is in the centre of Aoraki/Mt Cook National Park, located at 43.62 °S, 170.21 °E. The main trunk flows south from a névé at 2500 m to a terminus elevation of ∼ 740 m where it terminates into a proglacial lake. It is fed by a number of large tributaries, namely the Rudolf, Darwin, Hochstetter and Ball Glaciers (Figure 1.1) (Anderton, 1973). The geology surrounding the glacier is dominated by Mesozoic aged sandstones and argillites which are intensely faulted and jointed (Cox and Findlay, 1995; Cox and Barrell, 2007; Rattenbury et al., 2010; Tenzer et al., 2011). It is these weaknesses in the rock which allow frequent rockfalls and occasionally, rock avalanches to cover the surface of the lower Tasman Glacier (Kirkbride and Warren, 1999). This results in an irregular but extensive debris cover over the glacier (Figure 1.1) (Kirkbride, 1993; Benn et al., 2003).

Like many glaciers in the Southern Alps, the Tasman Glacier is in a state of negative mass-balance. The retreat history of the glacier has been characterised by three phases (Kirkbride, 1993). Surface lowering was first documented, initially by Skinner (1964) who observed an 82 m decrease in the elevation of the glacier over a 72 year period since observations began by Brodrick in 1891. The second phase commenced in the 1970's where thermokarst ponds developed surrounding areas of conduit collapse; these soon merged into a series of interconnected ponds and eventually, a proglacial lake. By 1991 terminus calving had initiated into the proglacial lake which led to rapid retreat of the terminus (Kirkbride and Warren, 1999). Despite calving being the dominant mechanism for ice loss near the terminus (Purdie and Fitzharris, 1999), surface lowering is still the major contributor to ice loss (80%) for the Tasman Glacier (Quincey and Glasser, 2009).

Predictions of future retreat for the Tasman Glacier are complicated by a number of glacio-dynamic features which require knowledge of ice thickness. The following section outlines the general theory of glacio-dynamic features which are significant for the Tasman Glacier.

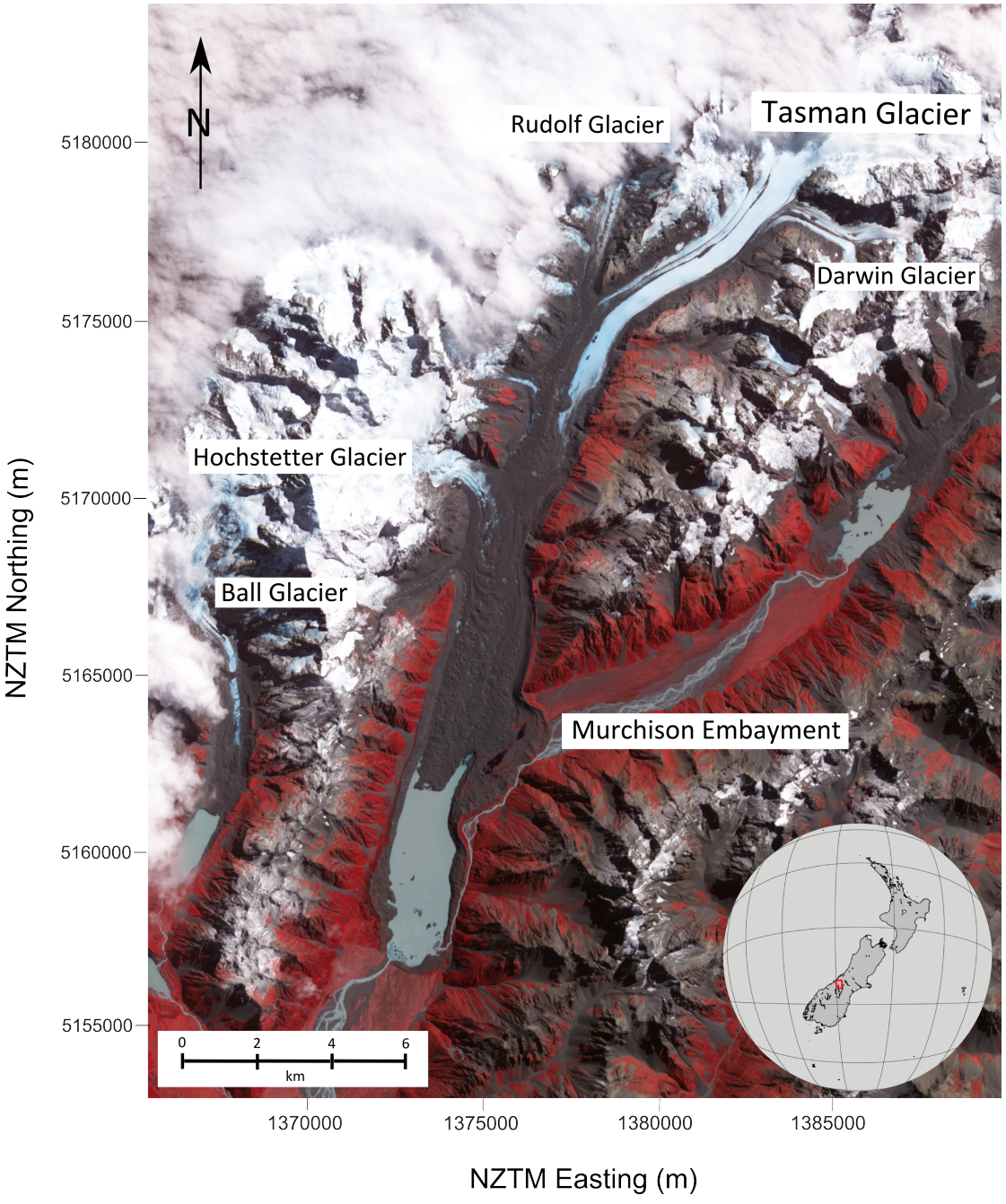

FIGURE 1.1: Map of the Tasman Glacier (March 2, 2011 - Aster image). The main trunk is visible by clean ice in the north-east, which becomes progressively debris-covered to the south. Inset indicates the location of the Tasman Glacier by the red box in the central South Island.

1.3 Glacier Dynamics

1.3.1 Glacier Flow

The term 'glacier dynamics' encompasses the processes which control glacier flow. Under the force of gravity, glaciers flow from the accumulation zone to the ablation zone by three mechanisms; sliding over the bed, deformation of sub-glacial material and internal deformation of the ice (Figure 1.2) (Cuffey and Paterson, 2010).

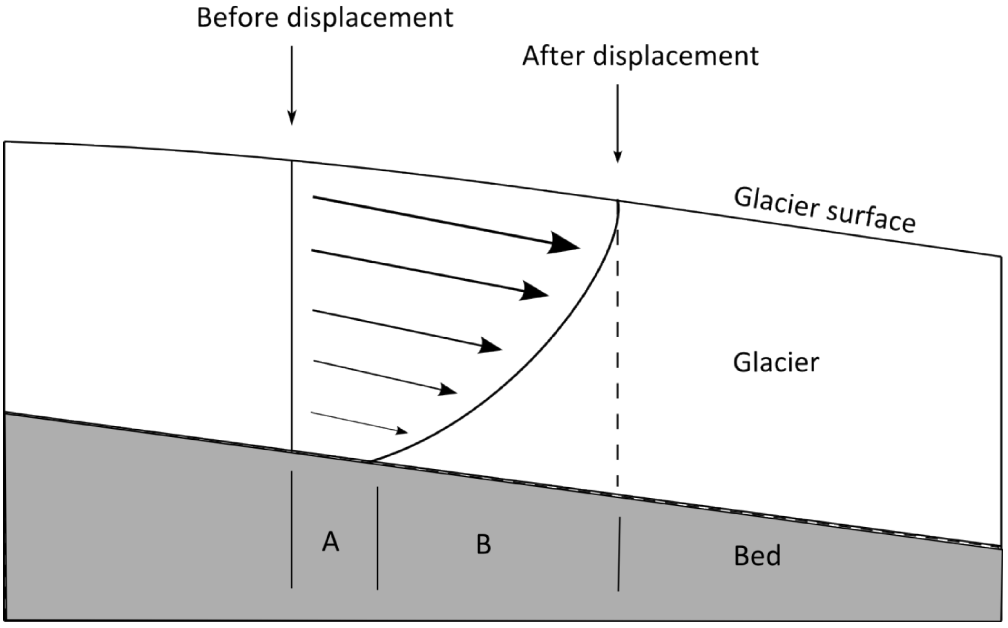

FIGURE 1.2: Components of glacier flow divided into (A) basal slip and (B) internal deformation. Down-facing arrows indicate the initial and final positions of a point on the glacier which has been displaced. Arrows within the glacier represent velocity. Figure adapted from Hambrey and Glasser (1978).

The equations which describe glacier flow result from the stresses which act on a glacier. To a first-approximation, glaciers in a steady-state of flow have a driving stress equal to the resisting stress (imposed by the base and sides of a glacier) and the longitudinal stress (Cuffey and Paterson, 2010). The driving stress (τ_d) is proportional to the surface slope (α) and the thickness (H) of the glacier:

$$\tau_d = \rho g H \alpha \tag{1.1}$$

where ρ is the density of ice and g is the force due to gravity (Cuffey and Paterson, 2010). The largest resisting stress is the basal drag, which is approximately equal and opposite to the driving stress:

$$\tau_b = f'\tau_d \tag{1.2}$$

where f' denotes a constant close to one. (For the full derivation of this relationship see Cuffey and Paterson (2010)).

The driving stress is a function of the ice thickness, the density of ice and the surface slope of a glacier (equation 1.1). How the ice deforms or flows in response to the driving stress depends on a few boundary conditions such as the basal drag, and the properties of the ice, however, these features will not be explored here. The following sections outline significant glacial processes that require knowledge of ice thickness.

1.3.2 Glacier bed

The nature of the bed has implications for the dynamics of glacier flow. In highly erosive valley glacier systems, the glacier bed can become over-deepened as a result of rapid sub-glacial erosion (Bennett and Evans, 2012). Typically, lower and thus warmer regions of a glacier exhibit over-deepened channels due to the presence of surface melt-water reaching the bed and aiding erosion (Alley et al., 2003b). In regions of over-deepening, beds also exhibit a steep reverse slope to the ice-air interface. At the steepened glacier/sediment interface, ice growth from super-cooling impedes flow thus decreasing sediment-transport capacity and favouring deposition (Figure 1.3). Through a positive-feedback, the mechanism of 'glacio-hydraulic supercooling' proposed by Alley et al. (2003a) suggests that beds of reverse slope to and 20-70 % steeper than the ice/air interface allow the supercooling of sub-glacial waters as they migrate up the bed slope, thus freezing conduits which would normally enable sediment transport. Hence, a form of 'glacial progradation' is observed by the progressive deposition of sediment onto the reverse slope.

The glacier bed has important controls on the stability of a glacier due to the resisting stresses it imposes on the ice, as well as heterogeneous features such as pinning points which can act to stabilise glacier fronts (Warren, 1991). Additionally, it has been shown that glaciers in a stage of terminus calving into water may enter a phase of unstable retreat if the bed deepens up-glacier (Bassis and Jacobs, 2013). For the Tasman Glacier, ice-thickness studies are sparse but values between 535 to 725 m adjacent to Ball Glacier (Figure 1.1) indicate that the bed may be over-deepened here (Broadbent, 1973). Bathymetric surveys near the terminus which indicate depths of up to 240 m (Dykes et al., 2010), suggest that the glacier shallows significantly between Ball Glacier and the terminus. Insights into the nature of the bed are sparse, but studies indicate that a till layer 100 – 200 m thick exists beneath the Tasman Glacier (Broadbent, 1973). South of the present-day terminus, till up to 620 m thick has been observed to occupy the Pukaki Valley (Kleffmann et al., 1998).

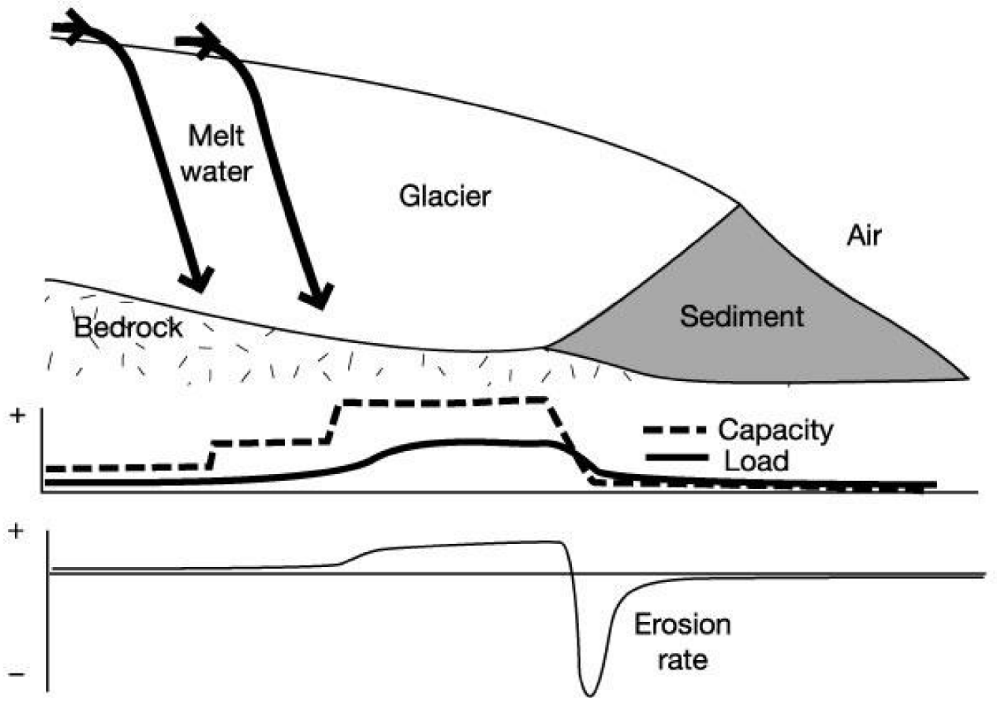

FIGURE 1.3: Schematic of the sediment-transport capacity and sediment load for a glacier exhibiting super-cooling. Figure courtesy of Alley et al. (2003a).

1.3.3 Debris cover

The response of a glacier to climate variations is partially influenced by the amount of surface debris cover. Models exploring the relationship between debris thickness and ablation rates show that for short-term temperature oscillations a thin debris cover (< 2.0 cm) enhances ablation (Reid et al., 2012). However, for glacier surfaces covered in a uniform (> 5.0 cm) thickness of debris, a net insulating effect is exerted on the underlying ice, thus ablation is reduced (Benn et al., 2003). Over seasonal and inter-annual time periods, long term temperature changes are propagated at depth through the debris layer (Bozhinskiy et al., 1986). For debris-covered glaciers, debris thickness generally increases towards the terminus, thus reducing ablation rates down valley. Consequently, debris-covered glaciers typically have a reversed ablation gradient (Figure 1.4) (Benn et al., 2012). A surface debris layer can result in (1) down-wasting of the ice surface, (2) a transition from a convex to a concave glacier profile, (3) a reduced glacier gradient and (4) the development of supra-glacial ponds, for glaciers in a state of negative mass balance (Purdie and Fitzharris, 1999; Röhl, 2008; Dykes and Brook, 2010).

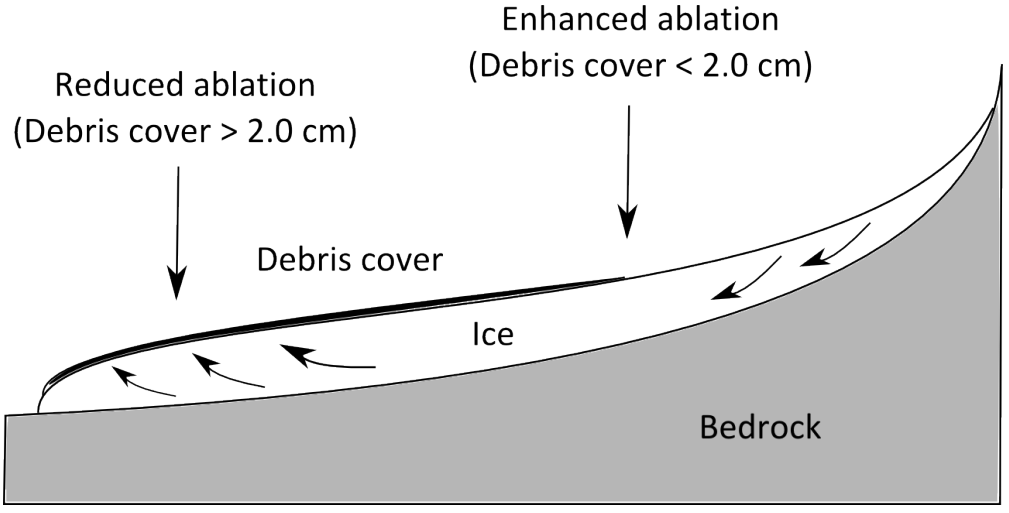

FIGURE 1.4: Reversed ablation gradient due to the effects of debris cover. Curved arrows represent the direction of ice motion in a glacier.

Glaciological observations since 1862 by von Haast and later mapping by Brodrick (1890) indicate that the Tasman Glacier has always had a significant debris cover over its lower extent. During the 20th and early 21st centuries, the glacier surface has been subjected to vertical lowering, resulting in a shallowed surface gradient and the transition from a convex to a concave surface profile (Kirkbride and Warren, 1999). Surface lowering was not associated with a change in terminus position until the early 1980's, at which point several thermokarst ponds developed and eventually coalesced into a proglacial lake (Kirkbride and Warren, 1999). The modern surface of the glacier continues to down-waste. Evidence of this lowering is exemplified by bare ice cliffs which exhibit small thermokarst ponds or drainage networks at their base (Figure 1.5) (Redpath, 2011; Vivero et al., 2013). The effect of debris cover on the sensitivity of ice-thickness changes is explored in more detail in section 3.3.2.

1.3.4 Calving

Calving is an important mechanism for ice loss and can be a more effective mass loss mechanism than surface ablation (Van der Veen, 2002). Many studies have investigated the processes which drive terminus calving; (e.g. crevasse-induced calving through high velocity gradients (Benn et al., 2007), thermo-erosional notch development (Röhl, 2006) or the relationship between calving rate and water depth (Dykes and Brook, 2010)).

To a first-order, longitudinal strain rates at the terminus of a glacier are responsible for yielding fractures in the ice. It is these fractures which provide the dominant mechanism for calving (Benn et al., 2007). Second-order processes including thermal notch development or buoyancy forces acting on sub-aqueous ice-tongues are typically super-imposed on top of this dominating trend. For particularly slow moving glaciers, these second-order processes may indeed become more dominant, such as in marine and lacustrine settings, where a glacier terminus calves into water. It is also common for glaciers in lacustrine settings to have a remnant sub-aqueous ice-foot following sub-aerial calving which, under unstable

FIGURE 1.5: An extensive debris cover over the lower Tasman Glacier. Note also the presence of an englacial tunnel exposed at the surface.

buoyant forces, will itself eventually calve (Figure 1.6). In particular, Mercer (1961) showed that calving rate and water depth are correlated for tide-water glaciers, indicating that retreat rates may be influenced by water depth. This relationship has also been observed in lacustrine settings like the Tasman Glacier (e.g. Dykes and Brook (2010)). Where glacial channels are over-deepened, the likelihood of terminus calving is thought to be enhanced if a glacier progressively retreats up-valley into a deeper channel. This would typically occur when the bed of the glacier has a reverse slope.

The future retreat, likely due to terminus calving, at Tasman Glacier is not well understood. Kirkbride and Warren (1999) established two different scenarios for terminus calving involving a slow-retreat and fast-retreat scenario. Fast retreat estimates were based on a linear relationship between calving rate and water depth

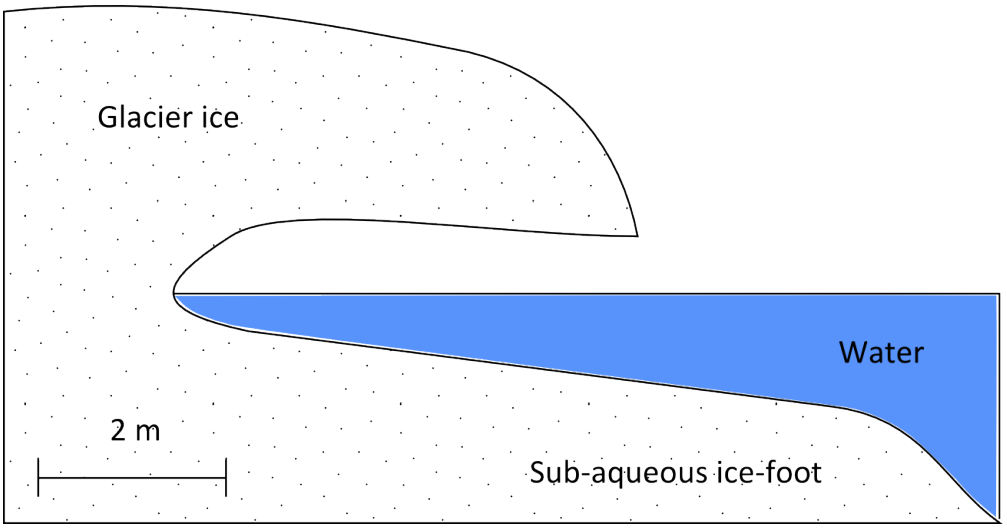

FIGURE 1.6: Secondary calving processes such as notch development destabilising the terminus of a glacier. Figure adapted from Röhl (2006).

while the slow retreat scenario assumed that only waterline melting contributed significantly to terminus calving. Recent studies by Dykes and Brook (2010) have investigated lake depth in an attempt to predict future retreat rates based on the fast-retreat scenario. In its current state, the Tasman Glacier is retreating primarily through terminus calving and has been since 1991 (Hochstein et al., 1995). In February 2013, the most recent calving event was captured through time-lapse photography (Figure 1.7).

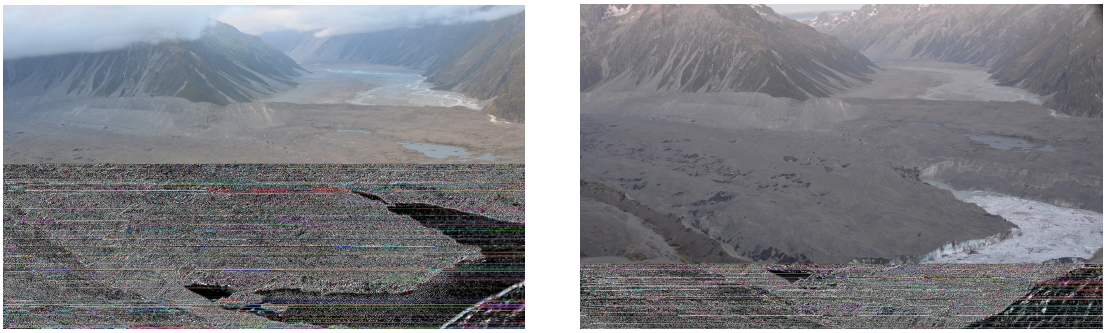

(a) Pre calving (22/02/2013) (b) Post calving (23/02/2013)

FIGURE 1.7: February calving event at the Tasman Glacier terminus. Photos courtesy of Brian Anderson.

1.4 Estimating glacier volumes

One of the present uncertainties faced in glaciology involves calculating the total volume of the world's glaciers (Farinotti et al., 2009; Huss and Farinotti, 2012). Of the 170,000 glaciers worldwide, only a small number have had their volume constrained through direct ice-thickness measurements (Nolan et al., 1995; Leclercq et al., 2011; Farinotti and Huss, 2013). Moreover, ice-thickness data is limited to point measurements or 2D cross sections which are then interpolated to obtain ice volume (Farinotti et al., 2009). Ice-thickness measurements are typically obtained through geophysical methods which are often arduous to collect and cannot be easily extrapolated (e.g. Watson (1995); Dowdeswell et al. (2002)). For glaciers without ice-thickness information, the total ice volume is often obtained through empirical formulae (Bahr et al., 1997; Chen and Ohmura, 1990) which relate the surface characteristics of a glacier to its volume. A variety of approaches have been used to estimate glacier volumes without the use of ice-thickness information. These approaches include:

1. Perfect-plasticity assumption
2. Area-volume scaling
3. Glacier mass turnover and principles of ice-flow mechanics

The following subsections outline the current methods used to estimate the ice volume of glaciers.

1.4.1 Perfect-plasticity assumption

Nye's (1952) theory states that the ice thickness can be estimated using the perfect-plasticity assumption. Consider a 2-dimensional slab of ice resting on a slope (α) whereby the length and width of the slab are large compared with the thickness (h) (Figure 1.8). Assuming that large valley glaciers have a low surface slope, the

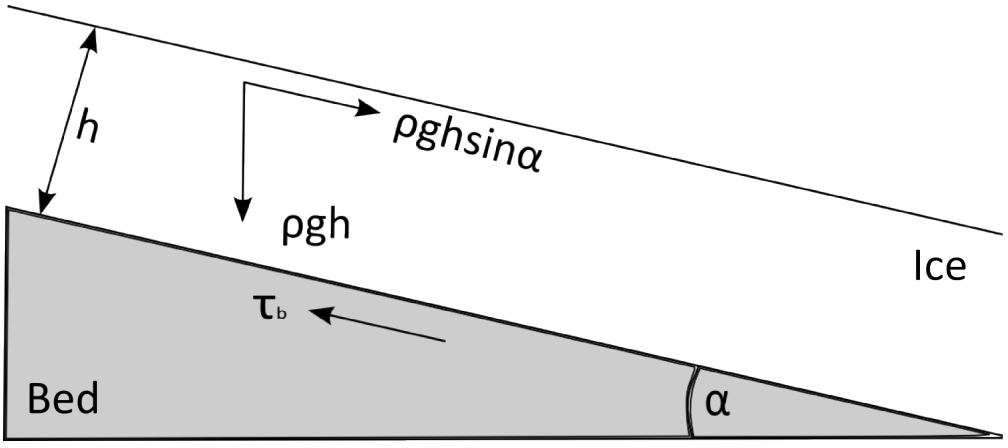

FIGURE 1.8: Cross section of an ideal glacier, (parallel sided slab) representing the perfect plasticity model. Under the perfect-plasticity assumption, τ_b is equal to τ_0 ($\rho ghsin\alpha$).

thickness of the column in the vertical component is approximately the same as the true thickness. Hence the weight of the column in the vertical component is given by (ρgh) while the weight component parallel to the slope represents the driving stress ($\rho ghsin\alpha$). The driving stress is opposed by the basal drag of the slope (τ_b). The perfect-plasticity theory assumes that the basal shear stress (τ_b) is equal to the constant yield stress for ice (τ_0) which is on the order of 100 kPa (Cuffey and Paterson, 2010). Thus the ice thickness is given by Equation (1.3):

$$h = \frac{\tau_b}{\rho g sin\alpha} \tag{1.3}$$

The standard perfect-plasticity model ignores boundary conditions such as side drag imposed by the valley walls. Additionally, the model requires no information about the mass balance of the glacier, although the main assumption that the basal shear stress is equal to the yield stress, implies that the glacier is in a steady state of mass balance (Clarke et al., 2009).

More recent work by Li et al. (2012) on the perfect-plasticity model considers the width of the glacier cross-section and therefore the additional drag forces imposed on the glacier. Given this adaptation, the extended perfect-plasticity

model is more rigorous, yet still simple compared to other methods in that it only requires glacier geometry and an assumed yield stress as inputs.

1.4.2 Area-volume scaling

The area-volume scaling method works on the simple assumption that the volume (V) of a glacier is proportional to its surface area (A) governed by a power relationship:

$$V = c \cdot A^{\gamma} \tag{1.4}$$

where c and γ are empirical constants derived from direct measurements of volume and area (Bahr et al., 1997; Chen and Ohmura, 1990). In essence, equation (1.4) takes information about the surface boundary of a glacier and extrapolates it to estimate the average thickness of the ice (Bahr and Radic, 2012).

The area-volume scaling method is justified by its ability to overcome random errors in individual glaciers due to the large sample set of glaciers typically used (Bahr and Radic, 2012). Its precision can be increased by using additional parameters in the regression between area and volume (Grinsted, 2013). As a result, this method is useful for estimating global volumes of ice rather than individual glacier volumes. Limitations in the scaling method arise from the lack of surface geometry information or climate setting for an individual glacier. Moreover, the scaling method does not consider the ice-thickness distribution of an individual glacier which is a first-order constraint for glacio-dynamic models (Huss and Farinotti, 2012).

1.4.3 Recent methods

Recent developments in estimating glacier volumes have come from a variety of sources (e.g. Clarke et al. (2009); Farinotti et al. (2009); Huss and Farinotti (2012)). Unlike the perfect plasticity and area-volume scaling methods, the goal of recent

methods has been to calculate the volume of a glacier by using ice-thickness data where available. Clarke et al. (2009) used artificial neural networks to simulate sub-glacial topography based on neighbouring ice-free topography. Farinotti et al. (2009) and Huss and Farinotti (2012) used a physics-based approach to solve for the ice-thickness distribution and overall ice volume of a glacier. In particular, Farinotti et al. (2009) used a method based on glacier mass turnover and principles of ice-flow mechanics to calculate the ice-thickness distribution of four alpine glaciers, all of which had direct ice-thickness data available for model validation. Huss and Farinotti (2012) developed this method further using digital elevation models and glacier outlines from the Randolph Glacier Inventory to solve for the total ice volume of glaciers worldwide (Arendt et al., 2012).

Farinotti et al.'s method for estimating the ice thickness distribution of the Tasman Glacier provides a robust comparison for the results obtained in this study. In particular, a simplified mass flux model based on Farinotti et al.'s method is used to estimate the ice thickness distribution of the Tasman Glacier. The results from this study are used to evaluate the model outputs of ice thickness and tune physical constants in the mass flux model in Chapter 3 and later compared to Farinotti et al. (2009)'s result for the ice-thickness distribution of the Tasman Glacier in Chapter 4.

1.5 Research questions and objectives

The ice-thickness distribution for glaciers is generally poorly known and is an important first-order physical constraint for estimating glacier volumes. The objective of this study is to improve our understanding on the ice-thickness distribution of the lower Tasman Glacier. Below, I list the research questions and corresponding objectives for this project.

Question 1: What is the ice-thickness distribution on the lower part of Tasman Glacier?

This question will be answered by producing two-dimensional (2D) and three-dimensional (3D) gravity models of the lower Tasman Glacier, constrained where possible by seismic methods and previous geophysical surveys, to estimate the ice-thickness distribution and bed topography of the lower Tasman Glacier.

Question 2: How do my ice-thickness measurements for the Tasman Glacier compare to estimates made using a simple mass flux model?

This question will be answered by applying an ice flux model to the Tasman Glacier and evaluating its performance using gravity derived ice-thickness measurements.

To address these questions, the chapters will be arranged as follows:

Chapter 2 describes the methodology of this study. This chapter summarises the theoretical basis behind gravity and seismic methods, encompassing appropriate field applications used in this study. It also highlights the theoretical background of the mass flux model used to estimate ice thickness for the Tasman Glacier.

Chapter 3 explores the results of the ice-thickness distribution of the Tasman Glacier through two- (2D) and three-dimensional (3D) gravity models. First I explore the sensitivity of ice thickness to changes in density and till thickness using a suite of 2D synthetic models. Forward and inverse (2D and 3D) gravity models are then presented for the Tasman Glacier. These models are constrained where possible by additional geophysical methods such as a seismic refraction survey and past geophysical studies. The mass flux model results are also evaluated with respect to the gravity derived ice thickness results.

Chapter 4 summarises the ice-thickness distribution of the Tasman Glacier by comparing 2D and 3D gravity models and analysing anomalous features in the 2D models. Limitations in the geophysical methods used and in the mass flux model are then highlighted. I then explore the implications of bed topography on future retreat with respect to glacier models before suggesting avenues for future research.

Chapter 2

Methodology: Geophysical theory and field applications

2.1 Introduction

Gravity prospecting methods use subtle changes (1 part in 10^5 to 10^6) in the Earth's gravitational field to infer density variations within the subsurface (Reynolds, 2011). The gravity method takes measurements across an area of interest and subtracts the gravitational effect of an idealised Earth (addressing changes in latitude, elevation and topography) leaving a Bouguer anomaly representative of the entire subsurface (e.g. Claridge (1983)). Bouguer anomalies can be reduced to residual anomalies to investigate shallow regions of the subsurface.

Refraction seismology is an additional method used here to measure the velocity of subsurface layers and constrain their density. This is beneficial for gravity modelling where geological models require realistic densities in order to match the residual anomaly (e.g. Stern (1978)).

Here, the gravity method is used to investigate the ice-thickness distribution of the lower Tasman Glacier, constrained locally by a seismic refraction survey. Residual anomalies are modelled in order to investigate the shape and thickness of the lower Tasman Glacier. Due to the high density contrast between the ice and basement

rock, the residual anomalies are large (-24 mGal). This chapter outlines the field methods used and the theory of seismic refraction and gravity with application to our data.

2.2 Field methods

Fieldwork for this study was carried out over a three week period in January and February, 2013. The fieldwork incorporated active-source seismic, gravity and Global Positioning System (GPS) methods over the lower section of the Tasman Glacier. A temporary camp was also established as a gravity base station in the centre of the glacier approximately east of Ball Hut (Figure 2.1). The following sections outline the survey designs used in this study.

2.2.1 Seismics

A refraction seismic survey was conducted to investigate the velocity structure of the surface debris cover, glacier ice and bed. The refraction line was established orthogonal to glacier flow near the camp-site/base station (Figure 2.1); this location was chosen to match independent surveys by Anderton (1973) and Broadbent (1973). A 230 m long, 24 channel spread (at 10 m spacing) was surveyed three times across the glacier, encompassing a total survey length of 690 m. A record length of 1 second was used at a sample interval of 0.125 seconds. The operator made 5 blows per stack using a 5 lb sledgehammer on a well-secured boulder.

2.2.2 Gravity

A LaCoste & Romberg gravimeter (model G 179) was used to conduct the gravity survey. A total of 189 stations were occupied between January 24 and February 8 2013, under fine conditions. (Sunny, with wind <5 kts 95% of the time). The survey was composed of 10 linear transects (L_100 to L_1000) spaced 500 m apart,

perpendicular to the main flow of the glacier. Two additional transects (T_100 and T_200) were also surveyed near the terminus of the glacier (Figure 2.1). Transects were composed of stations, spaced at 100 m intervals along each transect where three consistent gravity measurements were made. The base station was occupied every morning and evening ($\sim$ 12 hr intervals) at the temporary camp established in the centre of the glacier.

2.2.3 GPS

A Trimble GeoXH GPS unit was used with a dual frequency zephyr antenna to observe surface elevation across the glacier surface. The mobile set-up included a 1-m-long rod attached to the antenna at a height of 1.52 m or 1.82 m depending on the surveyor. Elevations were used to update DEM changes related to glacier down-wasting and to validate terrain corrections made by the surveyor (see section 2.5.6).

2.3 Physical basis of seismic refraction

The seismic refraction method is based on principles of wave-propagation across boundaries of varying refractive indices (Reynolds, 2011). It is commonly applied to geological problems to investigate the depth to a layer and/or the velocity within a layer (e.g. Bentley (1973); Booth et al. (2013)). Typical refraction surveys involve an active energy source (sledgehammer) and a string of recording devices (geophones). The source generates seismic waves which follow paths according to the density of the subsurface layers while the geophones record the arrival of these waves. Snell's Law describes the path of a wave through a variable set of media by:

$$\frac{\sin(i)}{\sin(r)} = \frac{V_1}{V_2} \tag{2.1}$$

where i describes the angle of incidence of a wave and r describes the angle of refraction. V_1 and V_2 are the velocities in the upper and lower layers respectively.

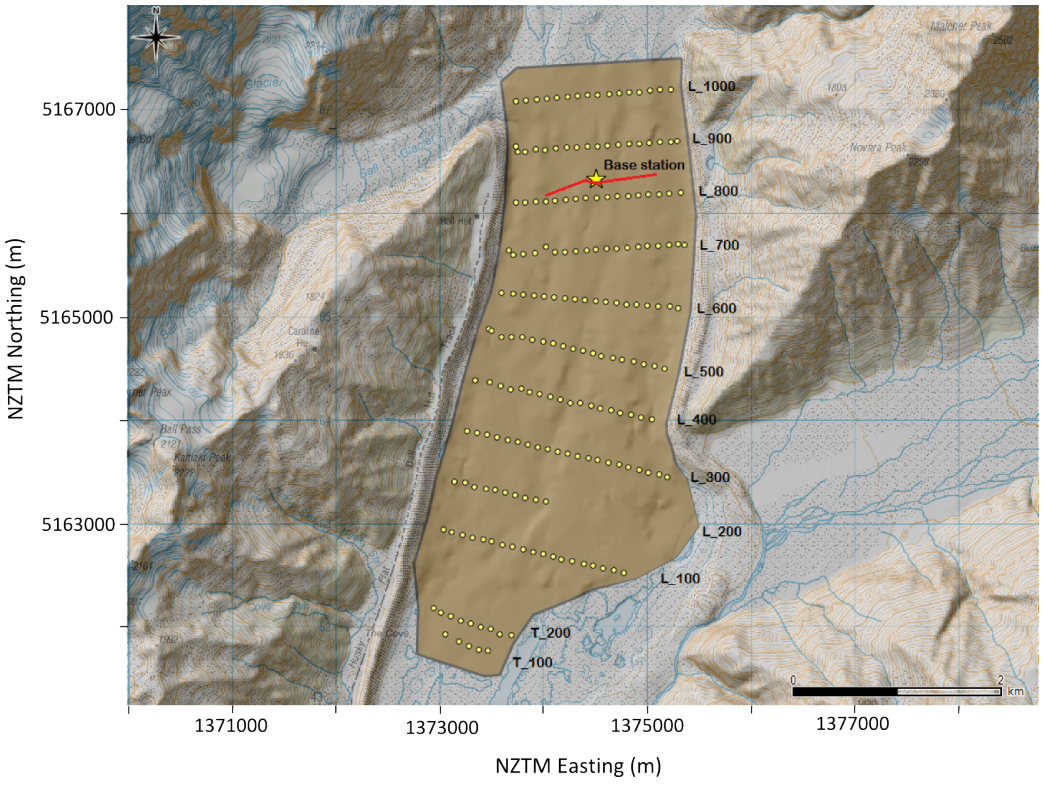

FIGURE 2.1: Location of the gravity survey points (yellow circles) and refraction seismic line (red) over the lower Tasman Glacier. The gravity base station (yellow star) also marks the temporary camp occupied during fieldwork.

Snell's Law describes the refraction path of a wave due to an increase in density of a medium. Generally, density and wave velocity increase with depth. A threshold depth is met when a wave propagates parallel to a refractive boundary; this is known as critical refraction. Critical refraction occurs at the critical angle (i_c), a condition at which the angle of incidence is large enough to allow the refraction of a wave along a boundary (Figure 2.2).

The seismic refraction method was used here to constrain the velocity and density of the surface debris cover and glacier ice. This is achieved through empirical relationships between velocity and density (e.g. Bentley (1973)). Constraining the density of these layers allows tighter constraints on the gravity models to be made.

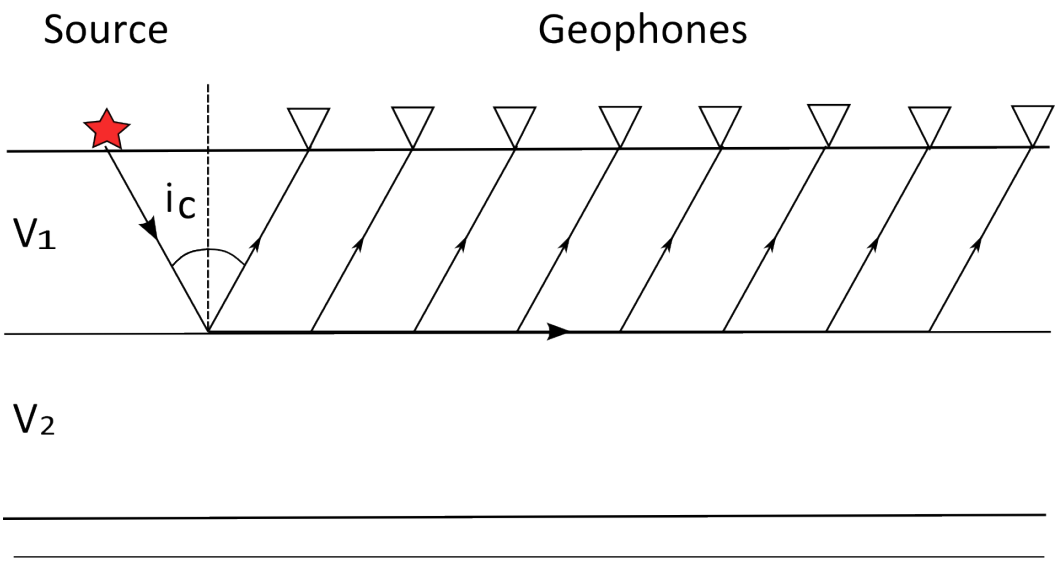

FIGURE 2.2: A typical refraction survey in cross section. An active source (red star) generates seismic waves. Inverted triangles represent a string of geophones.

2.3.1 Tasman Glacier refraction survey

The aim of the refraction survey was to constrain the velocities of the surface debris cover, glacier ice and ideally, the sub-glacial bed. Due to the size of the source (5 lb sledgehammer) and a small spread of geophones (24 channel at 10 m spacing), only the surface debris and glacier ice were observed in the shot gather (Figure 2.3). Data were processed in *Globe Claritas* and picks were made on the first breaks of each trace. Figure 2.4 indicates three horizons that were picked in between two distinct slope breaks, located at $\sim$ 35 ms and $\sim$ 45 ms. Three slopes, located between $0 - 35$ ms, $35 - 45$ ms and $45 - 110$ ms, are interpreted to represent the air wave (298 ± 38 ms^{-1}), debris layer (562 ± 333 ms^{-1}) and ice (3854 ± 56 ms^{-1}) respectively. Linear regression was used to fit the gradients of each line while uncertainties in these gradients are quoted to a 95% confidence interval (CI). Table 2.1 summarises the picked gradients and associated velocities for each wave.

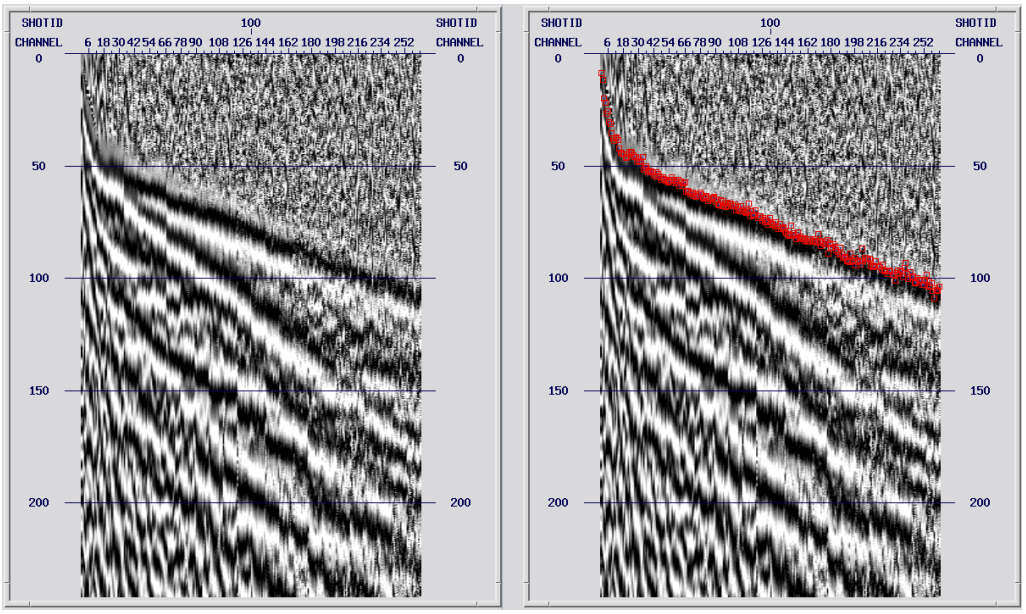

FIGURE 2.3: Offset sorted gather recorded across the Tasman Glacier showing pre-picked (left) and post-picked horizons (right). An AGC filter (window = 20 ms) has been applied for display purposes. Y axes are in units of ms (travel time) and x axes represent channel number (spacing between channels is 10 m).

TABLE 2.1: Refraction data summarised from Figure 2.4. Three distinct changes in gradient mark the air wave, debris cover and ice velocities which are fitted using linear regression. Uncertainties in the gradient, y-intercept and velocity are quoted to a 95% confidence interval (C.I.) using methods from Taylor (1997).

Waveform	**Grad ± 95% C.I.** 10^{-4}	**Y-int ± 95% C.I.** 10^{-4}	$\boldsymbol{V_p}$ **± 95% C.I.** ms^{-1}
Airwave	3.36 ±0.43	7.92 ± 2.61	298 ± 38
Debris	1.78 ±1.06	16.15 ± 14.17	562 ± 333
Ice	$0.26 \pm 4 \times 10^{-3}$	42.93 ± 0.53	3854 ± 56

2.3.2 Velocity/density conversions

The velocity of a seismic wave is a function of the density (ρ) of the material it travels through Fowler (2005). For primary waves (V_p), the velocity is also a function of the material's bulk and shear moduli, given by:

$$V_p = \sqrt{\frac{K + \frac{4}{3}\mu}{\rho}} \tag{2.2}$$

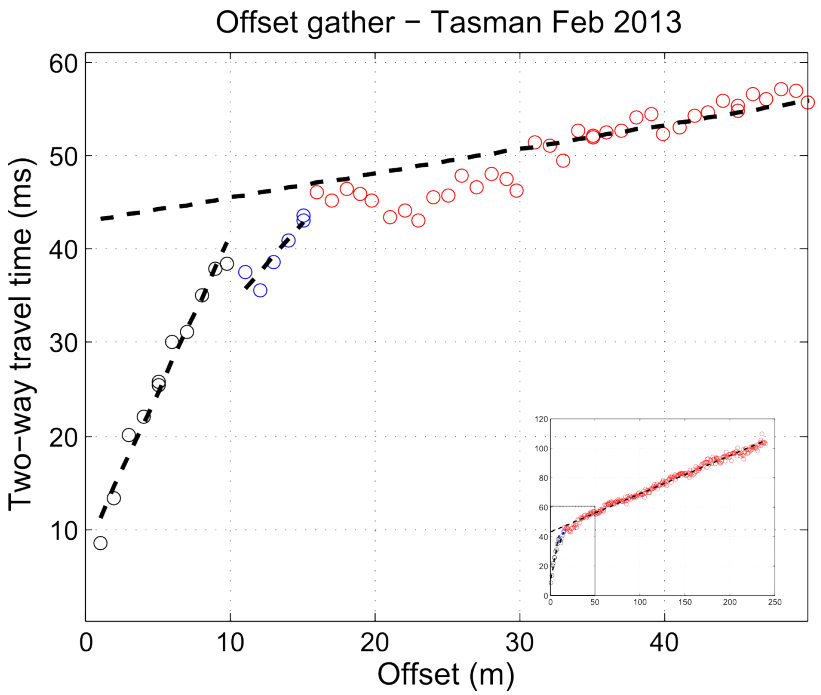

FIGURE 2.4: Direct (black circles), first refracted (blue circles) and second refracted (red circles) rays for the Tasman Glacier. Linear regression fits (dashed lines) have been applied to the data. Inset of total refraction line is shown on the bottom right.

where K is the bulk modulus and μ is the shear modulus of a material. However, for practical applications, the dependence of elastic moduli on density is not well established, hence empirical relationships have been developed to relate the velocity of a material to its density (e.g. Birch (1961); Bentley (1973); Gardner et al. (1974)).

Debris density

The density of debris cover is calculated using an empirical relationship developed by Gardner et al. (1974). The estimate is complicated due to the poorly sorted nature of the deposit. The deposit is composed primarily of Greywacke which has an average density of 2639 kgm^{-3} $\pm$ 100 kgm^{-3} (Tenzer et al., 2011). However, due to the amount of air space in the deposit, the refracted velocity of 562 ms^{-1}

$\pm$ 333 ms^{-1} (Table 2.1) indicates a lower density of 1500 $\pm$ 200 kgm^{-3} according to Gardner's relation:

$$\rho = \alpha V_p^{\beta} \tag{2.3}$$

where ρ has units of gcm^{-3}, V_p has units of fts^{-1} and α and β are empirically derived constants dependent on the local geology. In the absence of density data, a good estimate of density is obtained by taking $\alpha = 0.23$ and $\beta = 0.25$ (Gardner et al., 1974).

Debris thickness

Debris thickness (h) can be calculated in two different ways (Stein and Wysession, 2003). Both use the velocities of the first refracted (V_1) and second refracted (V_2) waves, which represent debris cover and ice respectively. The first approach calculates depth using the intercept time (τ) and is given by:

$$h_1 = \frac{\tau}{2 * \sqrt{\frac{1}{V_1^2} - \frac{1}{V_2^2}}} \tag{2.4}$$

The second approach uses the crossover distance (X_d) of 17.6 m (see Figure 2.4 and is given by:

$$h_2 = \frac{X_d}{2 * \sqrt{\frac{V_2+V_1}{V_2-V_1}}} \tag{2.5}$$

Equation 2.4 produces a depth of 4.6 m while equation 2.5 gives a depth of 7.6 m. These measurements provide a thickness for the debris which includes, for example, the remains of rock avalanche material from the 1991 Mt. Cook avalanche (McSaveney, 2002) or eroded material from the moraine sides.

Ice density

For seismic studies on ice, empirical relationships are complicated by heterogeneous features in the material such as fluids and pore spaces (e.g. Gardner et al. (1974); Booth et al. (2013)). This is also likely for the Tasman Glacier where the entrainment of debris or presence of conduits/water in the ice can alter the observed velocity. An empirical relationship proposed by Bentley (1973) has been used in several ice studies (e.g. King and Jarvis (2007); Rege and Godio (2011)):

$$\rho = (0.239 \pm 0.002)V_p - 0.002 \pm 0.009 \tag{2.6}$$

where ρ is the density (kgm^{-3}) and V_p is the velocity of the ice (ms^{-1}). To constrain the density of ice for the Tasman Glacier, p-wave velocities of 3854 ± 56 ms^{-1} obtained from Table 2.1 are used in equation 2.6. A density range of 919 ± 16 kgm^{-3} agrees within error for the density of polar ice studies e.g. Bentley (1973) as well as that for pure ice (917 kgm^{-3}). Ice thickness could not be obtained from this refraction survey as no refractions were observed at the glacier bed.

The density and thickness results obtained from this section will be used to constrain two and three-dimensional gravity models in Chapter 3.

2.4 Physical basis of gravity methods

Gravity is a universal phenomenon described as the attractive force between two objects. This force is proportional to the mass of two objects and inversely proportional to the square of the distance between them. Consequently, the larger the separating distance between two objects, the smaller the attractive force. Known as Newton's Universal Law of Gravitation, this force (F) is given by:

$$F = \frac{Gm_1m_2}{r^2} \tag{2.7}$$

with,

$$G = 6.67384 \times 10^{-11}\ \mathrm{m}^3\ \mathrm{kg}^{-1}\ \mathrm{s}^{-2}$$

where, G is the universal gravitational constant, m_1 and m_2 are the masses of the objects and r is the separating distance between the centres of mass of each object.

When relating equation (2.7) to the Earth, we assume that the Earth is a perfect sphere of constant mass (M) and constant radius (R). For an arbitrary point mass m on the surface of the Earth, equation (2.7) becomes,

$$F = \frac{GmM}{R^2} \tag{2.8}$$

Newton's second law states that a force is equal to mass times acceleration, given by,

$$F = ma \tag{2.9}$$

In the case of the Earth, the acceleration is equal to gravity (i.e. $a = g$), which acts vertically towards the centre of the Earth. Combining equations (2.8) and (2.9) we see that,

$$g = \frac{GM}{R^2} \tag{2.10}$$

Equation (2.10) shows, for a simplified Earth, the acceleration due to gravity on the Earth's surface. The acceleration due to gravity (g) is proportional to M and inversely proportional to R^2.

2.4.1 The Earth's Gravity

If Earth were a perfect sphere and had a homogeneous mass distribution, gravity would be constant over its surface. In reality this is not the case due to Earth's irregular shape and heterogeneous mass distribution. The true Earth shape induces an equipotential surface (the geoid) which approximates mean sea level but undulates according to mass inhomogeneities. Regions where the geoid is lower

than the ellipsoid are highlighted by lows (equal to −107.0 metres and higher, in magenta), while regions where the geoid is higher than the ellipsoid are represented by highs (equal to 85.4 metres and lower, in red) (Figure 2.5). When measuring gravity over Earth's surface a more realistic model considers the following factors:

1. Earth tides and instrumental drift
2. Latitude of the observation point
3. Elevation of the observation point
4. Topography surrounding the observation point
5. Density variations of the subsurface

This section describes the process of isolating a residual anomaly for the Tasman Glacier; this is the change in gravity related only to density variations in the shallow subsurface. To obtain a residual anomaly, the first four factors outlined above must be accounted for in gravity reduction. The fifth is modelled to match residual anomalies in Chapter 3).

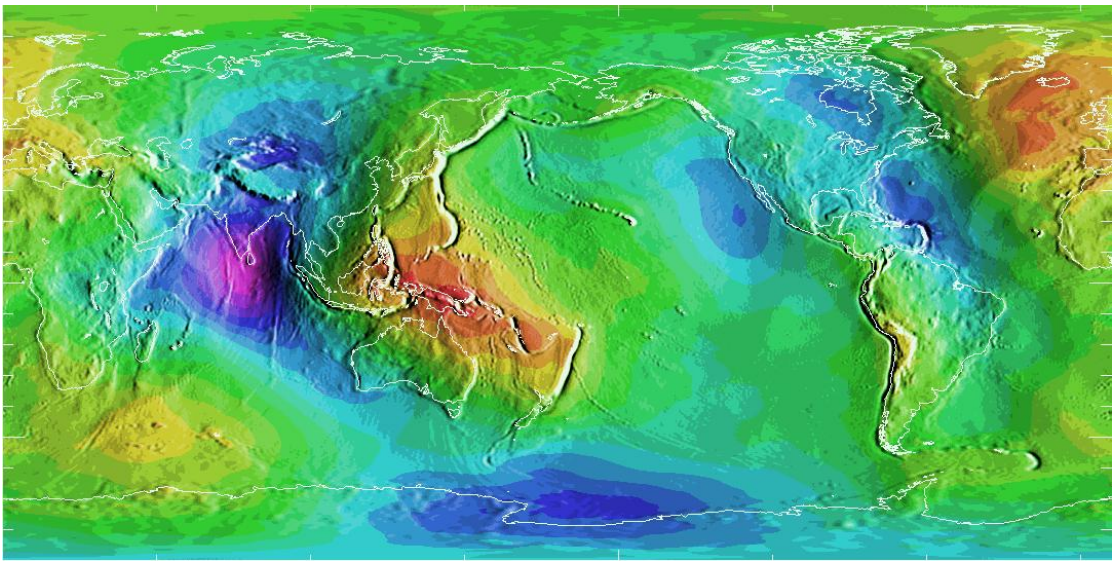

FIGURE 2.5: Deviations between a geoid model GEOID96 and the WGS84 reference ellipsoid. Figure from National Geodetic Survey, 1997.

2.5 Gravity reduction

2.5.1 Measuring gravity

Modern gravimeters can measure absolute and relative changes in gravity on the order of 10 parts per million and thus require a more suitable unit than ms^{-2}. The Gal, equal to 1 cms^{-2}, is adopted for geophysical uses, however the measurable changes seen by a gravimeter are on the order of the mGal (1×10^{-3} Gal) (Reynolds, 2011).

The device used to measure gravity for this survey is a LaCoste and Romberg gravimeter model G 179. The model G 179 measures relative changes in gravity on the order of $\pm$ 0.01 mGal between sites. Using a calibration factor specific to the meter, the meter units unique to the model G 179 are converted into mGals for each station (Reynolds, 2011). The observed gravity at a station (g_{obs}) is the raw measurement of gravity. In order to remove the external effects on gravity (outlined in section 2.4.1) g_{obs} must be reduced to a common datum such as the geoid (mean sea level) before corrections to the data can be made.

2.5.2 Absolute gravity

Absolute gravity is the acceleration due to gravity at a particular point in time and space. Often it is useful to express gravity in terms of its absolute value so that past studies can be tied to future studies. Absolute gravity is calculated from relative gravity values:

$$g_{abs} = g_{obssite} - g_{obsref} + g_{absref} \tag{2.11}$$

Where $g_{obssite}$ is the relative gravity reading at a new observation site, g_{obsref} is the relative gravity reading at the reference site, g_{absref} is the absolute gravity measurement at the reference site and g_{abs} is the absolute gravity measurement for the new observation site.

In this study, relative changes in gravity were recorded between observation sites. To convert relative gravity values to absolute values, a tie site where absolute gravity had already been established was used along with equation 2.11. The coordinates of the original tie site, established by Reilly (1972), did not match the map description provided; rather, they plotted on a hill slope adjacent to the Hermitage site description. We established a tie site on a permanent sundial adjacent to the Hermitage garage (this most closely resembled the site description) (Figure 2.6.) In order to tie this study to Reilly's tie site it was assumed that the absolute gravity from Reilly (1972) was equal to our tie site. The difference in absolute gravity between our reference site and the actual reference site is likely to be small, however the entire survey will have an associated static error of unknown value due to the discrepancy between tie sites (see Table 2.2).

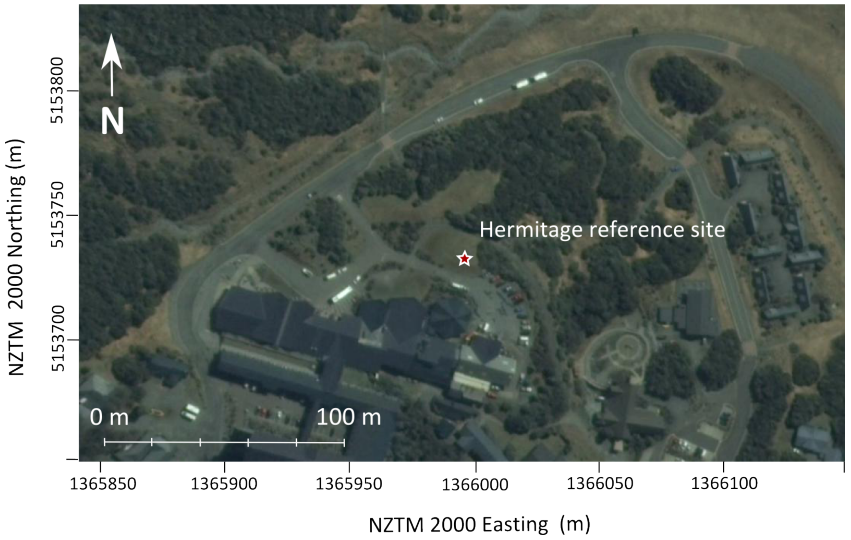

FIGURE 2.6: The Hermitage tie site established in this study is located at a sundial (red star). Coordinates are in NZTM 2000 (m). Image from Google Earth.

2.5.3 Variation of gravity with drift

The term 'drift' refers to the temporal changes in gravity that are induced as a result of both tidal forcings and spring relaxation in the meter (Claridge, 1983).

TABLE 2.2: Site information for Reilly's absolute gravity site and the tie site used in this study. Latitude and longitude are in World Geodetic System 1984 (WGS 84). Eastings and Northings are in New Zealand Transverse Mercator projection (NZTM 2000). Data obtained from the New Zealand Primary Gravity Network (Reilly, 1972).

	Mt. Cook absolute gravity station (Reilly, 1972)	Hermitage reference site (this study)
Latitude	43 44' 2"	43 43' 57"
Longitude	170 05' 5"	170 05' 40"
Easting	1365818.1	1365990
Northing	5153202.1	5153732
Elevation	748 m	760 m
g_{absref}	980270.85 mGal	980270.85 mGal

Instrumental and tidal drift are large enough to induce changes in the meter of 0.3 mGal/hr and $0.1 - 1.0$ mGal/hr respectively (Reynolds, 2011; Mishra, 2011).

Drift is accounted for by taking repeat measurements of an established base site at regular (1-2 hour) intervals (Reynolds, 2011). This study adopted a looping procedure at 8-12 hour intervals rather than 1-2 hour intervals due to (1) the survey lines being traversed over difficult terrain and (2) the lines being located several kilometres from the base station (Figure 2.1). A significant tidal drift component associated with the spring-neap cycle was seen in the data (Figure 2.7). To remove this, the combined effects of instrumental and the tidal drift over the 16 day period were modelled using a cosine function:

$$g_{drift} = Acos(\omega(t_{obs} - \phi)) + c \tag{2.12}$$

where A describes the amplitude of the waveform, ω describes the angular frequency of the waveform in radians per second, t_{obs} represents the time of each base site reading relative to the first base site reading, ϕ describes the phase of the waveform in radians and c is a constant. The values associated with equation 2.12 are summarised below:

Equation (2.12) is fitted to the set of readings according to the least squares method (Figure 2.7). It is assumed that the cosine function corrects for both the

TABLE 2.3: Constants related to equation (2.12)

Constant	Value
A	0.22
ω	0.0002
ϕ	3000
c	3863.41

spring-neap cycle and instrumental drift, even though the spring-neap signature dominates the model.

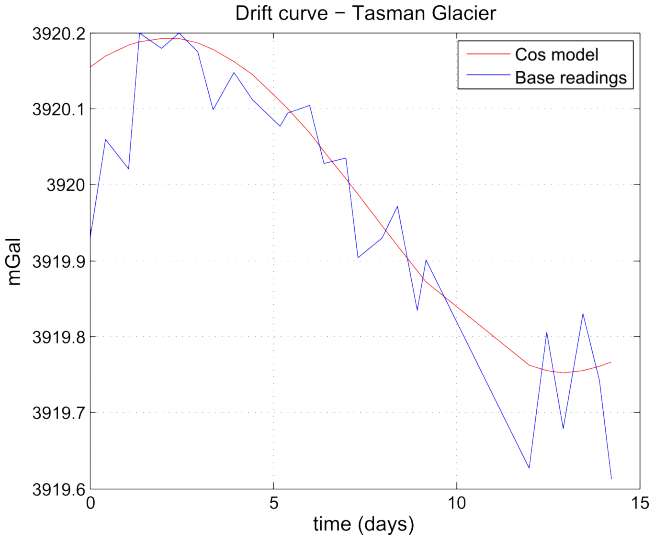

FIGURE 2.7: Drift curve model obtained using equation (2.12). The cosine model (red) is fitted to observed base readings (blue) according to the least-squares method. The rms misfit between the two curves is ±0.08 mGal.

The drift corrected values for each site are then calculated as the difference between g_{abs} and g_{drift}:

$$g_{obs_{dc}} = g_{abs} - g_{drift} \tag{2.13}$$

where $g_{obs_{dc}}$ is the observed drift-corrected gravity, g_{abs} is the absolute gravity and g_{drift} is the trend due to instrumental and tidal drift

2.5.4 Variation of gravity with latitude

The force of gravity varies with latitude due to the Earth's rotation. As the Earth rotates, an apparent outward (centrifugal) force (F_c) is generated. Over large time scales the Earth responds to the centrifugal force as a fluid, whereby the equator bulges outwards and the poles flatten. The term used to describe this shape is an ellipsoid of rotation. Two forces are considered to influence the Earth's gravity field: The gravity force (F_g) which acts from all directions towards the centre of the Earth, and the centrifugal force (F_c) which is directed outwards perpendicular to the axis of rotation. The force-balance relationship between (F_c) and (F_g) results in an equatorial bulge relative to the poles (Figure 2.8) (Reynolds, 2011). The centrifugal force opposes the gravity field (F_g) with a maximum force at the equator, diminishing to zero at the poles. Consequently, the force of gravity increases with latitude as F_c decreases with latitude (Reynolds, 2011; Mishra, 2011).

The flattening of the poles also affects the mass distribution of the Earth. There is a gradual decrease in the force of gravity from the equator to the poles due to a relative mass deficiency with increasing latitude (λ). The combined effect of rotation and a variable radius/mass distribution leads to an overall increase in F_g with increasing latitude. This amounts to a difference of approximately 5200 mGal between the equator and the poles (Fowler, 2005).

To a first-order, an ellipsoid of rotation can be used to model the latitudinal dependence of gravity (Reynolds, 2011; Fowler, 2005) (Figure 2.8). The true gravity distribution for the Earth is much more complicated than the ellipsoid of rotation. Large and small-scale geological features warp the gravity field so that the equipotential surface deviates from the ellipsoid. This surface, known as the geoid, is approximated by mean sea level (Reynolds, 2011). To a first order, the reference ellipsoid can be used to estimate the latitudinal dependence of gravity despite deviations between the reference ellipsoid and the geoid. The most recent shape of the reference ellipsoid is modelled by the 1987 International Gravity Formula. It provides an approximate value of gravity $g(\lambda)$ for any given latitude (λ):

$$g(\lambda) = g_e(1 + \alpha \sin^2 \lambda)(1 - \beta \sin^2 \lambda) \tag{2.14}$$

where g_e is the gravitational acceleration at the equator, equal to 9.780327, with constants $\alpha = 1.932 \times 10^{-3}$ and $\beta = 6.694 \times 10^{-3}$. It should be noted that the Hermitage reference site (which this study is tied to) is relative to the 1930 International Gravity formula. Therefore a correction was made using equation (2.15) to calibrate it to the more recent 1987 formula:

$$g_{herm} = g_{abs} + g_{1980} - g_{1930} \tag{2.15}$$

where g_{abs} is the absolute gravity at the Hermitage site, g_{1980} is the 1980 international gravity formula, g_{1930} is the 1930 international gravity formula (Fowler, 2005) and g_{herm} is the updated absolute gravity for the Hermitage reference site. g_{herm} is the absolute value of gravity used in this study, summarised in Table 2.2.

The latitudes of all gravity stations occupied in this study were inputs to equation 2.14 which describes the theoretical gravity for each station. These values are used later in Section 2.5.7 to calculate the contribution to the Bouguer model.

2.5.5 Variation of gravity with elevation

Relative to the centre of the Earth, any elevation change will result in a change in g (see equation (2.10)). To account for this change, two corrections must be applied:

1. The free-air correction
2. The Bouguer slab correction

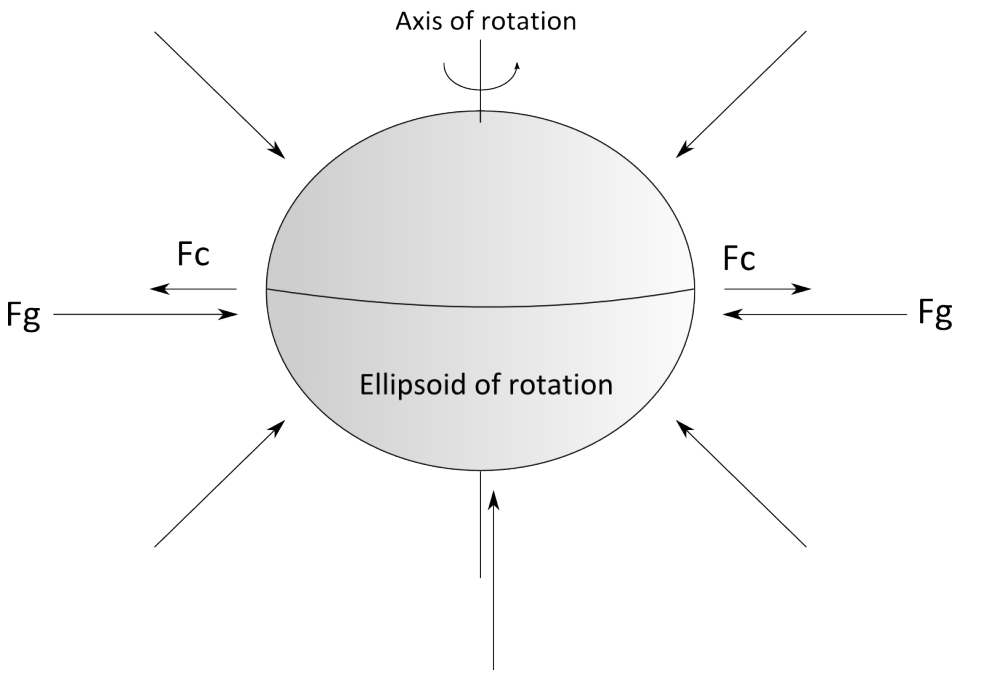

FIGURE 2.8: The Earth represented as an ellipse of rotation. The actual flattening is $\simeq 1/300$ but is exaggerated here to display an elliptical shape.

Free-air correction

The free-air correction is used to describe the difference in gravity between two points due to a change in height (h). A change in height is seen as the difference between the observation point and the geoid (Reynolds, 2011). The free-air gradient dismisses any materials between the observation point and the geoid; this is accounted for by the Bouguer slab correction in Section 2.5.5. The accepted value for the free-air gradient is:

$$g_{FA} = -0.30855\text{h} \tag{2.16}$$

The G 179 meter used in this survey has a precision of $\pm$ 0.01 mGal. To comply with this level of accuracy, elevations must ideally be known to within $3 - 5$ cm for the free-air correction (Reynolds, 2011).

Bouguer slab correction

The Bouguer slab correction is a first-order approximation for the mass in between the observation point and the geoid. It removes the extra gravitational pull imposed by the mass of an infinite horizontal slab. The Bouguer slab correction assumes the infinite slab has a uniform density (ρ) and thickness (h) (Figure 2.9) (Fowler, 2005; Mishra, 2011; Reynolds, 2011). The correction is:

$$g_B = 2\pi G\rho \mathrm{h} \tag{2.17}$$

The combined effects of the free-air gradient and the Bouguer slab define the elevation correction:

$$g_E = (-0.30855 + 2\pi G\rho)\mathrm{h} \tag{2.18}$$

The change in g_{abs} associated with the height above the geoid and the mass of a constant density slab of rock is corrected for by the elevation correction.

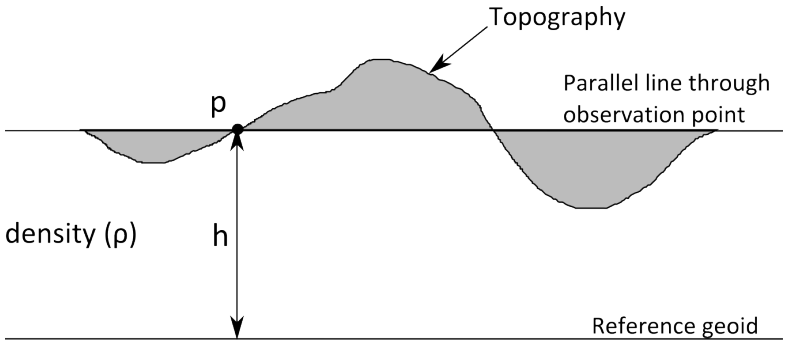

FIGURE 2.9: The variation of gravity with elevation is marked by a semi-infinite slab which lies parallel to the reference geoid. Point p is affected by (1) the height (h) above the geoid (free-air) and (2) the density of the slab between p and the geoid (Bouguer slab). Figure adapted from Davy (2012).

Uncertainties in the density of the Bouguer slab can lead to significant errors in the overall elevation correction. A mean crustal density of 2670 kg/m^3 is typically assumed for geological and gravimetric surveys (Hinze, 2003), while the greywacke sandstone surrounding the Tasman Glacier has an average density of 2639 kg/m^3 (Tenzer et al., 2011). Given that the slab correction for gravity is 4.19 mGal/100

m, (equation (2.17)) the difference between these values for a glacier elevation range of 750 - 1000 m results in a Bouguer anomaly error of 0.97 - 1.3 mGal. The magnitude of this error becomes insignificant when incorporated into the overall elevation error (See Section 2.5.8 - Elevation and position error).

Here, I adopt an average crustal density of 2670 kg/m^3 for greywacke. This value was chosen so that this study could be compared to previous gravity surveys (e.g. Broadbent (1973)) who also used 2670 kg/m^3 as their crustal density for greywacke in the region.

2.5.6 Variation of gravity with topography

The terrain correction (g_T) is used to quantify and remove variations in height about an infinite horizontal plane from an observation point (Fowler, 2005; Reynolds, 2011). Topographic variations are typically quantified using a Hammer Chart, where a template consisting of concentric segmented rings is placed over a topographic map and the average elevation of each segment is estimated (Hammer, 1938). The rings are weighted according to distance from the gravity measurement, such that closer rings have a larger influence on the gravity at an observation point. The Hammer Chart quantifies topography out to 21.9 km; beyond this distance any change in height has a negligible effect on gravity (Hammer, 1938).

For inner terrain corrections (0 - 170.1 m), average elevations are typically estimated by the surveyor (Table 2.4). Outer terrain corrections (170.1 m - 21.9 km) may use topographic maps. Modern techniques employ Digital Elevation Models (DEMs) which allow for more accurate estimations of terrain (e.g. Chen and Yue (2010); Columbus et al. (2011)). This study incorporated a combination of surveyor estimates for elevation and GPS derived elevations. GPS derived elevations were favoured, where possible, for their accuracy.

TABLE 2.4: Radii of inner terrain corrections out to zone D (170.1 m).

Inner terrain zone	Radius range
A	0-2 m
B	2-16.6 m
C	16.6-53.3 m
D	53.3-170.1 m

Inner terrain corrections

Inner terrain corrections (g_{Tinner}) were estimated by the surveyor between zones A to D over the lower Tasman Glacier. The irregular topography of the glacier surface made estimating elevations difficult, hence elevation data were also collected with the Trimble Geo XH GPS where possible. A digitized Hammer chart was created to incorporate inner terrain corrections from both eye-estimated elevations and GPS elevations (Figure 2.10). Red and blue 'plus' symbols represent Geo XH derived elevations, delineated by colour to distinguish individual segments of the Hammer chart. For inaccessible areas, the Geo XH could not sample certain topography, hence estimates by the surveyor had to suffice; these segments of the Hammer chart are represented by black lines. Zone A was always assumed to be level and thus no terrain correction was required.

To verify that each inner terrain correction estimated by eye was valid, scatter plots of eye elevation versus GPS elevation were made for each segment of the Hammer Chart. In general, the eye method slightly overestimates elevation except for the D radius. The spread in the plots is large, reflecting the difficulties encountered in estimating elevations by eye on the glacier surface (Figure 2.11). Provided that the two methods were directly proportional, segments with sparse or no GPS measurements could be replaced with the appropriate eye estimate.

Outer terrain correction

Outer terrain corrections (g_{Touter}) were determined between 170.1 m and 21.9 km using the software 'TopCor' developed by Davies (2005). TopCor utilises digital

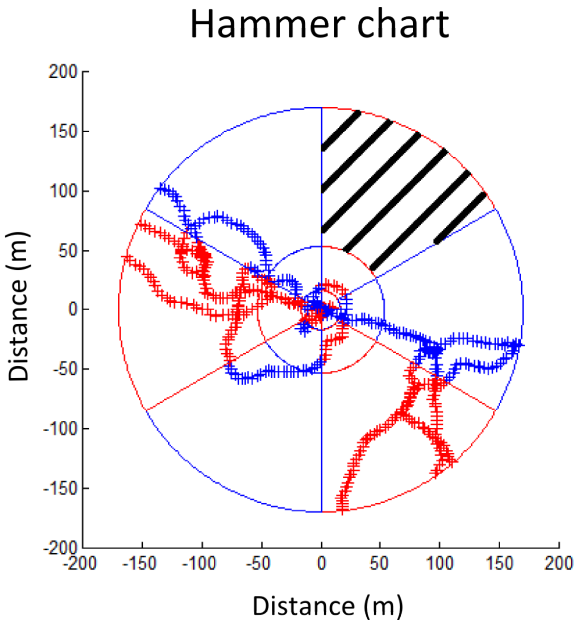

FIGURE 2.10: A typical Hammer Chart used for an observation point between zones B to D. Geo XH GPS elevations are distinguished by alternating segments of blue and red 'plus' symbols. In segments with sparse GPS elevations surveyor estimations of elevation were used (black lined area).

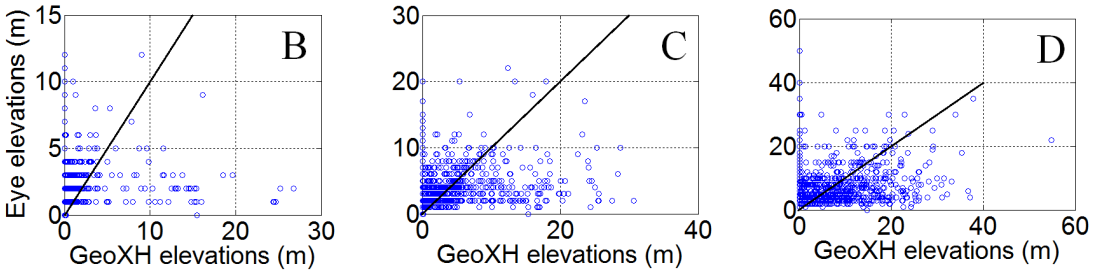

FIGURE 2.11: Inner terrain estimates for B, C and D radii. Blue circles represent the eye elevation estimate versus the measured GPS value for each segment of the inner terrain. Black lines denote a 1:1 ratio between the two methods.

elevation models and the location of each gravity station to produce an outer terrain correction for each station. The DEM used for this study (NZSoSDEM v1.0) has a spatial resolution of 15 metres (Columbus et al., 2011).

The total terrain correction for an observation point is found by summing the inner and outer terrain corrections given by:

$$g_T = g_{Tinner} + g_{Touter} \tag{2.19}$$

Glacier down-wasting

In recent decades, the Tasman Glacier has experienced significant thinning which has reduced its surface elevation (e.g. Hochstein et al. (1995)). The more recent (2013) glacier surface has decreased on the order of several metres per year relative to the 1986 DEM (NZSoSDEM v1.0). If left uncorrected, this discrepancy in elevation would lead to significant errors in the outer terrain correction. To account for the elevation error, elevation data collected via GPS during this survey was used to replace those parts of the outdated DEM occupied by the lower Tasman Glacier. This was done on a point-by-point basis, where out-of-date points on the 1986 DEM were replaced by an area-averaged point. The resulting DEM consisted of an updated glacier surface while the moraine walls and surrounding topography were left unchanged as negligible vertical change has taken place in these areas.

2.5.7 Bouguer anomaly

The Bouguer anomaly is the departure between the theoretical gravity at a location (corrected for drift, latitude, elevation and terrain) and the observed gravity measurement. It is assumed that the Bouguer anomaly represents the density variation of the subsurface and any long period wavelength associated with a regional trend (Fowler, 2005; Reynolds, 2011). The steps outlined in Section 2.5 provide a method for calculating the theoretical gravity at each observation point on the Tasman Glacier. Also known as the Bouguer model (g_{boug}), the theoretical gravity at a point is summarised by:

$$g_{boug} = g_{\lambda} + g_E - g_T \tag{2.20}$$

Where g_{λ} is the expected gravity for latitude λ, g_E corrects for both the free-air and bouguer plate and g_T corrects for terrain. The Bouguer anomaly (g_{anom}) is defined by the difference between the observed drift-corrected gravity and the theoretical Bouguer model:

$$g_{anom} = g_{obs_dc} - g_{boug} \tag{2.21}$$

Substituting Equation 2.20 into Equation 2.21 leads to:

$$g_{anom} = g_{obs_dc} - g_{\lambda} - g_E + g_T \tag{2.22}$$

2.5.8 Uncertainty in the Bouguer anomaly

Uncertainties in each gravity measurement arise primarily from four sources. These include: meter reader error, drift curve modelling, terrain corrections and the error in position and elevation.

Reader error

For each gravity station the meter was read a minimum of three times. The precision of the meter at 0.01 meter units ($\simeq 0.01$ mGal) meant that 3 consistent readings within 0.1 mGal were readily achievable, although outside factors such as wind, ice melt, unstable ground and seismic activity sometimes meant that measurements were outside the 0.1 mGal range. 89% of readings had a range within 0.03 mGal while 98% had a range within 0.1 mGal. Considering that 98% of the stations are within ± 0.05 meter units for this survey, the reading error is established as:

$$U_r = \pm 0.05 \,\text{mGal}$$

Drift error

To measure instrumental and tidal drift, base readings were taken on average every 12 hours. The average drift between readings was 0.083 mGal with a standard

deviation of 0.177 mGal while the maximum drift was 0.274 mGal between Sunday 3rd February and Wednesday 6th February 2013. The cosine model fitted to the meter readings used a method of least squares and had a standard deviation of 0.078 mGal, hence the uncertainty associated with drift is:

$$U_d = \pm 0.08 \,\text{mGal}$$

Terrain correction error

The uncertainties involved with estimating terrain proved the most significant, contributing over 99% of the entire error for each gravity station. Of the 189 stations surveyed, 77% of inner terrain corrections were less than 0.5 mGal while 97% were less than 1.0 mGal.
Inner terrain corrections had a significant error due to:

1. the irregular, hummocky terrain over the glacier, and
2. inner terrains being composed of both reader estimates and GPS measurements (Figure 2.10).

Uncertainties for the inner terrains are quoted to one standard deviation. B, C and D radii have a standard deviation of ±0.142 mGal, ±0.155 mGal and ±0.148 mGal respectively. When the variances are summed, the inner terrain error for each station is

$$U_{it} = \pm 0.26 \,\text{mGal}$$

U_{it} accounts for uncertainties out to zone D (170.1 m).

For outer terrain corrections (170.1 m - 22 km) the uncertainties depend on the resolution of the digital elevation model used. The DEM used for this survey

(NZSoSDEM v1.0) has a spatial resolution of 15 m with a standard deviation of 6.8 m and produced outer terrain values as high as 23 mGal. To quantify uncertainties for the outer terrains, 10% of the stations had Gaussian noise applied to the DEM with a standard deviation of 6.8 m. This allowed the DEM to vary by ±6.8 m, thus altering the outer terrain corrections. The uncertainty in the outer terrains was ± 0.88 mGal for distances greater than 170.1 m, where each node of the DEM was allowed to vary by the standard deviation. The approach is limited in the sense that topography would not vary randomly from node to node in reality; rather, one would expect it to vary over a wider area such as a valley or a ridge. However, as a first-order constraint on the outer terrain error, the Gaussian approach is appropriate.

The overall uncertainty associated with terrain is the sum of the inner and outer terrain uncertainties given by:

$$U_t = U_{it} + U_{ot} = 0.26 + 0.88$$

where U_t is the total terrain correction and U_{ot} is the outer terrain correction. Thus U_t is equal to ± 1.14 mGal.

Elevation and position error

The uncertainties associated with elevation and position are due to errors in elevation (free-air), latitude and density (Bouguer plate). With the development of differential GPS techniques, the errors involved in calculating elevation and position have been significantly reduced. Mounted with an external antenna, the precision of the Trimble GeoXH captured 93% of station heights within 50 cm. According to the elevation correction (equation 2.18) a deviation of 1 m of elevation is equivalent to a ±0.1967 mGal error (for a slab density of 2670 kgm^{-3}). In contrast, the international gravity formula (equation 2.14) indicates that a deviation of 1 m in latitude is equivalent to a ±0.0008 mGal error. For this reason,

latitudinal errors were assumed to be negligible.

ardincorporates both the free-air and Bouguer plate uncertainties:

$$U_e = (-0.3086 + 0.0419\delta\rho) \times \delta h \tag{2.23}$$

Where $\delta\rho$ is the uncertainty in the density of the Bouguer slab and δh is the error in elevation for a given gravity station. According to equation (2.23) a density error of $\pm$ 15 kgm^{-3} and an elevation error of $\pm$0.25 m corresponds to a $\pm$0.08 mGal error for each station, 99.99 % of which is due to the elevation error. Thus the error associated with elevation, position and density is:

$$U_e = \pm 0.08 \,\text{mGal}$$

Total uncertainty

The errors presented here represent measurement errors related to the formal measurement and processing stage of gravity reduction. The total uncertainty for each gravity station is the root mean square of each of the sources of error:

$$U = \sqrt{U_r^2 + U_d^2 + U_t^2 + U_e^2} \tag{2.24}$$

where U is the uncertainty at each observation site. All errors are presented in mGals to one standard deviation. For all sites the total uncertainty is $\pm$1.18 mGal representing one standard deviation.

Further uncertainties are introduced in this study regarding the reduction of the Bouguer anomaly to the residual anomaly (Section 2.6). These uncertainties are likely to be very significant if not more so than the measurement and processing errors discussed above; however they cannot be addressed in a quantitative manner as they were not acquired.

2.5.9 Gravity reduction summary

To summarise, the steps taken to reduce gravity measurements down to the Bouguer anomaly are:

- Convert relative gravity readings ($g_{obssite}$) into absolute gravity values (g_{abs}) using an established reference gravity station (Hermitage Hotel) and equation 2.11.
- Correct g_{abs} for drift using equation 2.13. To obtain $g_{obs_{dc}}$, the drift component (modelled by a cosine curve) was subtracted from g_{abs}.
- Calculate g_λ using the 1987 International Gravity Formula (equation 2.14).
- Calculate the free-air correction g_{FA} using equation 2.16 and the Bouguer Plate correction g_{BP} using equation 2.17. The sum of these two corrections is equivalent to the total elevation correction (g_E).
- Using the methods described in section 2.5.6 calculate the contribution of the inner and outer terrain corrections using equation 2.19.
- Calculate the Bouguer gravity anomaly using equation 2.22. This includes the aforementioned corrections above:

$$g_{anom} = g_{obs_{dc}} - g_\lambda - g_E + g_T \tag{2.25}$$

- Errors are established for: reader error, drift error, terrain error, elevation error and summed in equation 2.24.

2.6 Regional-residual separation

The Bouguer anomaly represents the combined effects of both deep seated structures and relatively shallow features; its appearance reflects this through both long and short wavelength components. Often it is desirable to separate these

components in order to observe the regional and residual anomalies individually (e.g. Reynolds (2011)). To accurately separate the anomalies, a set of Bouguer anomaly points must be extensive enough to capture the regional trend yet dense enough to resolve the residual trend (Burger et al., 2006). However, the solution is non-unique; the transition from small to large wavelengths is ambiguous. A typical approach is to employ a combination of analytical and graphical methods to accurately identify and remove the regional trend (Reynolds, 2011).

2.6.1 Mathematical methods

There are many mathematical approaches to separating the fields such as (1) removal by frequency filtering or (2) fitting a low-order polynomial to the Bouguer anomaly data (Reynolds, 2011). Low-order polynomials fit regional data appropriately compared to higher order polynomials which also capture part of residual anomaly. This study explores a range of polynomial functions to describe the regional signal and then separate it from the residual signal. Low order polynomial surfaces ranging from first-order to third-order demonstrate this approach in Figure 2.12.

Regional-residual separation for the Tasman Glacier

The Tasman Glacier region is influenced by a broad negative anomaly due to the Southern Alps (Davey et al., 2007) and the spatially constrained, residual anomaly due to the Tasman Glacier (Figure 2.13). To accurately capture the regional anomaly, Bouguer anomaly points were chosen on sites with small density variations and widespread distribution according to the method used by Stern (1978). Bouguer anomaly points located on bedrock sites such as greywacke ensured the regional fit was independent of the residual anomaly generated by the ice-based sites of the Tasman Glacier. The Bouguer anomaly associated with the Southern Alps is on the order of -20 to -100 mGal (Davey et al., 2007) while the Tasman Glacier Bouguer anomaly has a much smaller range of -80 to -100

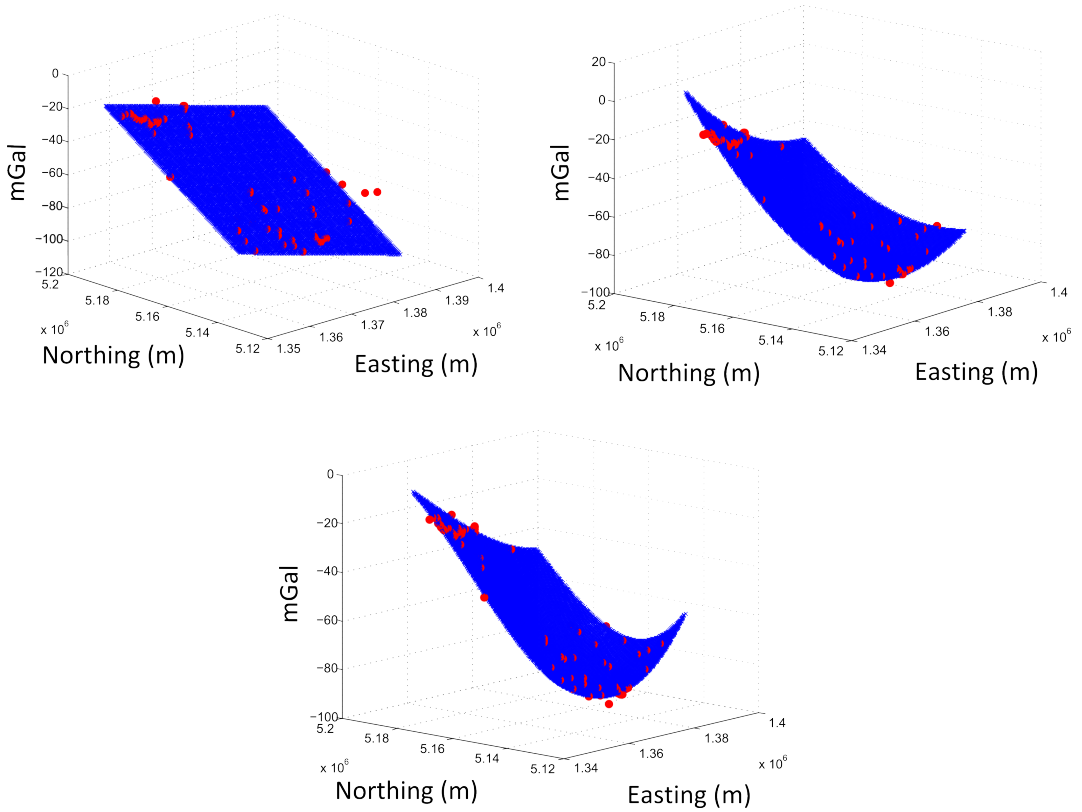

FIGURE 2.12: Bouguer anomaly points in red are modelled using mesh surfaces from a range of polynomial functions (in blue). Polynomial functions range from first order to third order (A to C).

mGal (Figure 2.13).

A surface fitting approach was used to remove the regional trend from the Tasman Bouguer anomaly. A series of low-order polynomials were fitted in x-y-g space to the regional Bouguer anomaly points seen in Figure 2.12 using a method of least squares. The most appropriate polynomial surfaces were then chosen according to (1) their minimum root mean square (rms) error (Figure 2.14) and (2) their compatibility with the regional geological setting. With increasing order, the polynomial surfaces have better fits to the Bouguer anomaly data. However, the higher order surfaces become complex and develop unrealistic curvature at their edges. Because data fitting methods are not constrained by the local geology they tend to overlook unreasonable circumstances such as this. A decision was made to represent the regional Bouguer anomaly signal with a second-order polynomial surface which has both a low rms error and long wavelength signature (Figure 2.14).

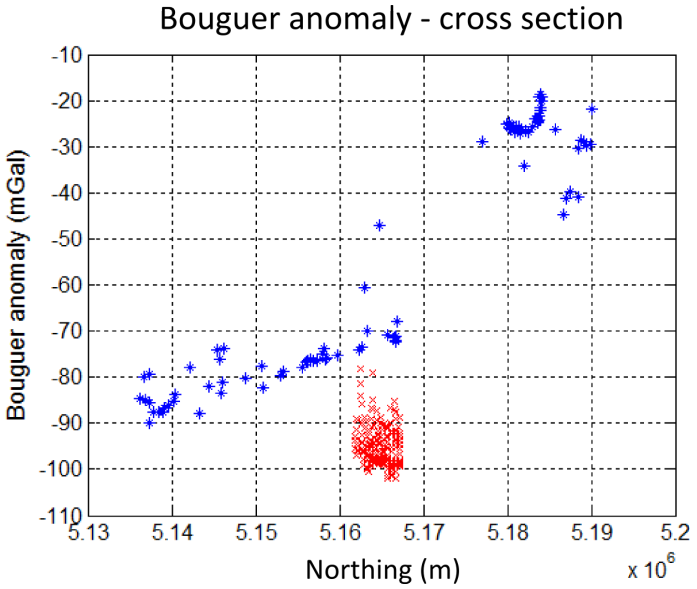

FIGURE 2.13: Bouguer anomaly values versus Northing for regional sites (blue) and Tasman Glacier sites (red) from this study.

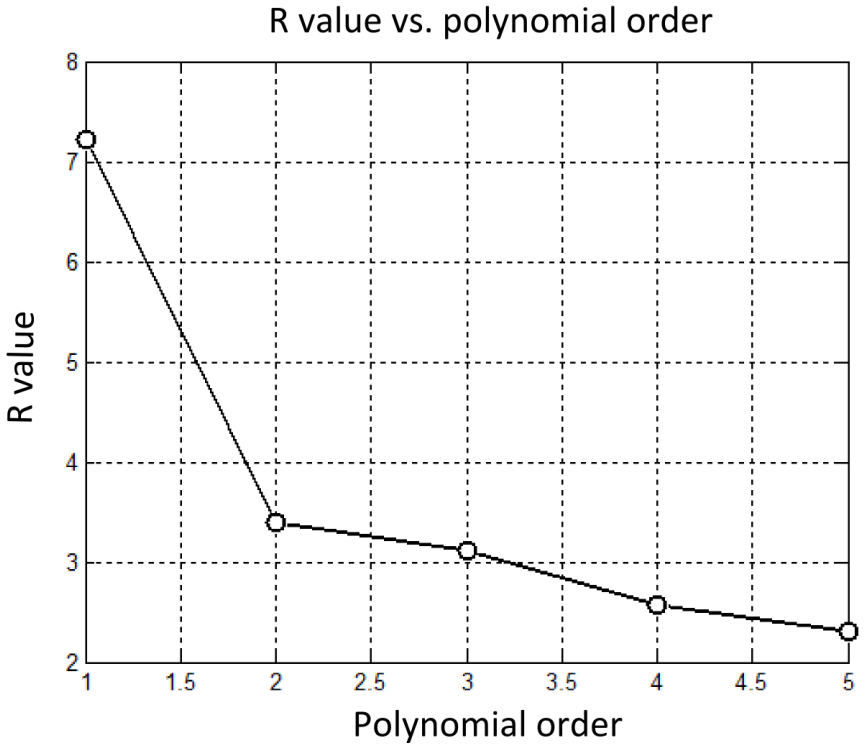

FIGURE 2.14: RMS error versus polynomial order. With increasing polynomial order the rms error necessarily decreases. A second-order polynomial satisfies a low enough rms error whilst not over fitting the Bouguer anomaly points.

The second-order polynomial representation of the regional Bouguer anomaly

was subtracted from the Tasman Bouguer anomaly points to obtain the residual anomaly. Figure 2.15 demonstrates the effect of applying a regional-residual separation. Because the regional trend centred about the Tasman Glacier was relatively planar, the residual is simply shifted on the order of the regional signal at that location (−70 to −80 mGal).

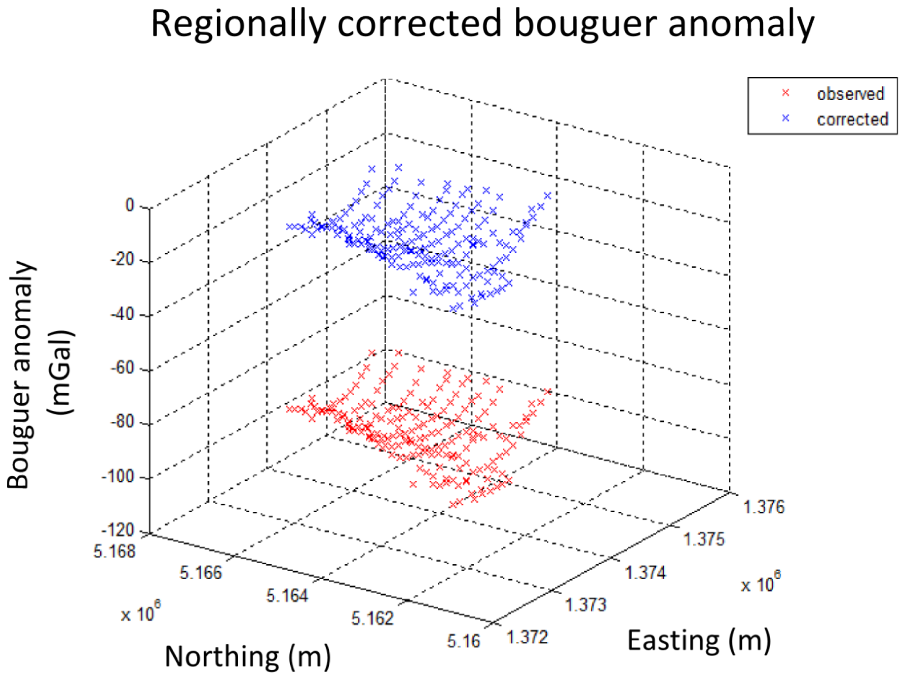

FIGURE 2.15: Regionally corrected Bouguer anomaly values using a second order polynomial.

Residual anomaly

Following the regional correction, a number of the residual anomaly values remained positive at the edges of the glacier, in part due to a partial regional signature remaining in the data but also because the residual anomaly was not absolutely tied to basement sites on the edges of the glacier. To remove the remaining regional signature a scalar (DC) shift was applied to the residual data to force all values to be negative. The data were shifted by subtracting the highest residual anomaly value from the entire dataset. The absence of tie sites for the residual anomaly is unappealing for gravity modelling; the residual anomaly

should be equal to zero at the largest anomaly value. Uncertainties are introduced into the ice thickness models because the residual anomaly has not been absolutely fixed to basement sites. To resolve this issue, gravity readings should be made on basement sites along the lateral edges of the Tasman Glacier. This suggestion is unreasonable for the eastern edge of the Tasman Glacier due to the steepness of the valley slopes, however the western edge is more favourable and could provide an improvement for future studies utilising the residual anomalies presented here. For the models presented in Chapter 3 the uncertainty in the residual anomalies is the quoted value of ±1.18 mGal. In reality, this uncertainty is larger than this due to the issues discussed above. However, because this uncertainty cannot be quantified it not be addressed; however it does exist and it should be noted when ice thicknesses models are presented.

The 2D residual anomaly profiles were gridded using a linear interpolation method. The residual anomaly grid seen in figure 2.16 demonstrates the end product of gravity reduction. A clear U-shaped form is seen the data, demonstrating that residual anomaly values decrease towards the centre of the valley, reaching a minimum of -24 mGal, and increase to zero at the edges. The lower Tasman Glacier (between 5163000 N and 5164000 N) is characterised by a linear feature with relatively high residual anomaly values which extend approximately north-south for 1 km. This feature will be explored in more detail in Chapter 3.

2.6.2 Regional-residual separation summary

Here, a surface fitting approach was used to represent the regional Bouguer anomaly signal. By subtracting the regional Bouguer anomaly from the Tasman Bouguer anomaly points, a residual anomaly was obtained. A second-order polynomial was chosen to represent the regional trend for its good-fit (low R value) and long wavelength signature associated with the crustal root of the Southern Alps. The edges of the residual anomaly remained above zero. To correct this error, a static correction was made by removing the highest residual anomaly value from the

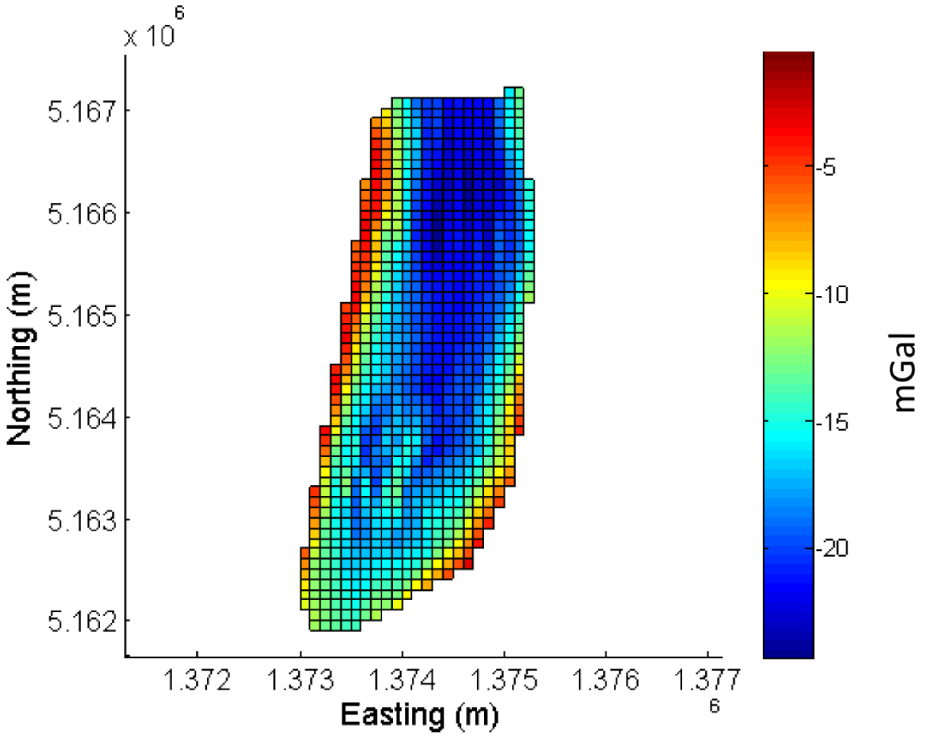

FIGURE 2.16: Plan view of the interpolated residual anomaly for the Tasman Glacier. Map coordinates are given in NZTM 2000 while residual anomaly units are in mGals.

entire dataset. The final residual anomaly for the Tasman Glacier will be used as an input for forward and inverse models in Chapter 3.

2.7 Ice volume estimation

This section describes the theory behind a recently-developed method for estimating the ice volume of the Tasman Glacier.

The method developed by Farinotti et al. (2009) assumes that the mass balance distribution of a glacier is equal to the sum of the ice flux divergence (the cumulative mass flux up-glacier from a flow line) and surface elevation change (assuming basal melt to be negligible). Ice flux is calculated using an 'apparent mass balance' factor computed using surface elevation changes. Taking the ice flux divergence (from predefined flow-lines) and the surface elevation of a glacier, ice

thickness (H) is calculated using Glen's flow law. Ice thickness (H) at any point along the flow line is calculated using the equation:

$$H = \sqrt[n+2]{\frac{q_i}{2A}\frac{n+2}{(C\rho g \sin\alpha)^n}} \tag{2.26}$$

where q_i is the mean specific ice volume flux along the flow line, ρ is ice density, g is the acceleration due to gravity, α is the mean surface slope and n is a constant. The parameter A is a flow rate factor taken from Glen (1955) while C represents a correction factor describing (in part) the contribution of basal sliding to the total flow speed. C can be calibrated using direct ice-thickness measurements (Farinotti et al., 2009).

The accuracy of this method has been assessed by comparing the cross-sections of the modelled and measured outputs. In Farinotti et al. (2009) the ice-thickness distribution for four alpine glaciers in Switzerland was measured using results from radio echo soundings. A point-to-point comparison between their measured and modelled results indicates a precision of ∼25%. Here, I describe a simpler version of this method. I use this method in Chapter 3 to assess the accuracy of modelled ice thickness versus ice-thickness results using gravity.

2.7.1 A simplified ice-thickness model

A simplified implementation of Farinotti et al.'s method is outlined here for the Central Southern Alps region (Figure 2.17). The model is simplified in three ways. First, the area-averaged mass balance for each glacier in the model domain is assumed to be zero (glaciers are in equilibrium with the present-day climate). Second, surface elevation changes are not considered for the contribution to 'apparent mass balance' (used by Farinotti et al. (2009)). Third, the ice flux divergence is calculated within elevation bands (20 m contour interval) for each glacier, rather then along flow lines (which considers multiple glacier catchments). Additionally, to recreate an approximately parabolic valley profile, the mass flux flowing through each elevation band is distributed into cells (within the elevation band) and scaled

linearly from the glacier margin to the centre of the glacier.

The flow rate factor A and the correction factor C are the most sensitive factors affecting the calculated ice thickness (equation 2.26, Farinotti et al. (2009)). The ice-thickness model for the Central Southern Alps has little ice-thickness information (Anderson, pers. comm. 2013) hence C is not well constrained for the model domain. By providing direct ice-thickness measurements to the model, calibrations of C can be made.

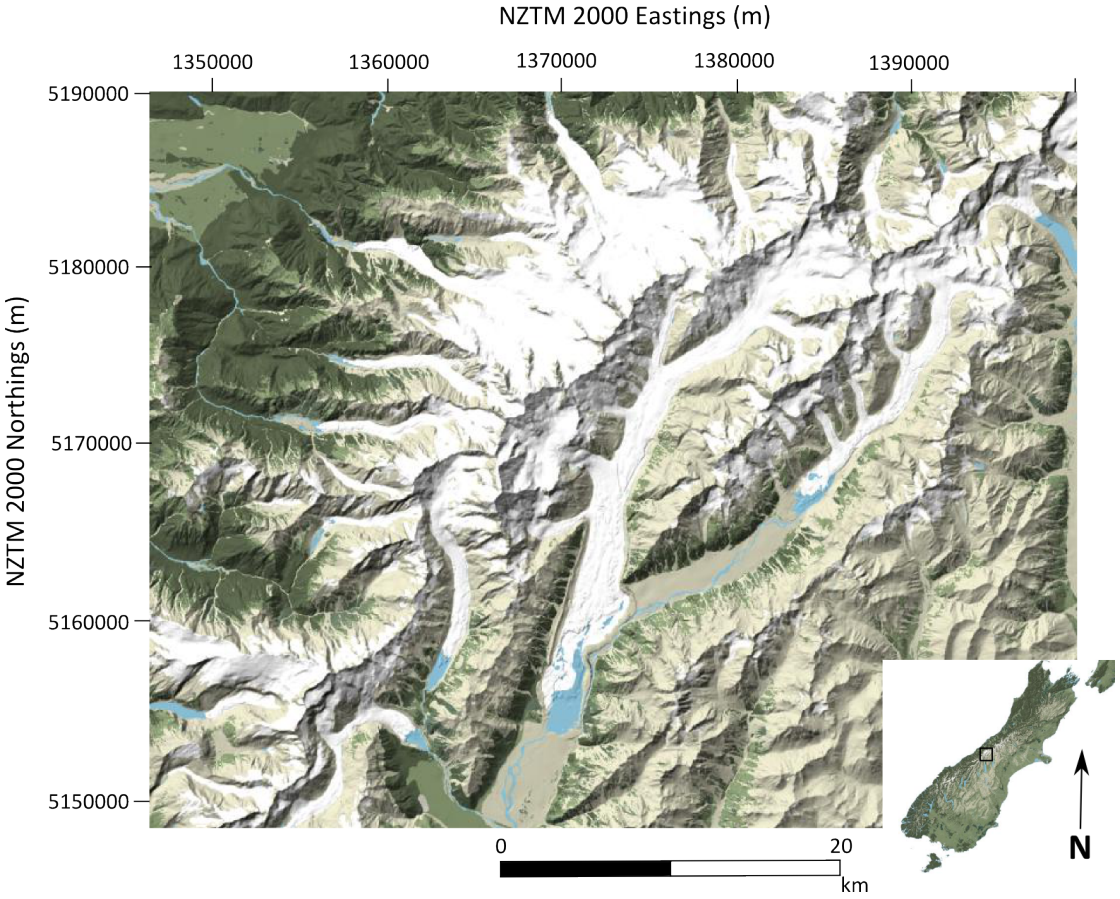

FIGURE 2.17: Map of the Central Southern Alps model domain. Map units are in metres (NZTM 2000 projection). Data obtained from Landcare Research 2012. Data sourced from LINZ.

2.8 Summary

Gravity and refraction seismics data are combined to explore the ice-thickness distribution of the Tasman Glacier. Residual anomalies are reduced from raw gravity observations; these are later modelled to investigate the shape and thickness of the lower Tasman Glacier. Refraction seismic data are used to constrain the density of ice, till and basement rock. A simple mass flux model is then presented to describe the ice thickness distribution of the Tasman Glacier. The following chapter details the ice-thickness results of 2D and 3D gravity models and explores the application of these results to the mass flux model described above.

Chapter 3

Results: Ice thickness distribution of the Tasman Glacier

3.1 Introduction

This chapter describes results obtained from the gravity survey over the Tasman Glacier. Initially, I present a suite of synthetic models to explore the major controls on ice-thickness variability. Models are used to critically assess the uncertainties involved in estimating ice thickness. A brief comparison of 2D models with past studies is presented to assess the validity of ice-thickness results. The ice-thickness distribution of the glacier is then explored through both 2D and 3D gravity models. Finally, ice-thickness data from this work is applied to a simple mass flux model to estimate the ice-thickness distribution and volume of the Tasman Glacier.

3.2 Gravity modelling

A gravity model represents the structure of the subsurface geologic units. By adjusting the shape and physical properties of the geologic units, an attempt is made to match the gravity response due to the geology to the measured residual anomaly. The effect calculated in a model is dependant on the shape, density

and depth of the causative bodies. The shape and depth of bodies is difficult to constrain without direct observations. However, the densities of ice and till are well constrained for this study. The density contrast between ice and basement rock is large 1770 kgm^{-3}, hence a high amplitude residual anomaly exists for regions of thick ice. Uncertainties in the density of the bodies and the residual anomaly propagate into the resulting model which lead to uncertainties in the extent of the bodies of interest.

A forward approach is employed for the 2D model, a geologically reasonable shape is produced and the calculated gravitational response is compared with the observed residual anomaly. When the difference between the calculated response and the observed anomaly are within uncertainty (±1.18 mGal), the model is accepted. 3D models use both forward and inversion models using the software package by 'Oasis montaj' developed by Geosoft.

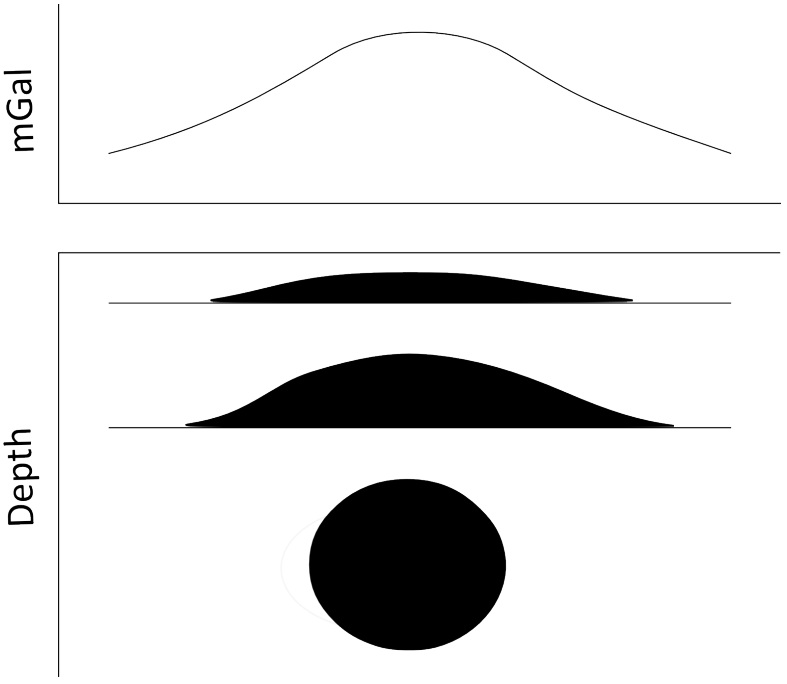

FIGURE 3.1: Schematic diagram showing the ambiguity in geological models (black) which extend to ± infinity along the y-axis. Thin, shallow structures produce the same gravity anomaly as a horizontal cylinder at greater depth. Diagram is not to scale.

3.3 Synthetic gravity models

It is important to assess the uncertainties associated with each variable and ignore those that are insignificant to the overall result. Here, I use a range of synthetic 2D models to examine the sensitivity of ice-thickness:

- Density variations
- Internal bodies within the ice
- Complexity of geological features (i.e. sub-glacial till/surface debris)

In order to examine how different model configurations affect model-derived ice thickness, a reference shape is required from which comparisons can be made. The ideal shape for the synthetic models is one that follows the shape of a valley glacier. A parabolic residual anomaly with an amplitude of 15 mGal is used as the reference anomaly, while the maximum thickness of a parabolic ice body is 300 m. This way, the uncertainty in ice thickness relative to a reference surface can be tested. After assessing the relative importance of these features in the synthetic models, 2D gravity models from the Tasman Glacier are presented. 2D models were generated using the GM-SYS package, part of Geosoft's 'Oasis Montaj' software, following the procedures of Talwani et al. (1959). 2D models are oriented in x-z space where x is profile distance in metres and z is depth in metres. The bodies extend to infinity in the ± y-direction and also extend ± 30,000 km in the x-direction to eliminate edge effects.

3.3.1 Density variations

Three main materials are typically used in temperate glacier gravity models; these are ice, till and bedrock (e.g. Watson (1995)). Glacier ice typically has a density range of 830 - 917 kgm^{-3} where temperate glacier ice (near 0 °C) is usually taken as 917 kgm^{-3} (Cuffey and Paterson, 2010). Till densities range from 2000 - 2300

kgm^{-3} (Broadbent, 1973). Basement samples of greywacke have a density range of 2640 kgm^{-3} (Tenzer et al., 2011) to 2700 kgm^{-3} (Broadbent, 1973). Table 3.1 (adapted from Watson (1995)) summarises the densities used in gravity modelling studies for temperate valley glaciers as well as the densities used for this study.

TABLE 3.1: Summary of the densities used in temperate valley glacier gravity studies. Units are in kgm^{-3}.

Densities used for temperate valley glaciers

Author	Ice density (kgm^{-3})	Till density (kgm^{-3})	Basement density (kgm^{-3})
Krimmel (1970)	900	-	2670
Broadbent (1974)	920	2200	2700
Stern (1978)	920	2200	2800
Claridge (1983)	900	2200	2700
Watson (1995)	900	2400	2670
This study	910 ± 10	2200 ± 200	2670 ± 30

Ice density

Here I explore the effect that ice density variations have on modelled ice thickness. Using a synthetic forward model, Figure 3.2 demonstrates the response of ice thickness to changes in ice density (910 ± 10 kgm^{-3}) based on a simple 'ice over bedrock' model. Assuming a parabolic valley profile with a maximum ice thickness of $\sim$ 300 m, an error in ice density of 910 ± 10 kgm^{-3} represents a 286 ± 5 m or ±2% error in maximum ice thickness. This is summarised in Table 3.2.

TABLE 3.2: Errors in density and ice thickness for a synthetic gravity model of ice over bedrock.

Uncertainty in ice depth for variable ice density

Ice density (kgm^{-3})	RMS error (mGal)	Depth (m)
900	0.124	282
910	0.094	286
920	0.131	291

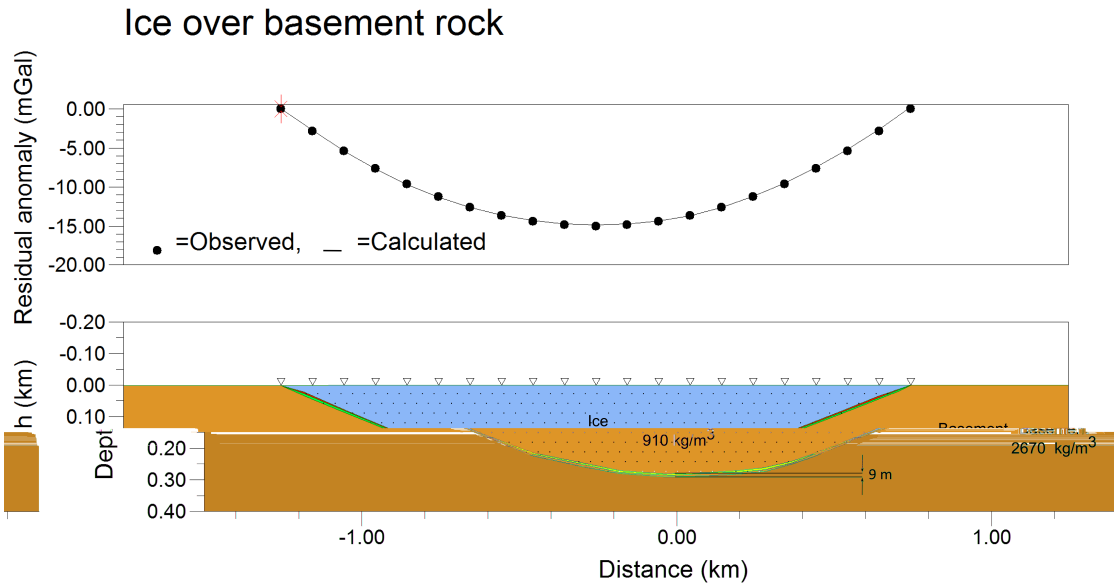

FIGURE 3.2: Top panel: Observed (black circles) and calculated (solid line) gravity in response to the forward model. Bottom panel: A synthetic gravity model of ice (blue) over basement rock (orange). Red and green regions reflect the change in ice thickness due to changes in ice density.

Till density

Holding the densities of ice and basement rock constant, a forward model was generated to investigate ice-thickness variations due to changes in till density (Figure 3.3). Initial bounds on the thickness of a sub-glacial till layer for the Tasman Glacier are constrained at $50 - 620$ m by a seismic line south of the present-day Tasman Glacier Kleffmann et al. (1998). Here, a mean till thickness of 300 m is used for this synthetic model. It is worth noting that the addition of a till layer forces the ice thickness to decrease slightly (Table 3.3) relative to an ice over bedrock scenario (Table 3.2). (Till thickness changes will be explored later in section 3.3.3). The uncertainties in till density (± 200 kgm^{-3}) are an order of magnitude larger than those for ice (± 10 kgm^{-3}) corresponding to a larger ice-thickness variation. Figure 3.3 highlights the errors in till density of 2200 ± 200 kgm^{-3} which correspond to maximum ice thicknesses of 261 ± 17 m, equivalent to a 7% error (Table 3.3).

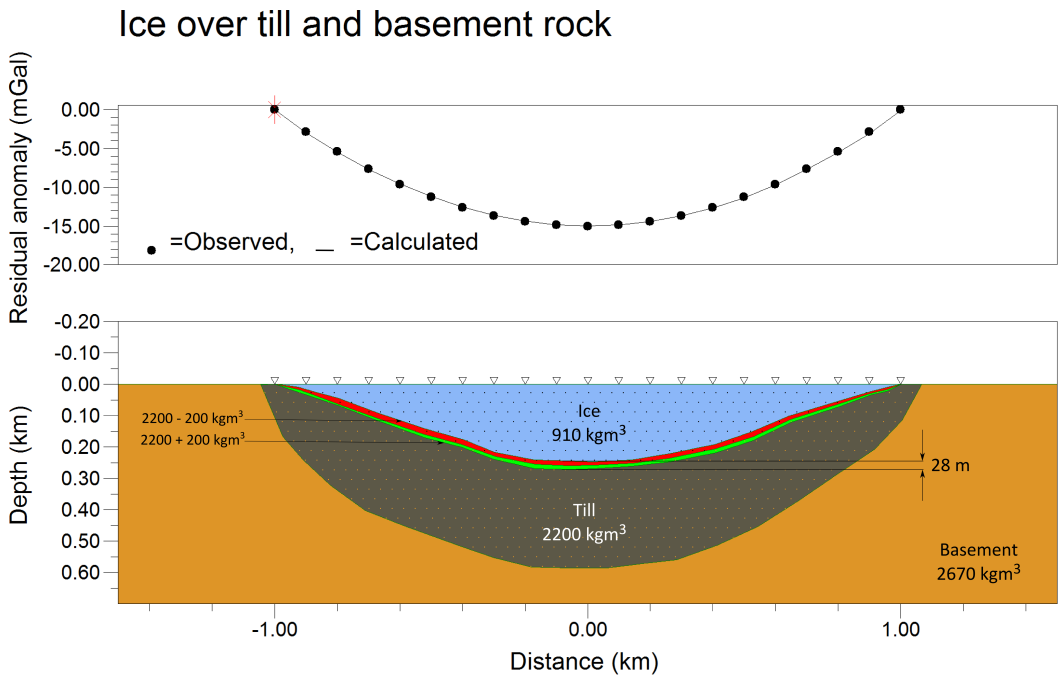

FIGURE 3.3: Top panel: Observed (black circles) and calculated (solid line) gravity in response to the forward model. Bottom panel: A synthetic gravity model of ice (blue) over till (grey) and basement rock (orange). Red and green regions reflect the change in ice thickness due to changes in till density.

TABLE 3.3: Summary of the errors in density and depth for a synthetic gravity model of ice over till and bedrock.

Uncertainty in ice depth for variable till density

Till density (kg/m^3)	RMS error (mGal)	Depth (m)
2000	0.058	244
2200	0.063	261
2400	0.086	272

Basement density

Holding the densities of ice and till constant, a forward model can be used to investigate the effect of uncertainty in basement density on the ice thickness estimate (Figure 3.4). A density range of 2670 $\pm$ 30 kgm^{-3} was chosen to represent greywacke density (Tenzer et al., 2011; Broadbent, 1973). Figure 3.4 displays the result of varying basement density on modelled ice thickness. The resulting estimate is 262 $\pm$ 12 m equivalent to a 5% error (Table 3.4).

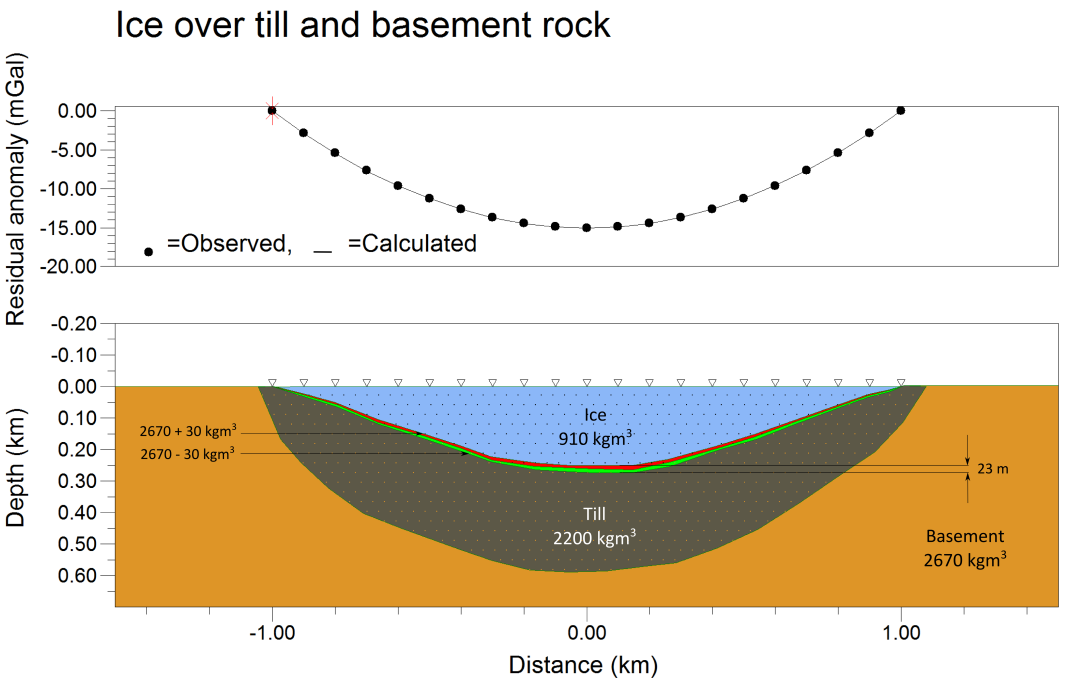

FIGURE 3.4: Top panel: Observed (black circles) and calculated (solid line) gravity in response to the forward model. Bottom panel: A synthetic gravity model of ice (blue) over till (grey) and basement rock (orange). Red and green regions reflect the change in ice thickness due to changes in basement density.

TABLE 3.4: Summary of the errors in density and depth for a synthetic gravity model of ice over till and bedrock.

Uncertainty in ice depth for variable basement density

Basement density (kgm^{-3})	RMS error (mGal)	Depth (m) (m)
2640	0.085	274
2670	0.039	262
2700	0.054	251

Errors in modelled ice thickness are linked to density contrasts; lower uncertainties in density (e.g. ice or basement rock) are associated with smaller ice-thickness errors (2% and 5 % respectively) while higher uncertainties in density (e.g. till) are associated with larger ice-thickness errors (7%). These values provide a first-order constraint on the ice-thickness uncertainties expected for the Tasman Glacier models.

3.3.2 Modelling features of the anomaly

A prominent feature in the Tasman residual anomaly is a 'residual ridge' within the overall U-shaped residual anomaly. This high region is present in the lower transects of the glacier (lines 100-400) (Figure 2.16). The ridge has an amplitude of approximately 6 mGal and a wavelength of 1000 m in the lower section of the glacier. This amplitude is larger than the measurement error (±1.18 mGal) and thus may be interpreted as a geologic structure. To investigate possible explanations for the residual ridge I explore how entrained bodies or changes in basement shape affect the residual anomaly. This subsection explores a range of synthetic models which may cause such a feature.

Internal bodies

The most likely source for this residual 'ridge' is an anomalous high density body either at depth or near the surface. Due to the high erosion rates and extensive coverage of surface debris over the study area, it is possible that the localised high may be due to entrained sediments. Entrained sediment of sub-glacial origins has been shown to produce internal 'debris ridges' up to 50 m across (Jansson and Iiolmlund, 2000). It is also possible that debris from events such as the Mt. Cook rock avalanche in 1991 (Owens, 1992), which covered an extensive area of the Tasman Glacier, may have become partially entrained in the Hochstetter ice fall crevasses or in the Grand Plateau accumulation area. Subsequent entrainment of debris may have led to an englacial position within the glacier.

An entrained debris ridge may be approximated as a horizontal cylinder of till (2200 kgm^{-3}) surrounded by glacial ice (910 kgm^{-3}) (Figure B.1 in Appendix A). To recreate the same amplitude (6 mGal) and wavelength ($\sim$ 1000 m) we see in the true residual anomaly, the cylinder has a diameter of 280 m and is centred at approximately 140 m depth. The top of the body intersects the glacier surface and extends to $\pm\ \infty$ in the y-direction.

Alternatively, a vertical rectangular prism may be appropriate (Figure B.2 in Appendix A). The length and width of the body is 400 m and 160 m respectively,

centred at approximately 200 m depth. The residual anomaly peak spans approximately 600 m but has a sharper peak compared to Figure B.1. The top of the body intersects the glacier surface and extends to $\pm \infty$ in the y-direction.

Basement highs

A basement ridge which is relatively resistant to erosion could also produce a localised peak in the residual anomaly. A basement high was modelled using a density of 2670 kgm^{-3} surrounded by glacial ice (910 kgm^{-3}) (Figure B.3 in Appendix A). The height and base-width of the ridge required to produce a peak of 6 mGals was 300 m and 400 m respectively. A peak with an amplitude of 6 mGal spans approximately 800 m producing a much broader response compared with Figures B.1 and B.2 as well as the 400 m wavelength we see in the true residual anomaly. This is because the ridge is positioned much deeper than either of the internal bodies considered (Figures B.1 and B.2). By comparing the relative weighting of internal till bodies with respect to basement highs, we can see that bodies nearer to the surface produce a larger amplitude/shorter wavelength response in the residual anomaly, whereas deeper features such as the basement high produce a smaller amplitude/longer wavelength response. Figure 3.5 demonstrates the cumulative effect of a horizontal cylinder and then a basement ridge on the residual anomaly. The majority of the anomaly response is due to the cylinder which lies at 140 m depth and raises the anomaly by 5.1 mGal (lower peak) while the basement ridge at approximately 250 m depth raises the anomaly a further 0.9 mGals (higher peak). The contribution from both features is represented by the higher peak.

The next section explores ice-thickness changes in response to changes in the thickness of till. Both sub-glacial till and surface debris cover are explored here.

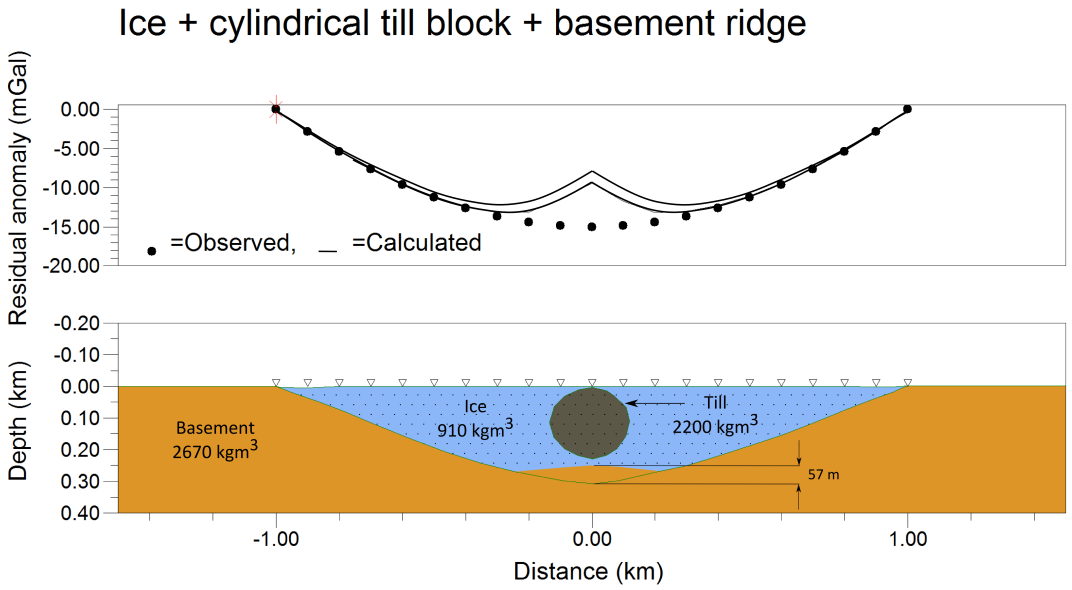

FIGURE 3.5: Top panel: Observed (black circles) and calculated gravity (solid lines) representing the response to (1) the internal till body (lower peak) and (2) the internal till body + basement ridge (higher peak). Bottom panel: A synthetic gravity model of ice (blue) over basement rock (orange). Internal till bodies are grey.

3.3.3 The effect of till

The term 'till' is used to describe the unconsolidated sediments which are deposited by a glacier (Cuffey and Paterson, 2010). The thickness, porosity and saturation of till are important constraints for glacier flow, yet these attributes are difficult to quantify due to the inaccessibility of the material (Boulton and Hindmarsh, 1987; Cuffey and Paterson, 2010). Surface debris cover is another form of till which may be an important control on the mass-balance of debris-covered glaciers (Anderson and Mackintosh, 2012).

Here, I present a discussion on the effects of (1), a varying sub-glacial till thickness and (2) a varying surface debris cover on the overall ice thickness of a typical valley glacier. Initial constraints on sub-glacial till thickness are 50 - 620 m from Kleffmann et al. (1998) while a surface debris cover of $\sim$ 5-8 m is constrained through seismic refraction results (Section 2.3.2). These bounds will be used to

quantify minimum and maximum ice-thickness changes for the following synthetic models.

Sub-glacial Till

Three sub-glacial till models are presented here. The models (based on evidence from Broadbent (1973)) have till thinning towards the glacier sides and thickening towards the centre, constrained by Kleffmann et al.'s results. All models have an initial reference shape approximating a parabolic profile. The maximum thickness of ice in these models is 300 m.

The introduction of a till layer forces the ice thickness to decrease for all models. The thickness of sub-glacial till varied between the range 50 - 620 m. Ice thickness was adjusted to match the offset residual anomaly due to the introduction of the till layer. Figure B.4 demonstrates that for a minimum till thickness of 50 m the ice thickness decreases by 7 m (14%) in the centre of the profile. Accordingly, an average till thickness value of 300 m forces an ice-thickness decrease of 41 m (14%) due to the till layer (Figure 3.6), while a maximum till thickness of 620 m forces a decrease in ice thickness by 71 m (24%) (Figure B.5). For an ice thickness similar to the Tasman Glacier ($\sim$ 600 m) a 620 m till layer forces a decrease in ice thickness of 84 m or 14%. This last result demonstrates that ice thickness reductions are proportionally less for thicker bodies of ice relative to the synthetic models presented here.

These models demonstrate that a sub-glacial till layer induces a reduction in modelled ice-thickness. The most extreme case shows the modelled ice thickness decreasing by up to 71 m for a 620 m thick till layer, suggesting that ice thickness is highly dependant on the thickness of till beneath the glacier. When drawing conclusions on the uniqueness of ice thickness for the Tasman Glacier, one must consider two points. The first is that the thickness of till beneath the Tasman Glacier is poorly constrained (Broadbent (1973)). Therefore uncertainties in ice thickness are rather large due to the range of possible till thickness values obtainable from Kleffmann et al. (1998). Second, the maximum ice thickness for the

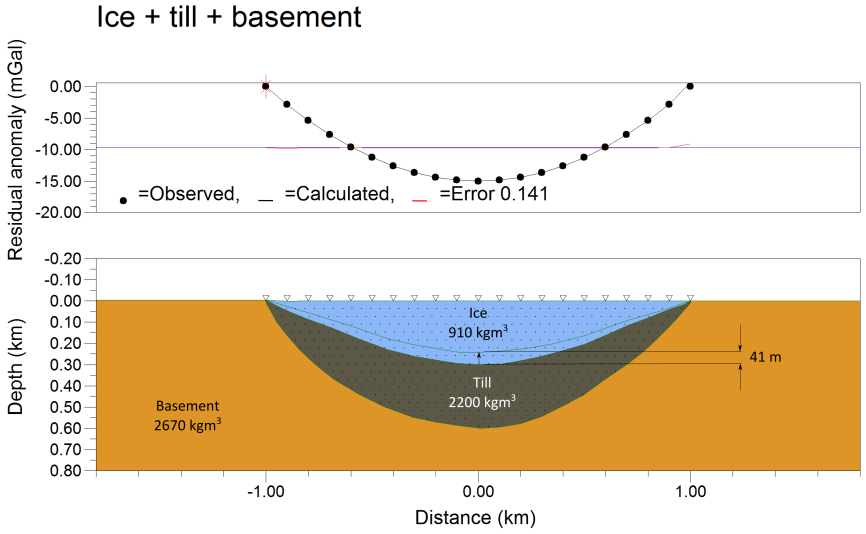

FIGURE 3.6: A synthetic model demonstrates the effect of a till layer on the changes in ice thickness. Observed gravity is shown by black circles while the calculated residual anomaly is given by a solid black line (top). The original ice/bed surface is marked by a solid black line. Adding a 300 m layer of till causes an decrease in ice thickness of 41 metres.

Tasman Glacier is more than double that of the synthetic models (Section 3.4.1). Therefore, ice thickness changes are proportionally reduced for a thicker glacier compared to the thinner synthetic models presented above.

Surface debris

A variable surface debris thickness of 4.6 to 7.6 m was obtained from the refraction survey adjacent to Ball Hut (Section 2.3.2). The density of this layer is relatively low (1510 ± 190 kgm^{-3}) which, in combination with a thin surface, meant that a negligible response ($\pm$ 0.1 mGal) was observed in the residual anomaly even for the maximum thickness/highest density contrast scenario (Figure 3.7).

3.3.4 Summary of synthetic models

The following features were observed in synthetic models for a typical parabolic shaped glacier with a maximum thickness of 600 m:

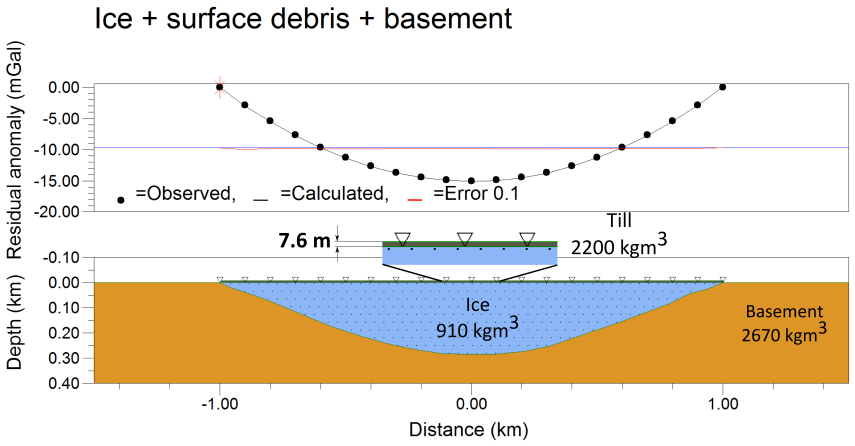

FIGURE 3.7: Top panel: Observed (black circles) and calculated gravity (solid line). Bottom panel: A synthetic gravity model of surface till (grey) over ice (blue) over basement rock (orange).

- Density variations in ice/till/basement caused ice-thickness variations of ±28 m to ±67 m equivalent to a 4.7% to 10.9% change respectively.

- Entrained sediment and/or basement highs can reproduce the residual 'ridge' seen in the lower residual anomalies of the Tasman Glacier. The size, shape and depth of these bodies influences the amplitude and wavelength of the residual anomaly. Models are non-unique due to uncertainties in density and shape of the bodies.

- The presence of a uniform sub-glacial till layer causes an ice thickening of 46-254 m depending on the thickness of till. However I also consider a variable till thickness: this causes a reduction in ice thickness of 0-50 m and may be a more likely distribution for the Tasman Glacier.

- The presence of surface debris is too thin to have any significant effect on ice thickness.

3.4 Tasman gravity models

Here, I explore the ice-thickness distribution of the Tasman Glacier through both 2D and 3D gravity models. The models presented below are all non-unique solutions to the ice thickness of the glacier; however, constraints have been employed where possible to minimise the uncertainty in the models. These include constraints on density through the seismic refraction survey (Section 2.3.2) as well as depth constraints on the Ball Hut transect (equivalent to line 900) through seismic reflection studies by Broadbent (1973).

A total of twelve gravity transects, perpendicular to glacier flow, are modelled both in 2D and 3D using Geosoft's GM-SYS software. Four of the twelve 2D models are presented in this chapter due to the similarity between adjacent transects. Transects are numbered T_100 and T_200 for the terminus transects and L_100 to L_1000 for the main glacier, increasing to the north (Figure 2.1). Lines L_900, L_300 and the terminus transects T_100 and T_200 are presented, while the remaining models are seen in Appendix B. Line 900 is presented to compare ice-thickness results with Broadbent's 1973 Ball Hut survey. Line 300 is presented to explore the causes behind a residual 'ridge' seen in a number of transects. The terminus lines are then presented to explore the ice thickness near the actively calving face of the Tasman Glacier.

3.4.1 2D models

I use a forward modelling approach for the 2D models and consider the gravitational influence of three units: ice, till and basement rock (densities are summarised in Table 3.1). 2D models are displayed in two parts: an upper segment and lower segment. The upper segment shows observed gravity (black circles), calculated gravity (black line) and the root-mean-square error between these (red line) with units in mGals. The error associated with each residual anomaly point is ± 1.18 mGal as summarised in Appendix A. The number of observed gravity stations for each transect also represents the number of nodes used to describe each interface.

However, as no gravity measurements were made on bedrock surfaces, ice thickness was forced to zero at the glacier sides. The bottom segment displays the three units mentioned above which produce the calculated gravity response, given by negative depth (km) as the profiles are above sea level.

All models have a horizontal position in NZTM 2000 Eastings (m) and are tied to the highest observed gravity point (black circle with red star) in an attempt to tie each survey to a site with zero ice thickness. For most transects, these sites were impossible to occupy due to the steep moraine walls inhibiting a safe gravity measurement.

Ball Hut transect (L_900)

The Ball Hut transect is a well established line that has been occupied by several studies over the last few decades e.g. (Skinner, 1964; Anderton, 1973; Broadbent, 1973; Watson, 1995) (Figure 3.8). Ice thickness has been constrained at this location through both reflection seismic surveys (Broadbent, 1973) and gravity studies (Claridge, 1983; Watson, 1995) providing an important tie mark for this study. Consequently, the survey was designed to incorporate the Ball Hut transect with the aim of constraining ice thickness for this part of the glacier.

Line 900 was constructed using ice-thickness constraints from the Ball Hut transect. To achieve this, Broadbent's seismic line was digitised and compared with the gravity anomaly obtained for line 900. Assuming Broadbent's seismic line was accurate, a close match was expected between the seismic model and the residual anomaly. However, the direct use of Broadbent's seismic line was complicated by two factors.

First, Broadbent's seismic model from 1973 was based on a glacier surface ∼75 m higher than today. A significant vertical lowering of this surface over the last 40 years meant that the observed gravity values were relatively lower compared with the gravity response form Broadbent's seismic model. Assuming a reduction in ice loss occurred across the entire transect over this period, a uniform

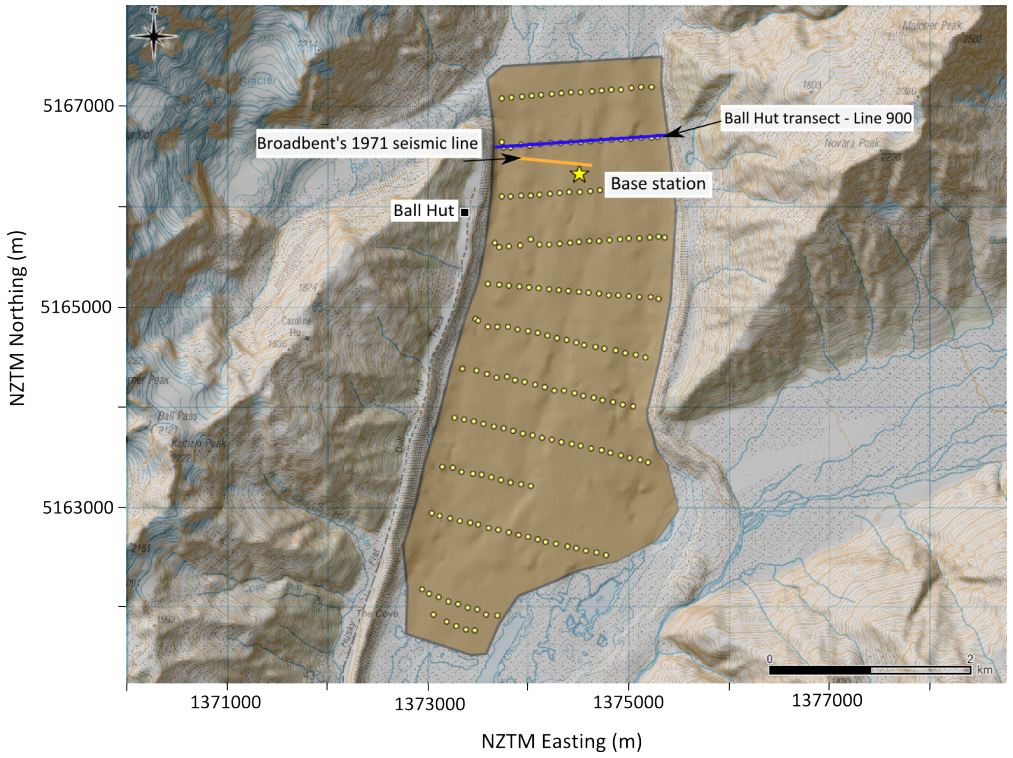

FIGURE 3.8: Site map for the Tasman Glacier indicating the Ball Hut transect in blue (Line 900) and Broadbent's seismic line in orange. Yellow circles mark the location of each gravity station used in this study while the yellow star represents the base station for the survey. The Ball Hut shelter is marked by a black square on the western side of the glacier.

correction was made in ice thickness of +75 m to restore the glacier surface to its 1973 elevation. Second, the seismic survey conducted by Broadbent only extended across the western side of the glacier. Thus the eastern portion of the ice/till and till/basement interfaces were inferred. These two factors led to Figure, 3.9 - a reconstruction of Broadbent's seismic model relative to our residual anomaly. A large discrepancy between the model and our data is seen on the eastern part of the glacier where till thicknesses range from 100 to 200 metres. This range is thought to be related to errors involved in picking seismic events (Broadbent, 1973).

We adapted the forward gravity model for line 900 to incorporate the constraints provided by Broadbent's seismic survey, while increasing the ice thickness on the eastern side of the valley to satisfy the observed and calculated gravity response (Figure 3.10). This meant that the cross sectional area obtained for the

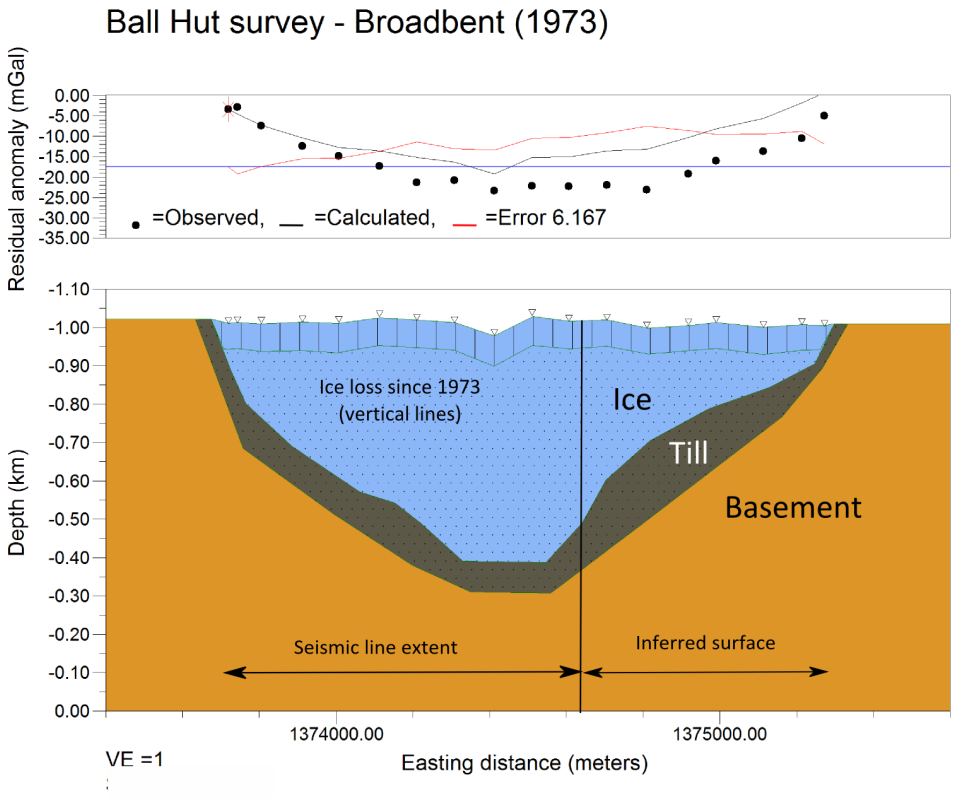

FIGURE 3.9: Broadbent's digitised seismic model for the Ball Hut transect on the Tasman Glacier. The model is composed of ice (910 kgm^{-3}) over till (2200 kgm^{-3}) and basement (2670 kgm^{-3}). The reduction in glacier elevation since 1973 is shown by vertical lines. Broadbent's seismic line extends across the western part of the glacier while the inferred ice/till and till/basement interfaces occupy the eastern side. Our observed residual anomaly is shown by black circles, calculated gravity is shown by a solid black line and the root-mean-squared error (red line) represents the difference between the observed and calculated anomalies (top).

Ball Hut transect (6.9 $\times$ 10^5 m^2) was greater than Broadbent's estimate of 6.5 $\times$ 10^5 m^2.

Figure 3.10 shows the 2D model for line 900 which lies approximately coincident with the Ball Hut transect of Broadbent (1973). At a bearing of 085° it is also located within 400 m of the refraction seismic line used in this study (Figure 2.1) hence densities are well constrained here. The model is characterised by a symmetrical parabolic shape with a cross-sectional area of 6.927 $\times$ 10^5 m^2 (Table 3.5). The ice/till interface extends down to a depth of 295 m above sea level,

equivalent to a maximum ice thickness of 663 m. An entrained layer of till (up to 36 m thick) outcrops at the surface and a variable sub-glacial till thickness of 100 to 150 metres occupies the base of the glacier.

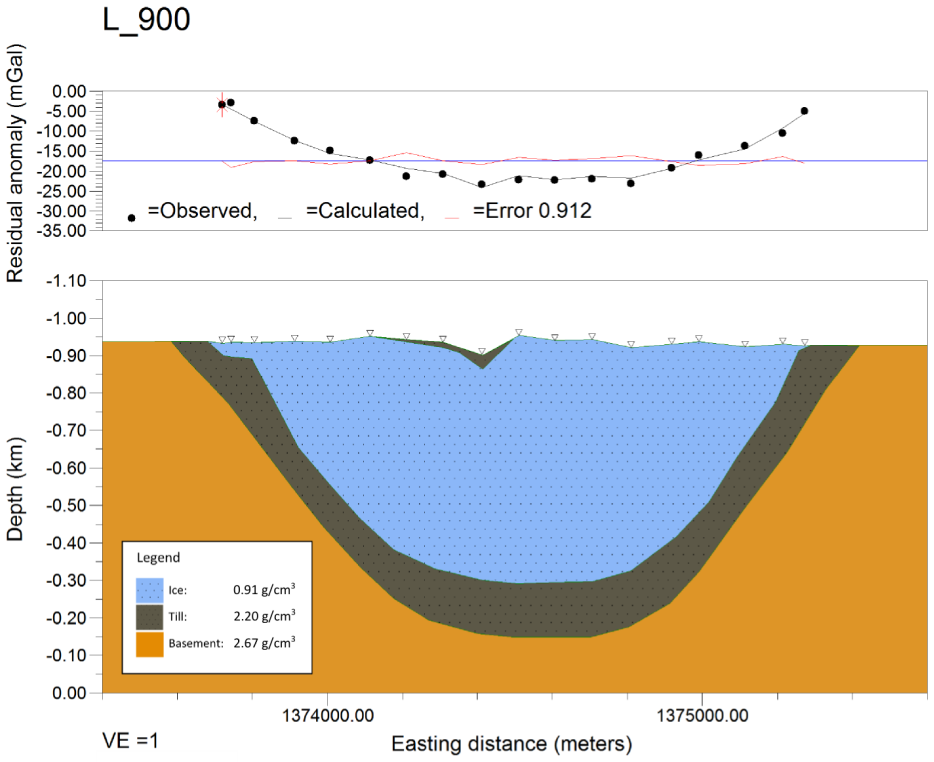

FIGURE 3.10: Adapted forward gravity model for line 900 on the Tasman Glacier. Observed gravity is shown by black circles, calculated gravity is shown by a solid black line and the root-mean-squared error (red line) represents the difference between the observed and calculated anomalies (top).

The residual 'ridge' (L_300)

Geomorphological evidence from unoccupied, present-day glacial valleys indicates that the cross-sectional shape of temperate valley glaciers typically follows a U-shape or catenary form (the shape of a chain suspended by each end) (Montgomery, 2002). Mathematically, the U-shape has also been shown to represent the cross-sectional shape of a steady-state glacier (e.g. Hirano and Aniya (1988)).

The majority of anomaly transects across the Tasman Glacier indeed follow the

U-shape typical of valley glaciers. However, a significant feature observed in many transects is the presence of a high 'ridge' of anomaly values (Figure 2.16). This feature extends in a north-south direction across several transects between lines L_100 and L_400. With an amplitude of approximately 6 mGal and a wavelength on the order of 1 km, the ridge cannot be explained simply through errors in the residual anomaly values, which are ± 1.18 mGals.

Here, I test glaciologically plausible cross-sections for the lower Tasman Glacier by attempting to fit the anomaly with a localised body of till entrained within the glacier (Figure 3.11). The relatively high density contrast between ice and till means that a body of till near the surface of the glacier causes a localised high in the residual anomaly (as observed in Section 3.3.3 for the synthetic models). Basement highs were also investigated in the synthetic models but were found to produce a small amplitude/long wavelength response on the residual anomaly. Furthermore, we expect to see a U-shaped bed for the Tasman Glacier, as was observed in the more northern transects, thus the possibility of a bedrock ridge was excluded from the models.

The body of till representing the residual 'ridge' seen in L_300 (Figure 3.11) has a substantial area (summarised in Table 3.5). The dimensions of the body are approximately 300 m wide and 70 m thick with a cross-sectional area of 17.975 $\times$ 10^3 m^2. This feature extends north and south into the adjacent models L_100, L_200 and L_400. The processes which allow such large volumes of sediment to be deposited over the glacier are discussed later in Chapter 4.

Tasman Glacier terminus

Many of the world's valley glaciers are currently calving into proglacial lakes (e.g. Benn et al. (2012)). The dynamic control on the calving behaviour of these glaciers is complicated by many factors such as lowering of the surface, lake level and temperature, buoyancy forces or the nature of the sub-glacial topography (e.g. Boyce et al. (2007)). For the terminus region of highly erosive valley glaciers, the sub-glacial topography often forms a steep, reverse slope to the overlying glacier

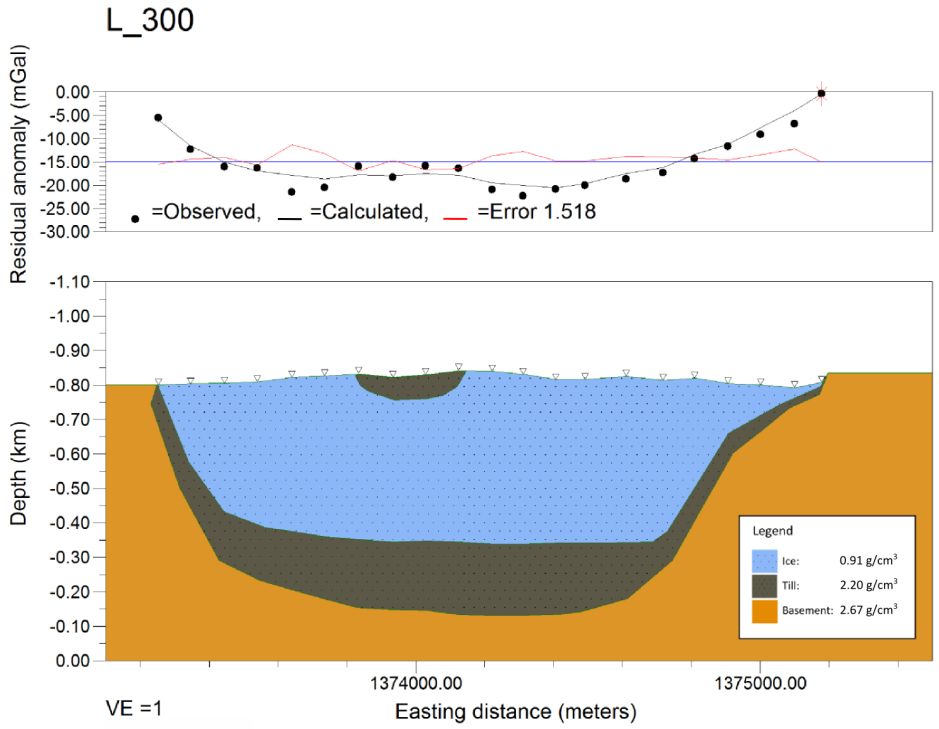

FIGURE 3.11: Forward gravity model for line 300 on the Tasman Glacier. A large (6 mGal) ridge in the residual anomaly is modelled using an entrained till body of density 2200 kgm^{-3}. Observed gravity is shown by black circles, calculated gravity is shown by a solid black line and the root-mean-squared error (red line) represents the difference between the observed and calculated anomalies (top).

surface (Alley et al., 2003b). The term used to describe this shape is a 'bed over-deepening' (Bennett and Evans, 2012).

The sub-glacial topography plays a role in the stability of the terminus region. The presence of an irregular bed surface may allow 'pinning points' to stabilise the glacier terminus (Warren and Glasser, 1992) while an over-deepening of the sub-glacial topography may result in an instability in the terminus region (Bennett and Evans, 2012).

Geophysical and geomorphological evidence on the Tasman Glacier is suggestive of the presence of a reverse bed slope leading up to the present-day terminus (e.g. Anderton (1973); Dykes and Brook (2010)). Here, I present 2D gravity models over the terminus region to address this feature. The two lines presented (Figures

3.13 and 3.14) show a significant reduction in ice thickness compared to the more northern lines suggesting a reverse bed-slope profile exists. These transects are the southernmost lines for this study, positioned within 200 m of the terminal face. The approximate positions of the two transects (T_200 and T_100) are marked by solid black lines in Figure 3.12. The distance between the two transects is approximately 200 m, while the length of line T_100 is 400 m.

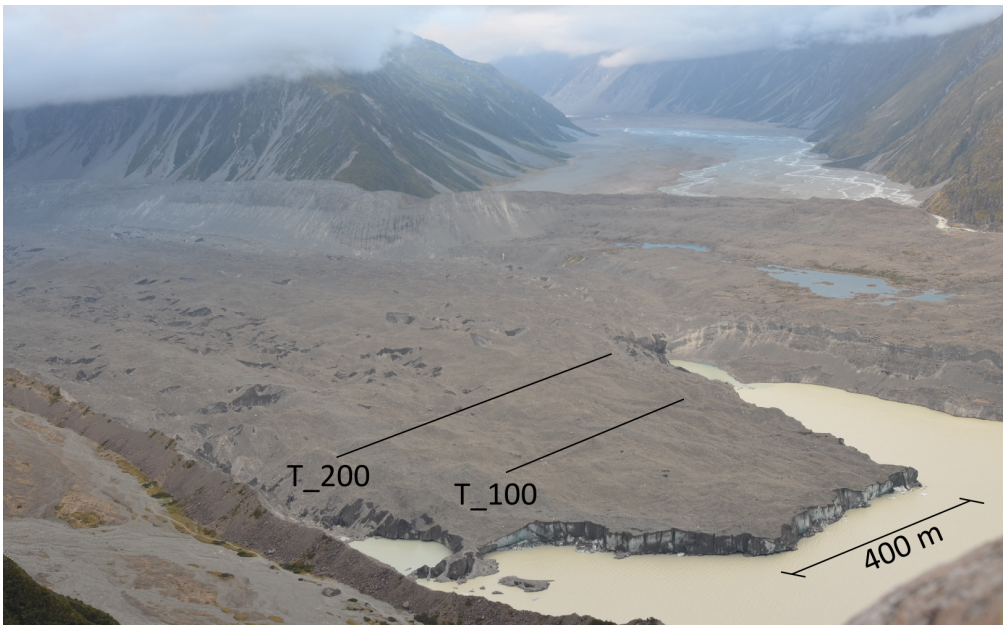

FIGURE 3.12: An oblique photo taken on 22nd February 2013 shows the terminus of the Tasman Glacier during this survey. Photo courtesy of Brian Anderson.

Line T_200

Line T_200 is the more northern of the two terminus transects, approximately 250 m upstream of Line T_100. The ice/till interface extends down to a depth of 546 m above sea level, equivalent to a maximum ice thickness of 220 m. The ice has a cross-sectional area of 9.18×10^4 m^2 (Table 3.5). The model is characterised by a asymmetrical parabolic shape, and contains an entrained layer of till (up to 40 m thick) near its surface and a sub-glacial till layer up to 45 m thick. T_200 has a significantly deeper section on the eastern side (approximately 60 m thicker than the western side) which cannot be accounted for by an entrained till body.

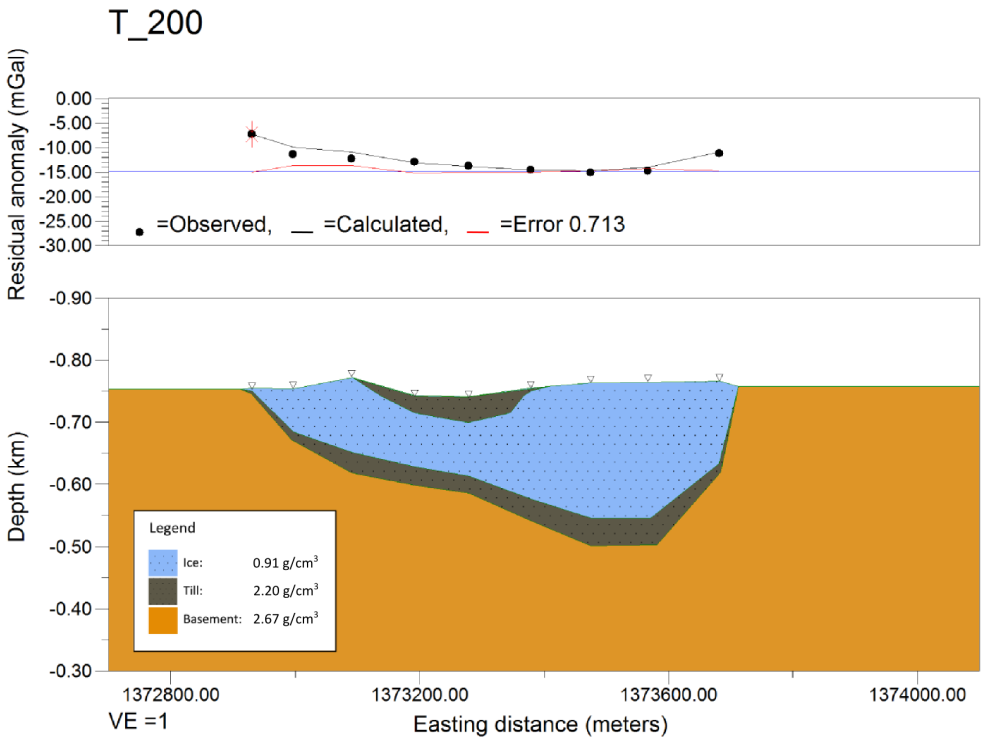

FIGURE 3.13: Forward gravity model for line T_200 on the Tasman Glacier. Observed gravity is shown by black circles, calculated gravity is shown by a solid black line and the root-mean-squared error (red line) represents the difference between the observed and calculated anomalies (top).

Line T_100

Line T_100 is the southern-most terminus transect, approximately 200 m from the present-day calving face. Because T_100 is so close to the calving face, the 2D assumption that bodies extend to infinity in the ± y-direction may be violated. The modelled ice/till interface extends down to a depth of 662 m.a.s.l., equivalent to a maximum ice thickness of 92 m. The ice has a cross-sectional area of 2.64 × 10^4 m^2 (Table 3.5). The profile is characterised by a broad and near-symmetrical parabolic shape which contains an entrained layer of till (up to 30 m thick) near its surface and a sub-glacial till layer up to 16 m thick.

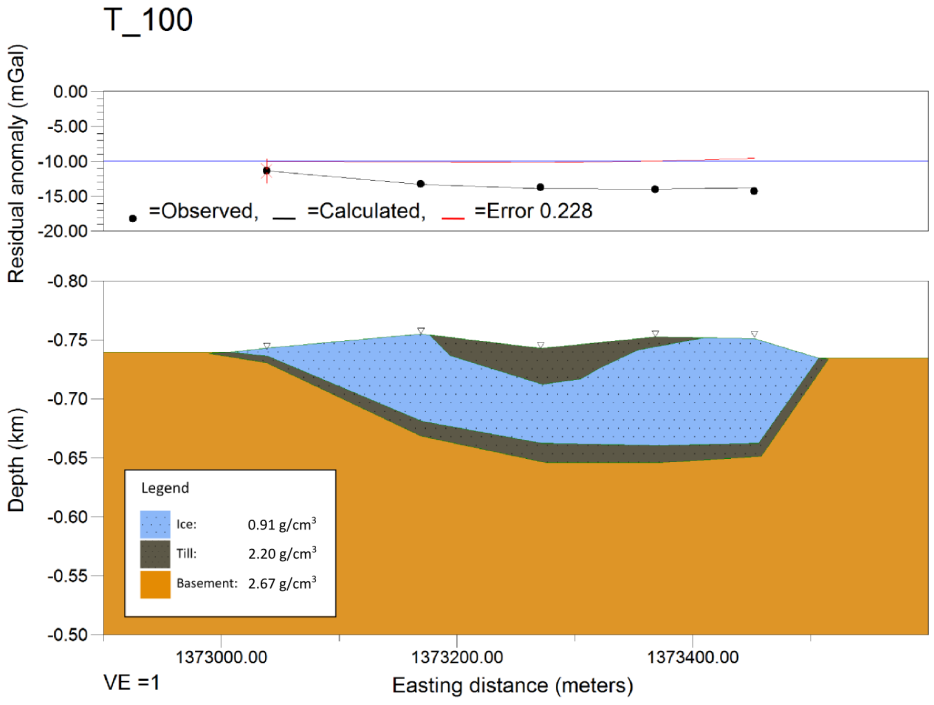

FIGURE 3.14: Forward gravity model for line T_100 on the Tasman Glacier. Observed gravity is shown by black circles, calculated gravity is shown by a solid black line and the root-mean-squared error (red line) represents the difference between the observed and calculated anomalies (top).

2D model summary

Four representative 2D models have been presented to show (1) the typical valley shape and expected ice thickness of the glacier compared with previous surveys (Broadbent, 1973), (2) the effect an entrained body of till has on a residual 'ridge' observed across several transects and (3) the ice-thickness distribution of the terminus region of the Tasman Glacier.

The entire survey area, encompassing all twelve 2D transects, is presented for the sub-glacial bed elevation in three-dimensions in Figure 3.15. The general shape of the 3D plot shows a typical U-shaped valley with maximum ice thicknesses of 722 m, gradually thinning to 92 m at the terminus. A prominent reverse bed-slope is also seen between L_300 and T_100 where a reduction in ice thickness occurs. Lines 400 to 600 are noticeably shallower by up to 150 m than the adjacent profiles. This feature will be explored in more detail in Section 3.4.2 and discussed in Chapter 4. Table 3.5 summarises the main features for each transect.

Table 3.5: Summary of the ice thickness and glacier area data for transects over the Tasman Glacier. Maximum ice thickness and glacier area are calculated on the assumption that the models extend to infinity in the ± y-direction.

Tasman Glacier transect summary

Line #	Bearing (°)	Max ice thickness (m)	Glacier area ($\times 10^5$ m^2)	Entrained till area ($\times 10^3$ m^2)
1000	085	722	8.846	10.717
900	086	663	6.927	4.856
800	087	692	7.450	4.968
700	086	675	8.486	18.004
600	095	461	6.184	4.584
500	102	510	6.531	9.466
400	103	467	5.436	10.166
300	103	501	7.159	17.975
200	103	419	5.895	11.526
100	103	351	3.799	9.254
T200	105	220	0.9184	9.954
T100	105	92	0.2636	3.647

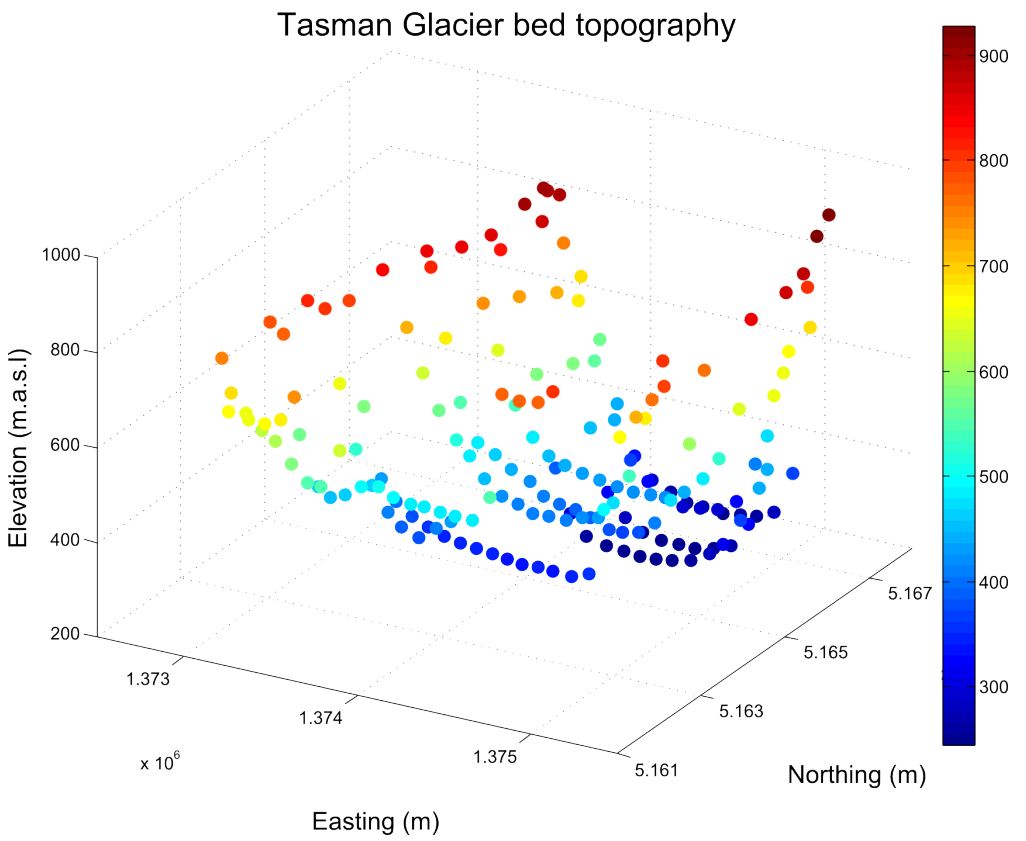

FIGURE 3.15: Bed topography for the Tasman Glacier derived from 2D gravity models. Coloured circles mark the elevation of each node (metres above sea level) for each gravity station. X and Y axes are in NZTM 2000 Eastings and Northings respectively.

3.4.2 3D models

Both structural inversion and forward modelling approaches are used to produce 3D models, where a three-layer scenario of ice over till and bedrock is considered. Model inputs include the surface topography of the glacier, an interpolated bed and basement topography (derived from 2D models) and the gravity residual anomalies. The main bed features and model differences are described in the 3D models.

Structural inversion

The gravity structural inversion approach uses a bed topography surface and alters it to minimise the misfit between the calculated gravity response and the observed gravity. A structural inversion was made for an interpolated bed topography (derived from 2D model transects) with parameters summarised in Table 3.6. A maximum of five iterations were set for the inversion, with each node allowed to vary by upper and lower bounds of 35 m. Inputs are constrained where possible by results obtained from the 2D models (e.g. uncertainties in ice thickness and/or the uncertainty in the residual anomaly points). The model required two iterations before terminating due to the mean error diverging from the limit of 1.18 mGal. The structural inversion results described below are not valid, but are compared with the forward 3D model. The inverted ice/till interface (left-hand image in Figure 3.16) has a minimum and maximum elevation of 267 m.a.s.l. and 687 m.a.s.l. respectively and a mean value of 460 m.a.s.l.

Table 3.6: Summary of the inputs used for the structural inversion procedure in GM-SYS 3D.

Structural Inversion parameters	Value
Max. number of iterations	5
Convergence limit (mGal)	1.18
Lower High-cut limit	0.5
Upper High-cut limit	0.7
Regional offset	0
Upper Z bound (m)	35
Lower Z bound (m)	0
Max. change in Z (m)	35

Forward modelling

The forward modelling approach calculates the gravitational response from a model input using Taylor series expansion (Taylor, 1717). Again, an interpolated bed topography surface from the 2D surveys is used as the input model.

Five Taylor series terms were used for the forward calculation. The ice/till interface has minimum and maximum bed elevations of 254 m.a.s.l. and 700 m.a.s.l. respectively and a mean value of 490 m.a.s.l. (right-hand image in Figure 3.16).

Comparison between 3D models

Both the gravity structural inversion and forward models show similar features to the 2D models. However, the structural inversion model is not valid as the result diverged from the error range supplied. The reasons for this are unknown, but it is likely that a higher error margin would allow more freedom of movement for each node. Focussing on the northern section of the transects (3500–5500 m along the y-axis in Figure 3.16), both models indicate a bed over-deepening with ice thicknesses approaching 700 m in the centre of the glacier. South of the bed over-deepening, the models deviate slightly. For the forward gravity model, a high region of bed elevations ($\sim$ 450 m ice thickness) between 2500–3500 m along the y-axis extends across the entire width of the glacier. The forward gravity model shows a significant step in bed elevation of $\sim$ 100–140 m between the over-deepening and the raised bed while the structural inversion model produces a more subtle transition between the bed over-deepening and the raised bed ($\sim$ 50–70 m), indicating a more typical U-shape expected for valley glaciers. South of the raised bed (0–2500 m along the y-axis) both models indicate a gradual decrease in bed elevations ($\sim$ 500–550 m ice thickness) before increasing again towards the terminus. The terminus region has ice thickness values between 100–200 m. For the forward gravity model (0–1000 m along the y-axis) the bed slope tends to steepen more towards the terminus while the structural inversion has a more gradual increase in bed elevations towards the terminus. Ice thicknesses for both models near the terminus are $\sim$ 240 m.

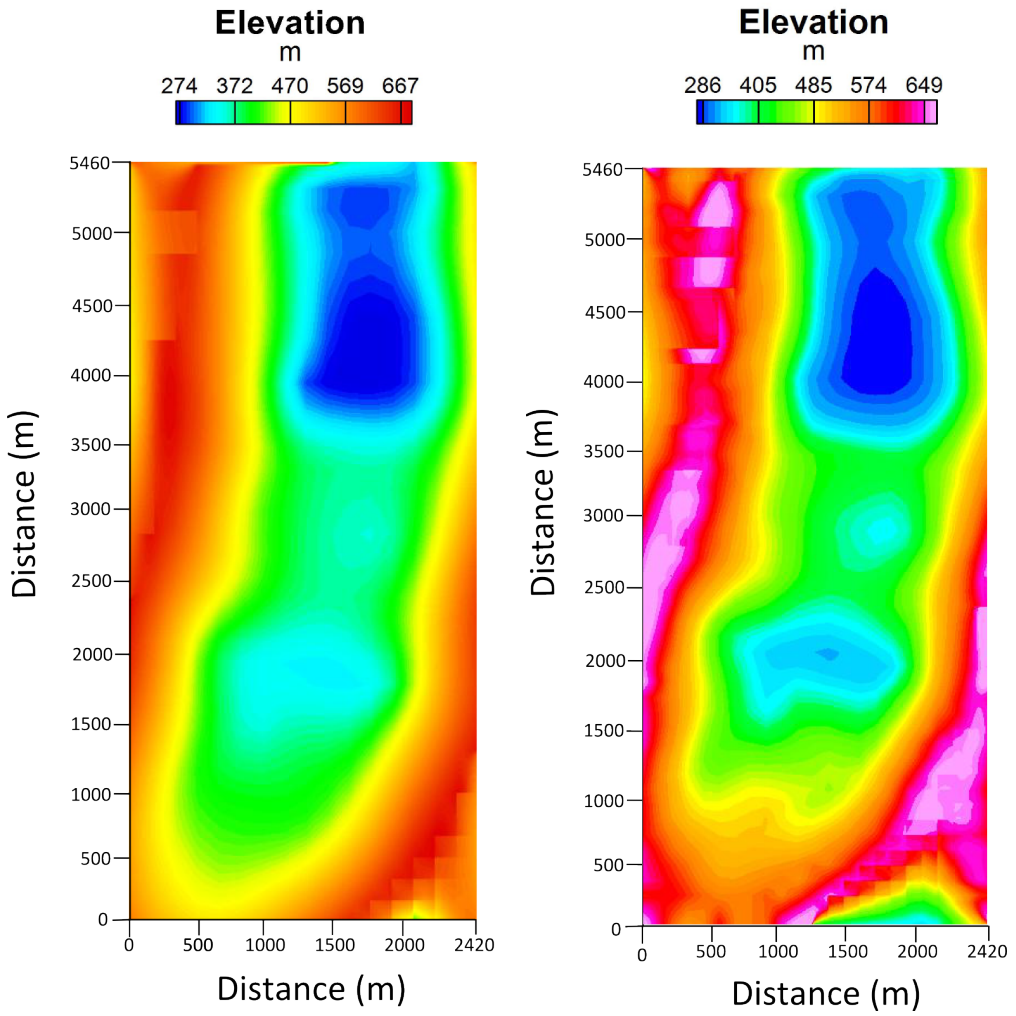

FIGURE 3.16: Map view of the ice/till interface for a gravity structural inversion (left) and a forward gravity model (right).

3D model summary

Two different modelling approaches (structural inversion and forward gravity) have been used to produce 3D models for the ice-thickness distribution of the Tasman Glacier. Because the structural inversion model diverged from the error limit, its validity is poor, thus the forward model is favoured here for discussion. The general bed shape is characterised by a U-shaped trough with (1) a large over-deepening in the northern section of the survey area (ice thicknesses approach 700 m), (2) an increase in bed elevation between lines 400 to 600 (ice thickness reduces

to $\sim$ 450 m), (3) a reduction in bed elevation south of line 400 (ice thicknesses of $\sim$500–550 m) and (4) a bed elevation increase towards the terminus where ice thickness is less than 100 m. Generally, the forward 3D model provides maximum ice thicknesses in good agreement with the 2D models. This is thought to be related to the 3D model being derived from 2D depth inputs. A more rigorous comparison between the 3D model and 2D models will be summarised in section 4.

Section 3.5 explores the application of ice-thickness data to glacier models. In particular I compare the 2D gravity results to an ice-thickness model based on a simpler version of Farinotti et al. (2009). The glacier model takes point data (derived from 2D profiles) as inputs to an ice-thickness model for the 'Central Southern Alps' region which includes the Tasman Glacier.

3.5 Ice volume estimation

This section uses a simplified version of Farinotti et al.'s method in the 2D model domain to estimate the ice-thickness distribution and volume of the Tasman Glacier in the 'Central Southern Alps' region. The mass flux model uses measured ice thicknesses (derived from gravity results) to produce an optimised ice-thickness distribution for the entire glaciated area of the Central Southern Alps. Put simply, the mass flux model is tuned. The optimisation is limited in its ability to model ice thickness as it only seeks to minimise the Root Mean Square Error (RMSE) between the calculated and measured ice thickness rather then find the most likely bed shape. The model requires physical constraints such as surface slope, a DEM of the glacier surface and the parameters A and C (equation 2.26) to calculate the best fitting ice-thickness distribution.

The performance of the model was limited by the optimisation for reasons previously mentioned, therefore manual tuning of the parameters A and C was required. A manual adjustment of the C parameter was made while A was held constant, in an attempt to more accurately constrain the ice-thickness distribution

for the Tasman Glacier. In this way, changes in the influence of basal sliding and other uncertainties could be assessed based on the linear fit between calculated and measured ice thicknesses. Excluding the terminus profiles (T_100 and T_200) resulted in a better fit. The manually adjusted parameter solutions for A and C as well as glacier geometry for the best fitting model are summarised in Table 3.7.

TABLE 3.7: Summary of the inputs used for the ice-thickness model in the Central Southern Alps.

Model parameters	Value
C	2.5
A	2.4×10^{-15}
Minimum slope	0.007
Slope median window	13
DEM median window	7
Max. ice-thickness (m)	700

An important control on maximum ice thickness in the model is the surface slope. Farinotti's equation (2.26) indicates that for small surface slopes (α) ice thickness (H) is increased in order to maintain the same ice volume flux (q_i). As α approaches zero H tends to infinity. For the Tasman Glacier, surface slopes near the terminus are low. A surface slope of 0.007 was used for the optimised model solution. Maximum ice thickness was set at 700 m based on maximum ice thicknesses obtained from this gravity survey. The DEM used in this model is based on topographical maps from 1986. Due to continued downwasting since then (Watson, 1995), the 1986 surface elevation of the glacier was $\sim$ 48 m higher than the 2013 surface.

Results from manual adjustment of the model parameters indicate that the modelled ice thickness underestimates observed ice thickness with a Root Mean Square Error (RMSE) of 148 m. The regression line has a positive y-intercept of 119 m, hence modelled ice thickness is overestimated relative to measured ice thickness (for values up to $x = 310$ m). For $x > 310$ m modelled ice thickness is underestimated relative to calculated ice thickness. The equation of the regression line is:

$$y = 0.613x + 119 \tag{3.1}$$

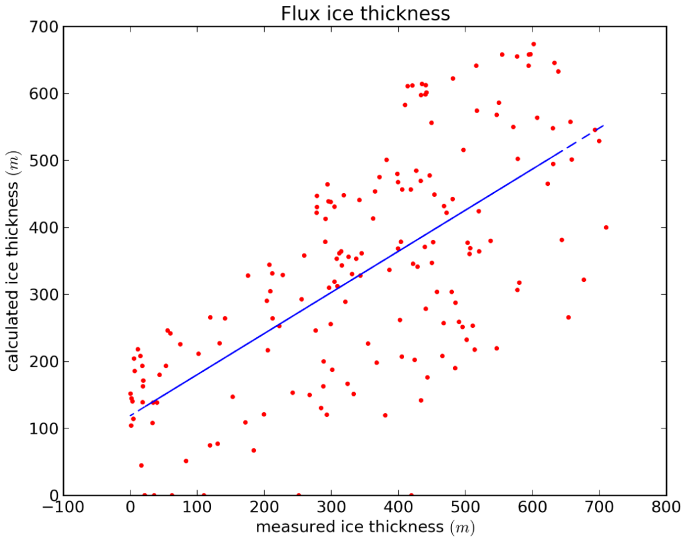

FIGURE 3.17: Plot showing calculated ice thickness versus measured ice thickness from gravity results. Blue line indicates line of best-fit with equation y = 0.613x +119 and RMSE of 148 m.

The underestimation of modelled ice thickness relative to measured ice thickness for $x > 310$ m is likely a result of several features. Firstly, cross glacier profiles for the Tasman Glacier are complicated by multiple tributaries delivering mass into the Tasman Glacier catchment (e.g. Rudolf and Darwin Glaciers). The simple assumption that the ice flux is distributed linearly with distance from the margin in each elevation band may be inaccurate. That is, the linear assumption doesn't provide enough ice flux in the glacier centre and so underestimates ice thickness there. Secondly, the ice thickness distribution favours a low RMSE value rather than finding an optimal ice thickness distribution with a slightly higher RMSE value. Thirdly, the DEM surface used in the model is based off aerial photography from 1986/87, hence the model is calculating an ice thickness relative to a glacier bed that is being overestimated relative to the measured values.

Modelled ice thicknesses for the Central Southern Alps display the main glacial valleys in the region (Figure 3.18). Tasman Glacier is the distinctly north-south

trending red/yellow area in the centre of Figure 3.18 which contains the majority of the Central Southern Alps ice. Maximum ice thicknesses approach 700 m in the centre while other areas of thick ice are also observed up-glacier.

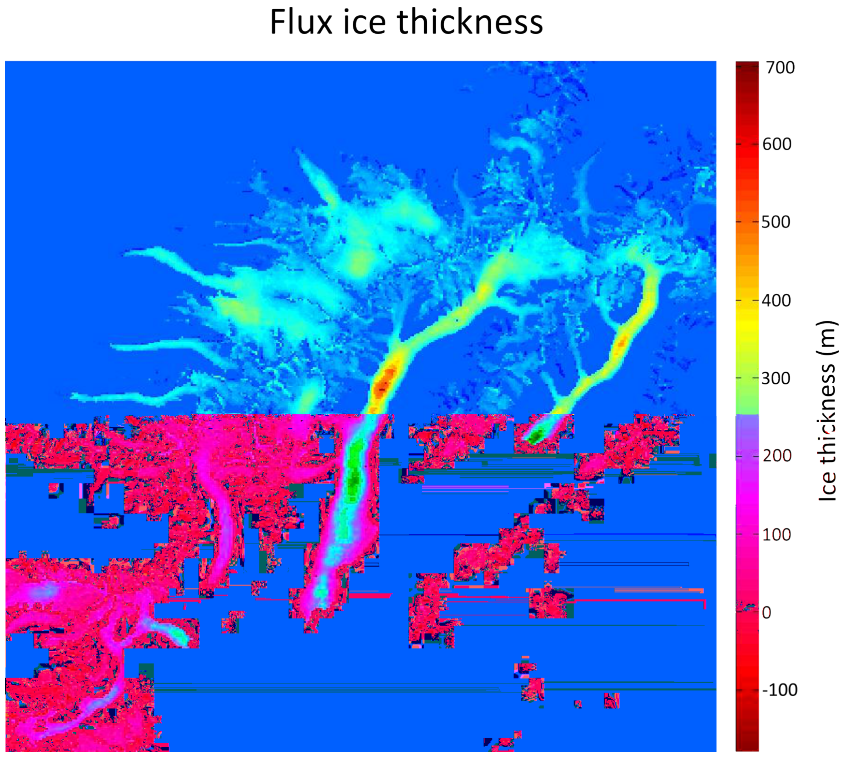

FIGURE 3.18: Map of the Central Southern Alps model domain showing ice thickness derived from the mass flux model using gravity derived ice-thickness measurements.

Here, 2D plots of ice thickness derived from the mass flux model are compared to gravity derived ice thicknesses for transects L_100 to L_1000. The plots show three surfaces: the 1986 DEM (blue line), the model bed (red line) and the measured bed from this study (black line) (Figures 3.19 and 3.20).

Comparison of the measured and modelled profiles demonstrate the trend given by the linear best fit (equation 3.1) that ice thickness is generally underestimated relative to our measured values. However for transects L_100 (in Figure 3.19) and L_600 (in Figure 3.20) the model overestimates ice thickness by $\sim$ 100 m near the glacier centre. Overall, the plots have an RMSE of 148 m between the modelled and calculated ice thickness.

The final flux ice volume of the Tasman Glacier calculated using the mass

flux model is 14.96 km^3 while the total volume for the Southern Alps region is 39.81 km^3. Other estimates of total ice volume for the Tasman Glacier give 14.77 km^3 (Anderton, 1973) and 15.62 km^3 (Chinn, 2001). The present estimate is not distinguishable as no uncertainties exist. However, this estimate is still considered an improvement over past estimates for the following reasons. First Chinn (2001) used area-volume scaling, an approach which is useful for large numbers of glaciers but tends to become unreliable for estimating individual glacier volumes. Furthermore, the method does not accommodate the ice-thickness distribution of a glacier. Given that Chinn (2001)'s ice volume estimate of 15.62 $km^3 \pm \sim 15\%$ is possibly an overestimation, .

Second, the ice volume estimate made by Anderton (1973) of 14.77 km^3 was obtained from a simplified contour map of bedrock elevation based on the interpolation between three profiles obtained from Broadbent (1973). Our results indicated that Broadbent's Ball Hut profile underestimated ice thickness based on his method of interpolating between the profiles using a simplified contour map. For these reasons our ice volume estimate is considered a more accurate representation of current glacier volume than previous estimates of ice volume. However, this claim cannot be fully resolved without associated uncertainties on our estimations.

3.6 Results summary

The ice-thickness distribution of the Tasman Glacier has been estimated using gravity observations and a suite of modelling techniques. Initially, synthetic models were presented to quantify the uncertainties in ice thickness due to physical parameters such as density and till thickness. A series of 2D models for the Tasman Glacier outlined the major features of the glacier and summarised the general ice-thickness distribution. 3D models were then used to compare results and explore features of the bed. Finally, our ice-thickness data were applied to a simple equilibrium mass flux model in order to estimate the ice-thickness distribution of

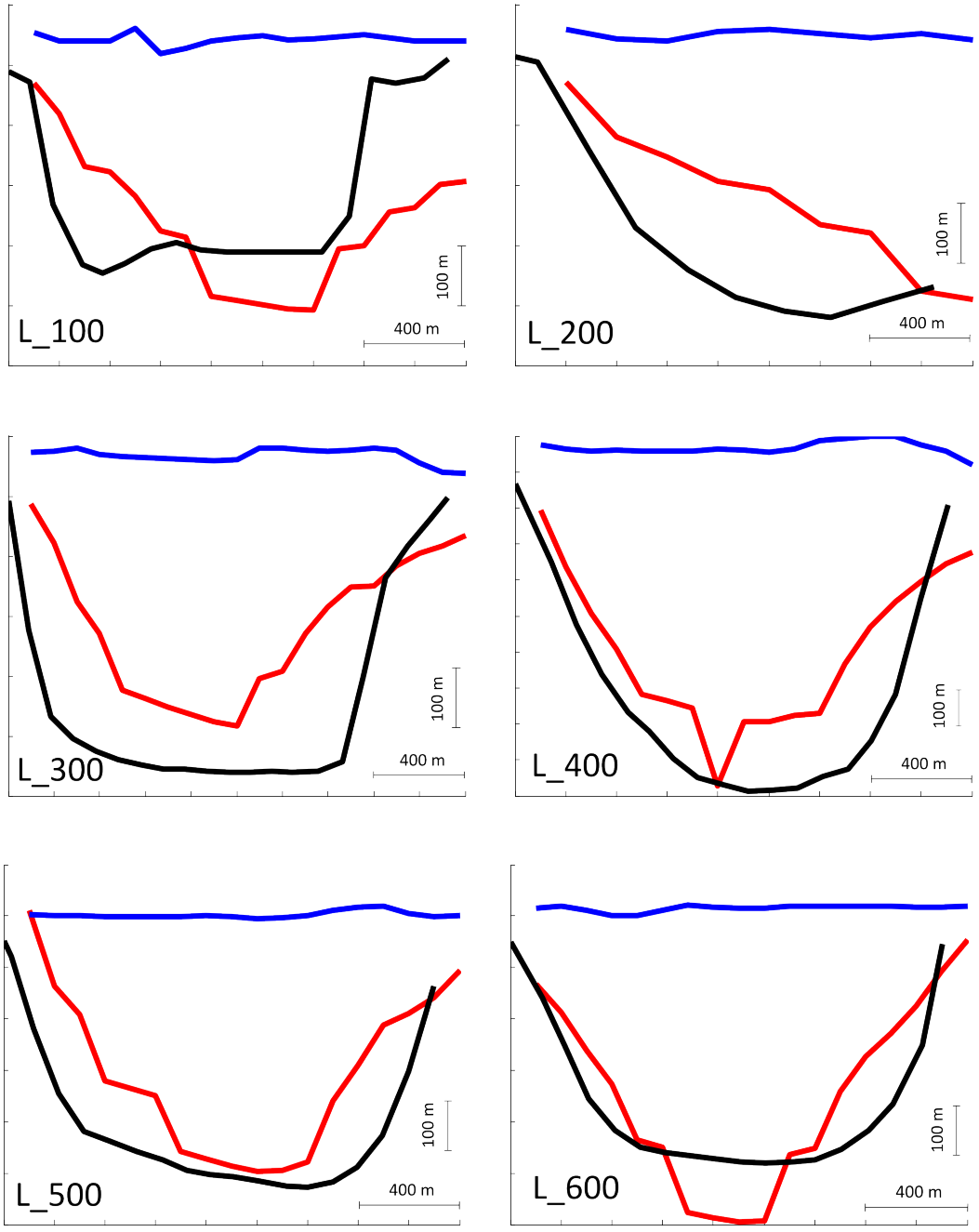

FIGURE 3.19: 2D transects for lines L_100 to L_600. Transects show modelled bed topography (red) versus 2D gravity results (black). Glacier surface marked by 1986 DEM (blue).

the entire Tasman Glacier. This led to an estimate of the Tasman glacier's total volume, however because an uncertainty could not be provided for this value,

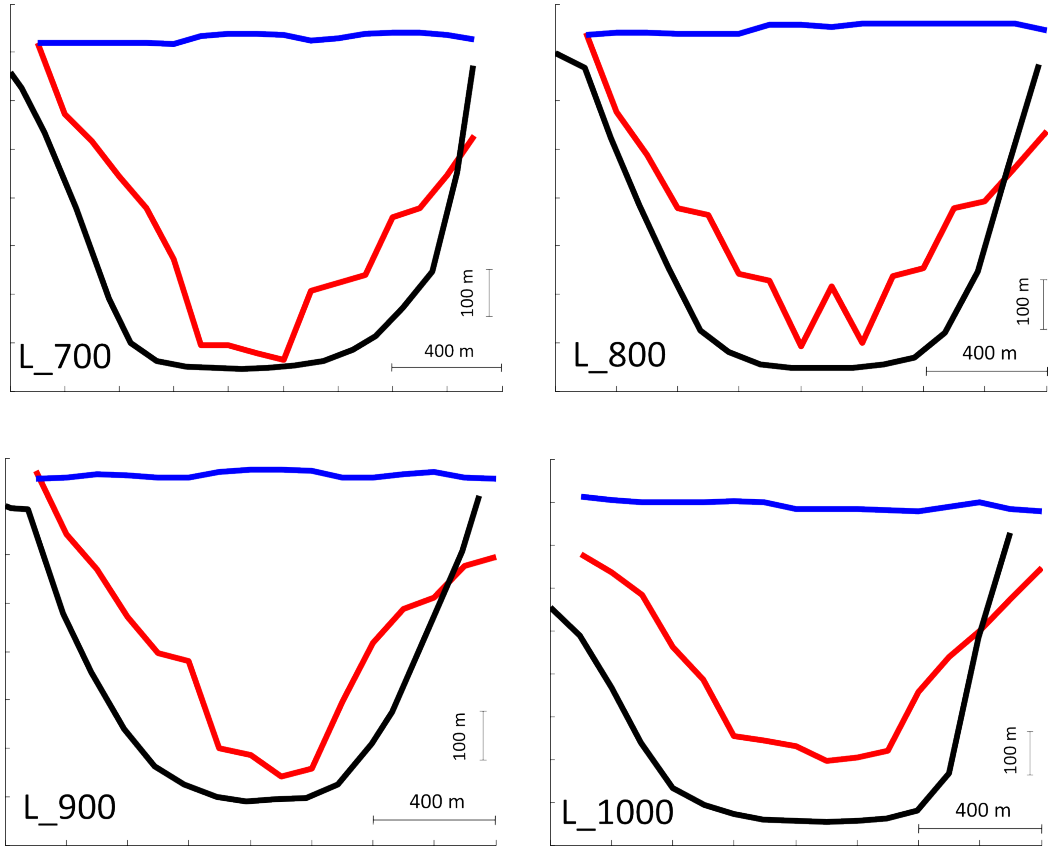

FIGURE 3.20: 2D transects for lines L_700 to L_1000. Transects show modelled bed topography (red) versus 2D gravity results (black). Glacier surface marked by 1986 DEM (blue).

comparisons with other studies are limited.

The next chapter summarises the ice-thickness distribution of the Tasman Glacier. Firstly, an analysis of the results section is presented through (1) anomalous features in the 2D profiles and (2) a comparison between 2D and 3D models. Secondly, I address the limitations in the methodology of this study and in the mass flux model. Finally, the possible implications of bed topography on future retreat are discussed before avenues for further research are mentioned.

Chapter 4

Discussion and conclusions

This study estimated the ice-thickness distribution of the lower Tasman Glacier through gravity models, constrained where possible with seismic refraction surveys and past studies. Here, I summarise the results of the 2D gravity profiles and compare these to the 3D gravity model results. I then highlight advantages and disadvantages of the gravity method before discussing limitations of the mass flux model used to estimate volume for the Tasman Glacier. The bed topography of the Tasman Glacier is then discussed with respect to potential controls on future retreat. Finally, I address the limitations of this study and suggest avenues for further research.

Glacier valley profiles

In most cases, 2D gravity models represented a U-shaped valley profile. This seemed like a sensible result, considering geomorphological (e.g. Montgomery (2002)) and mathematical evidence (e.g. Hirano and Aniya (1988)) which demonstrates the ubiquity of this valley shape in glaciated landscapes. I tested the applicability of using this valley shape in my gravity models by comparing one transect (L_900) to seismic results from Broadbent (1973) for the Ball Hut transect. The success of this test meant that I had some confidence in using the same valley profile shape

for adjacent profiles in order to develop a geologically reasonable model for the entire glacier.

Broadbent's seismic study resulted in a generally parabolic valley profile with a maximum ice thickness of 615 m (Figure 3.9). As Broadbent's seismic line was limited to the western half of the glacier, ice thickness in the eastern part of the valley may have been underestimated due to the incorrect identification of seismic events (Broadbent, 1973). Regardless, a maximum ice thickness of 663 m for L_900 is comparable to Broadbent's value of 615 m. The discrepancy between these values may be explained through two main sources of error. Firstly, ice-thickness errors are linked to reasonable uncertainties in density of ice/till and basement. The results from our synthetic models indicate that ice thickness can vary by up to 67 m for uncertainties in the density of ice, till or basement. Secondly, the thickness of till was shown to have a significant effect on the ice thickness variability (up to 50 m). Considering these two sources of error, the agreement between Broadbent's Ball Hut transect and L_900 is good.

For the Ball Hut transect and other transects, valley profiles included the sub-glacial till layer. The presence of till is suggested by Broadbent's estimate of sub-glacial till thickness near Ball Hut. Broadbent's plots indicate a maximum till thickness of $\sim$ 200 m. Our profiles adopt a till-thickness range at the bed of 100 to 200 m.

The following sections analyse the anomalous features present in some of the 2D models.

The residual 'ridge'

The residual 'ridge' is a longitudinally extensive feature seen between transects L_400 and L_600. It is composed of residual anomaly values that are high relative to neighbouring residual values and cannot be explained by errors alone. A high density body near the surface of the glacier was required to fit the anomaly. We suggested this is an entrained till body which most closely resembled the long-wavelength and high-amplitude ($\sim$ 6 mGal) signal of the residual ridge. In certain

areas the modelled till body is over 50 m thick and, for continuity, has been modelled across all lines that exhibit the ridge (see Appendix B). Other lines which exhibit local highs in the residual anomaly can also be modelled by inclusion of a localised till body emplaced near the surface. The cross-sectional areas of these till bodies range from 5×10^3 m^2 to 18×10^3 m^2 (summarised in Table 3.5). We suggest that the source for such an extensive body of till may be large rock avalanche events. For example, the Mount Cook rock avalanche in 1991 contained $11.8 \pm 2.4 \times 10^6$ m^3 of rock and ice (McSaveney, 2002) which is comparable to the total till volume (8.43×10^6 m^3) of our entrained till body.

Debris cover in general was excluded from the profile models due to the relatively insignificant effect it had on ice-thickness variability (summarised in section 3.3.3).

Murchison Embayment

The majority of the Murchison Embayment is occupied by a thin $\sim$ 100 m layer of ice which lies adjacent to the main body of the glacier. Additional evidence for this feature is provided by Redpath (2011) who agree that surface velocities in the embayment are very close to zero. Low surface velocities are interpreted to represent moraine and ice-cored moraine, thought to result from the detachment of ice from the main glacier. If this is indeed the case, the active trunk of the Tasman Glacier is approximately 1.4 km wide rather than 1.9 km at this location.

Comparing 2D/3D models

It was challenging to create a realistic 3D ice-thickness model for the Tasman Glacier because data was not collected on the moraine walls abutting the glacier. The structural inversion and forward gravity 3D models display ice and till layers extending to infinity in the $\pm$ x-direction instead of thinning to zero at the edges (Figure 4.1). Only the forward 3D model is valid for comparison with the 2D models as the structural inversion model diverged from the error bounds.

The forward 3D model used a 1986 DEM as the upper bound on ice-thickness values. Down-wasting of the glacier surface since 1986 has resulted in a uniform decrease of $\sim$ 48 m near Ball Hut. Maximum ice thicknesses in the forward 3D model is consistent with corresponding 2D profiles which used an updated glacier surface derived from GPS measurements. Taking the Ball Hut transect (L_900) as an example, the forward gravity 3D model indicate maximum ice thicknesses of 675 m while ice thickness for the initial 2D model was 672 m. It is thought that the 3D models may be underestimating the depth to the bed given the out-of-date DEM surface used. In the forward 3D model the bed is $\sim$ 10 m higher than L_900. Till thickness for the forward gravity model is 148 m while the initial 2D model yields a till thickness of 146 m. Generally, all models perform best when till thickness is kept relatively uniform (100–200 m) along the length of the glacier (Figure 4.2).

A feature in the forward 3D model which differs from the 2D models is the increase in till thickness towards the sides of the glacier (the opposite from what was proposed in section 3.3.3 for the synthetic models). Till thickening near the edges of the model may be due to the unconstrained ice thickness against the valley sides. The 3D model attempts to fit high residual anomaly values at the edges by increasing till thickness in these regions. This increased till thickness appears to reduce the overall density contrast but is likely to be an unrealistic feature of the models. This error highlights the need to constrain ice thickness at the edges of a glacier.

To summarise, maximum ice thicknesses are estimated well by the forward 3D model, although this result is partly because the input data for the 3D model was derived from 2D gravity models. The general distribution of ice is poorly constrained at the edges of the 3D model due to the lack of accessible sites adjacent to the glacier surface. The large discrepancy between the 2D and 3D models in these areas highlights the importance of constraining sites of zero ice thickness in gravity surveys.

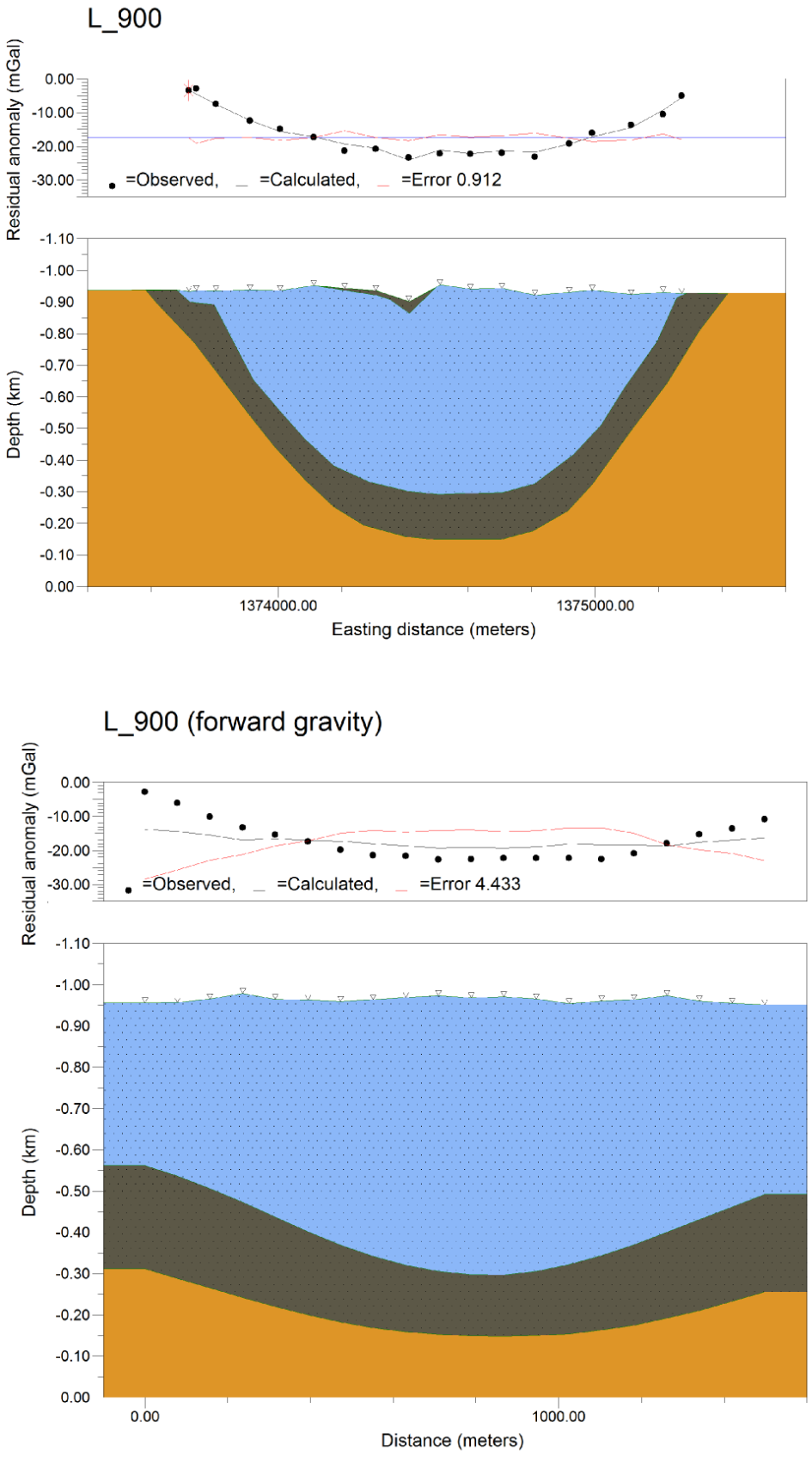

FIGURE 4.1: Comparison between 2D model and 3D forward gravity for L_900.

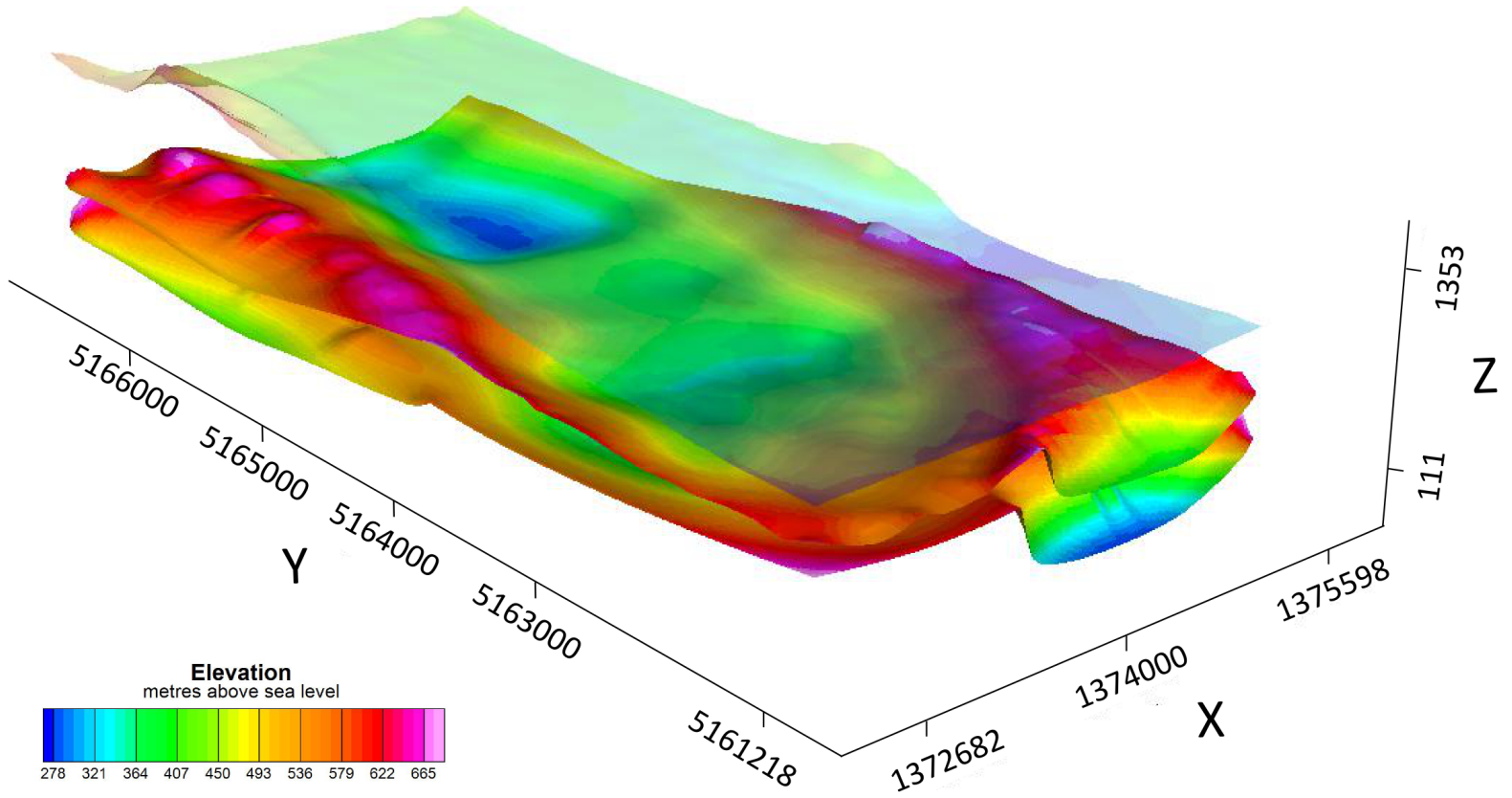

FIGURE 4.2: South-west oblique view of the structural inversion model for the lower Tasman Glacier. Three layers are seen in the model including the surface topography, ice-till interface, and till-basement interface (obscured). X and Y and Z axes are in metres (NZTM 2000).

4.1 Bed topography and future retreat

The driving stress and therefore the resisting shear stress at the sides and base of a glacier are proportional to its surface slope and ice thickness (Cuffey and Paterson, 2010). Ice thickness is bounded by the surface of the glacier and its underlying bed. Studies concerning the retreat of valley glaciers through proglacial lakes emphasize the importance of constraining bed topography (e.g. Boyce et al. (2007); Quincey and Glasser (2009)). Topographic highs in the bed are termed 'pinning points' due to their local modification of the stress balance (Mercer, 1961). It is on these pinning points that a glacier can become stabilised for extended periods of time (REF). Conversely, valley glaciers which gradually deepen up-valley are typically vulnerable to rapid retreat (Bassis and Jacobs, 2013). Thinning of the terminus region into bed over-deepenings has also been observed to induce flotation and up-warping of the terminus region (Boyce et al., 2007) leading to terminus break-up.

Thickness reductions such as those recently observed at Tasman Glacier cause a reduction in the driving stress, and therefore the velocity, assuming surface slope has remained constant through time. Our gravity surveys on the Tasman Glacier indicate that a gradual deepening of the bed occurs up-glacier from the terminus. Ice thicknesses range from 92 m at the terminus to 722 m adjacent to the Ball Glacier/Tasman Glacier confluence. Results at the terminus are less constrained due to the smaller number of gravity points occupying each transect. However, a sharp increase in ice thicknesses between the terminus profile T_100 (92 m) and L_100 (351 m) does suggest a reverse slope profile.

For the central gravity transects (L_400 to L_600) the bed topography is complicated with a localised high region at 400 to 450 m.a.s.l (equivalent to ice thicknesses of 460 to 510 m) surrounded by lower bed elevations of 250 to 320 m.a.s.l (500 to 690 m ice thickness). The high region extends 1 km along flow and across the entire width of the glacier (Figure 4.2). Forward gravity models could not fit lower bed elevations for this region. This feature may act as a future pinning point.

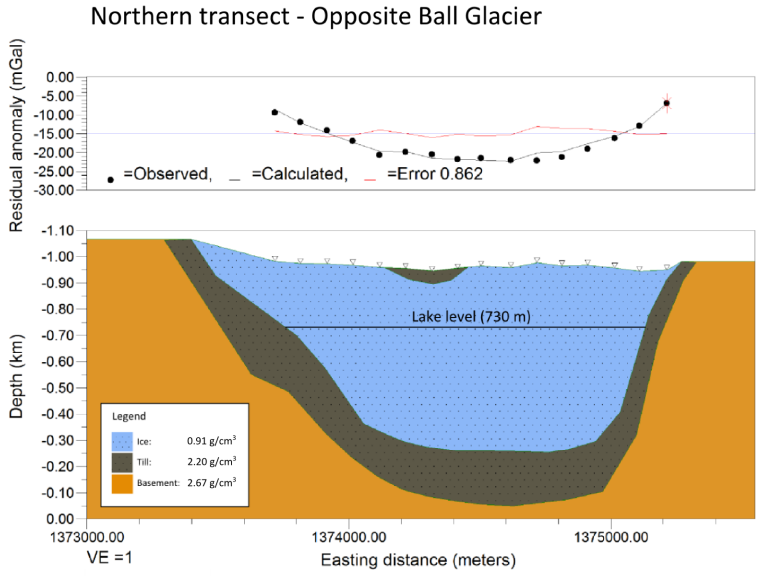

FIGURE 4.3: Forward gravity model for line 1000 on the Tasman Glacier (northern-most transect). The model shows the present-day lake level (730 m) against the glacier cross-section with a minimum bed elevation of 253 m.a.s.l.

The most negative residual gravity anomalies (down to -24 mGal) were observed at the northern transects, corresponding to a maximum ice thickness of 722 m. Ice thicknesses were observed to increase to the north, indicating that the bed deepens further up-valley from the northern-most transect. Observations of the surface velocity of the Tasman indicate that the Hochstetter Glacier provides the majority of ice to the lower glacier (Redpath, 2011). Gravity anomalies indicate a significant over-deepening south of the Hochstetter confluence (down to 253 m.a.s.l) which may be consistent with the high velocities observed here. Relative to the present-day lake level at the terminus (730 m) the bed is almost 500 m lower at the Ball/Tasman Glacier confluence (Figure 4.3).

Bed elevation is an important physical control on the future limits of lake expansion. For the Tasman Glacier, the maximum possible extent of the proglacial lake will be defined by the point where the base of the glacial valley exceeds the lake level (730 m). Bed topography at the Ball/Tasman Glacier confluence (253 m.a.s.l) is not high enough to terminate lake expansion. The maximum limit of

lake expansion lies somewhere north of the survey area and is only loosely constrained by Broadbent (1973) who measured bed elevations of $\sim$ 970 m.a.s.l, 16 km from the terminus.

Short-term limits on proglacial lake development are controlled by glacier velocity and melting and calving at the terminus (Quincey and Glasser, 2009). For the lake to continue migrating up-glacier, ice loss at the terminus would have to exceed the flux of the glacier to reach this point. Rates of cliff retreat by subaerial melt of 22 ma^{-1} and calving rates of 34 ma^{-1} for the terminus were calculated by Röhl (2006) between 2001 and 2003 while velocity measurements have been made by Quincey and Glasser (2009) and Redpath et al. (2013). An average retreat rate of 54 m/a between 2000 and 2006 and 144 m/a between 2007-2008 was obtained for the terminus of the Tasman Glacier by Dykes and Brook (2010). For the period 2009 to 2011, average surface velocities were less than 50 m/a at the terminus (Redpath et al., 2013). These results suggest that calving rates may still lead to significant retreat of the Tasman Glacier terminus in the future.

4.2 Limitations

First, I highlight the limitations in the geophysical methods used to estimate ice thickness. Second, I suggest possible reasons for the discrepancy between the modelled ice thickness (derived from the mass flux model) and measured ice thickness (from gravity results). A volume comparison is also made between the mass-flux model used here and the more rigorous mass-flux model by Huss and Farinotti (2012).

Estimating ice thickness

Obtaining ice thickness and volume estimates for debris-covered glaciers is difficult due to their unique surface morphology. For debris-covered glaciers like the Tasman, the gravity method is a sensible option as it relies on density contrast to measure ice thickness. Additionally, it is a relatively time efficient and environmentally considerate method to use compared to active-source seismics or ground-penetrating radar which can have logistical difficulties on debris cover (Schrott and Sass, 2008). Many previous ice-thickness studies on the Tasman Glacier have used the gravity method for these reasons (e.g. Broadbent (1973); Claridge (1983); Watson (1995)) although the non-uniqueness of plausible models does introduce errors into ice thickness and volume estimates. Prior to the formation of the proglacial lake in 1991 (Kirkbride and Warren, 1999), gravity transects obtained by Broadbent (1973) indicated maximum ice thicknesses near the former terminus of $\sim$ 200 m. Subsequent bathymetric soundings in the proglacial lake by Dykes and Brook (2010) indicated maximum water depths of $\sim$ 160–170 m for the same location. Although the glacier is likely to have thinned prior to lake formation and the present day lake level does not match the 1973 glacier surface on which Broadbent measured ice thickness, the agreements between past and present studies reflect the reliability of the gravity method for ice-thickness studies.

Bed characteristics can influence the dynamics of a glacier and therefore its responsiveness to climate forcings (Cuffey and Paterson, 2010). Our gravity models

could not uniquely identify the presence, or not, of a till layer, therefore seismic results from Broadbent (1973) led to the assumption of including a 100 to 200 m thick sub-glacial till layer. GPR transects by Nobes et al. (1994) show that the base of the ice and underlying till is adequately imaged, however Nobes et al.'s results were limited to the edges of the glacier where the ice was thin. For accurate estimations on till thickness, reflection seismics would provide the tightest constraints.

Performance of the mass flux model

In section 2.7 ice-thickness results were used to calibrate a mass flux model in order to estimate the ice-thickness distribution and volume of the entire Tasman Glacier. Results showed that for optimal parameter values, the model underestimated ice thickness relative to our measured ice-thickness values. Here, I discuss potential sources of error which may account for the discrepancies seen between the model output and measured ice thickness.

The DEM used for the mass flux model is derived from topographic maps which date back to 1986 (Columbus et al., 2011). On average, the surface has decreased in elevation by $\sim$ 48 m near Ball Hut. This provides some estimate of the amount of surface lowering that has occurred recently over the glacier. Use of an out-of-date DEM can lead to (1) an incorrect surface slope or (2) an overestimation of ice volume, considering it acts as an upper limit for ice thickness. Many debris covered glaciers in the Central Southern Alps exhibit low surface slopes which may be poorly represented by the DEM, and could pose difficulties for the estimation of mass flux. For this reason a median filter was applied to the DEM to smooth the slope. Improved performance on the mass flux model requires a more recent DEM along with some consideration of the thinning rate.

The method developed by Farinotti et al. (2009) calculates the ice volume flux based on the apparent mass balance for predefined ice flow-lines. In contrast, our mass flux model calculates mass flux through a series of elevation bands. For multiple glacier catchments which contribute to the overall mass flux of a glacier,

different tributaries may have different mass-balance relationships. For example, the western Hochstetter and eastern Darwin tributaries are likely to have different mass balance gradients, because the eastern side of the glacier is significantly drier than the western side. However, the lower Tasman Glacier should be well represented by a single mass balance relationship.

In the Tasman terminus region, the irregular and hummocky terrain is not well represented by the DEM. Poor representation of these features distorts the elevation bands and may lead to errors in the mass-flux calculation. Better estimation of the surface topography would result in an improved mass flux model and more reliable ice-thickness estimates.

The performance of our mass-flux model can also be compared to global studies (e.g. Huss and Farinotti (2012)) which estimated the total ice volume of all mountain glaciers and ice caps on Earth. However, because both our estimate and Huss and Farinotti's estimate were not supported with an associated uncertainty, no robust conclusions can be drawn. Huss and Farinotti (2012) obtained a total ice volume of 35.98 km^3 for the Central Southern Alps region, albeit with a slightly different area domain, using the complete method developed by Farinotti et al. (2009) (Figure 4.4). This result is lower than our estimate of 39.81 km^3 which may be due to different area domain being used (Figure 4.5). The aforementioned simplifications made in our mass-flux model may also reflect the discrepancy between these models. As the complete method developed by Farinotti et al. (2009) uses glacier flow-lines to compute ice volume, the performance of Huss and Farinotti's model is likely improved for estimating ice thickness in the upper regions glacier catchments. However, as this study incorporated gravity-derived ice-thickness measurements for the lower Tasman Glacier, the estimate made by our mass-flux model may be more accurate for the lower Tasman glacier. This comparison highlights the advantages of including uncertainties for ice volume estimates, using an appropriate mass-flux model and also incorporating direct ice-thickness measurements to improve the performance of these models.

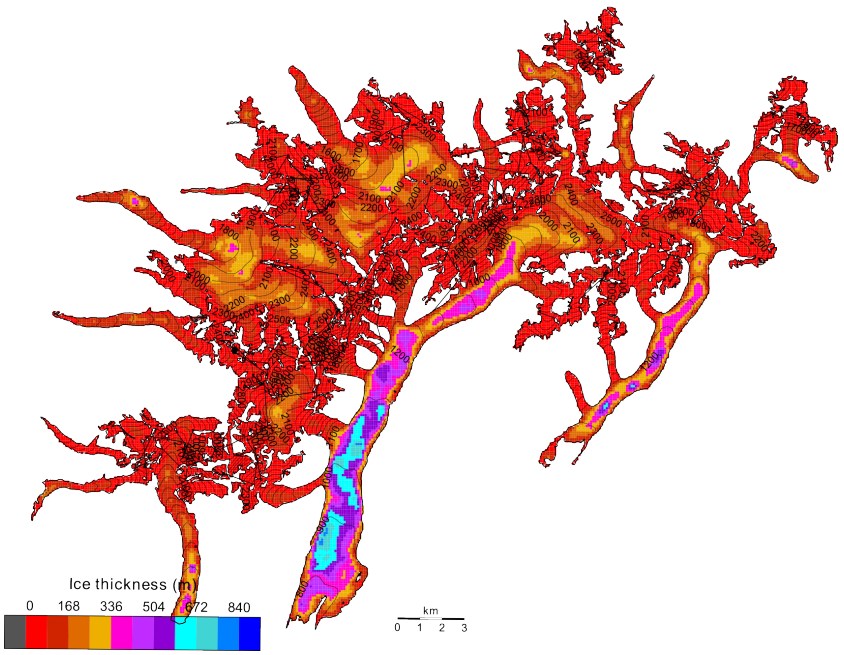

FIGURE 4.4: Map of the Central Southern Alps model domain showing ice thickness derived from the mass flux model developed by Huss and Farinotti (2012).

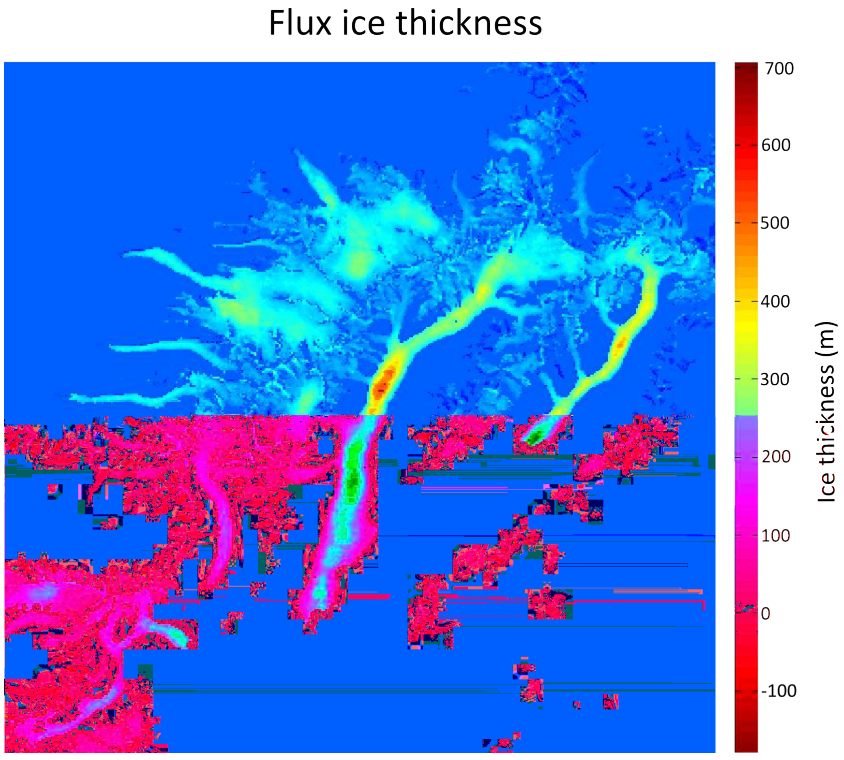

FIGURE 4.5: Map of the Central Southern Alps model domain showing ice thickness derived from the mass flux model using gravity derived ice-thickness measurements.

Interestingly, the volume estimate was systematically lower for large glaciers compared to volume-area scaling (-49% for New Zealand) (Huss and Farinotti, 2012). This underestimation was also noted in Chapter 3 between our volume estimate 14.96 km^3 and the volume estimate made by Chinn (2001) of 15.62 km^3. To accurately constrain the ice-thickness distribution of glaciers worldwide, glacio-dynamic models are favoured, but require more ice-thickness data to constrain their uncertainties Huss and Farinotti (2012).

A simple ice flux model is used here to infer the ice-thickness distribution and volume of the Tasman Glacier. Ideally bed topography should be used to constrain the model through the calibration of parameters such as A and C. Including higher quality surface elevation data and using model flow-lines would result in further improvement. Ice flux models such as the one used in this study have the potential to provide more robust estimates of glacier volume for the Southern Alps.

4.3 Future work

Ice-thickness measurements for the Tasman Glacier were made for an area extending from the terminus region to Ball Glacier. To constrain ice thickness for a larger section of the Tasman Glacier, another similarly sized gravity survey could be conducted up-glacier from the northern-most transect presented here. This would allow a better estimate of ice volume for the Tasman Glacier and would provide further data for calibrating models used to calculate the total volume of the world's glaciers (e.g. Huss and Farinotti (2012)).

An improved bed dataset for Tasman Glacier will also be useful for dynamic glacier modelling studies, aimed at explicitly calculating the future response of this glacier to climate change (Oerlemans et al., 1998). Such studies will allow tighter constraints on local ice thickness to be resolved. The implementation of gravity tie sites to the edge of the Tasman Glacier allows errors in the residual anomaly and therefore ice thickness to be reduced for this purpose. Local scale ice volume models will also enable improved predictions of melt-water run-off which forms an

important part of the hydrological cycle (Huss et al., 2008) and is directly used in NZ electricity generation and agriculture. Local studies such as this also provide tighter constraints on global ice volume studies (e.g. Radić and Hock (2010)) that assess the impact of climate change on global sea level.

4.4 Conclusions

A large-scale gravity survey has been used here to explore the ice-thickness distribution of the lower Tasman Glacier. The results from this gravity survey were also applied to a mass flux model to assess the performance of the model and provide an estimate of total ice volume for the Tasman Glacier. The questions outlined in section 1.5 can now be addressed:

Question 1: What is the ice-thickness distribution on the lower part of Tasman Glacier?

Gravity models generally indicate a U-shaped valley for the lower Tasman Glacier with ice thicknesses of 722 m near Ball Glacier, gradually thinning to 92 m at the terminus. A prominent reverse bed-slope is also seen between L_300 and T_100 where a reduction in ice thickness occurs. These results are supported by previous geophysical studies (e.g. Broadbent (1973); Watson (1995)) who used similar methods (reflection seismics and gravity) to calculate ice thickness.

Question 2: How do my ice-thickness measurements for the Tasman Glacier compare to estimates made using a simple mass flux model?

Using gravity derived ice-thickness results as input data to a mass flux model, ice-thickness outputs from the mass flux model were compared to the 2D gravity profiles. Generally, ice thickness was underestimated relative to the gravity derived ice-thickness results. Overall, the RMSE between the mass flux model results and the gravity derived results was 148 m. Improvements to this discrepancy can be made by constraining ice thickness for a larger area of the glacier and providing a more recent DEM to the mass flux model (Anderson, 2013).

Final ice volume was also calculated using the mass flux model. For the Tasman Glacier the best estimate was 14.96 km^3. This is thought to be a reliable estimate of ice volume compared to Chinn (2001) who estimated 15.62 km^3 based on volume-area scaling methods, and Anderton (1973) who estimated 14.77 km^3 based on interpolation between 2D profiles made by Broadbent (1973). However, no robust conclusions can be drawn from these values without appropriate uncertainties.

To conclude, ice-thickness measurements are required to calculate the geometry and driving stress of a glacier as well as providing estimates to the total volume of glacier ice on Earth. As measurements are difficult to make everywhere, models are typically used to infer this ice volume. Studies like this highlight the importance of providing direct ice-thickness measurements to improve glacio-dynamic models and global ice volume estimates.

Appendix A

Gravity Data

Station (ID)	Latitude (WGS84)	Longitude (WGS84)	Easting (NZTM)	Northing (NZTM)	Height (m)	TC (mGal)	g abs (mGal)	g boug (mGal)	g anom (mGal)	g res (mGal)	Error (mGal)
T 101	-43.6625	170.1902	1373452	5161779	752.149	20.50	980257.24	980335.27	-78.03	-13.82	1.18
T 102	-43.6624	170.1892	1373368	5161785	752.551	18.70	980257.2	980335	-77.8	-13.63	1.18
T 103	-43.6621	170.188	1373271	5161818	742.937	18.20	980258.97	980336.35	-77.38	-13.28	1.18
T 104	-43.6616	170.1868	1373170	5161863	755.026	17.50	980256.57	980333.42	-76.85	-12.84	1.18
T 105	-43.661	170.1852	1373039	5161932	742.197	17.10	980259.93	980334.75	-74.82	-10.93	1.18
T 201	-43.6586	170.184	1372931	5162193	753.431	16.10	980259.39	980329.82	-70.43	-6.84	1.18
T 202	-43.659	170.1848	1372997	5162150	755	15.80	980256.82	980331.4	-74.58	-10.92	1.18
T 203	-43.6594	170.1859	1373091	5162106	773.664	15.40	980252.62	980328.25	-75.63	-11.89	1.18
T 204	-43.6598	170.1871	1373192	5162069	742.147	15.50	980258.88	980335.21	-76.33	-12.51	1.18
T 205	-43.66	170.1882	1373279	5162044	740.065	15.70	980258.73	980335.97	-77.24	-13.35	1.18
T 206	-43.6604	170.1894	1373379	5162006	755.406	15.90	980255.88	980334.02	-78.14	-14.18	1.18
T 207	-43.6612	170.1931	1373682	5161924	767	16.40	980257.1	980332.06	-74.96	-10.8	1.18
T 208	-43.6611	170.1917	1373567	5161938	765.579	16.90	980254.28	980332.75	-78.47	-14.37	1.18
T 209	-43.6606	170.1906	1373475	5161986	764.413	18.00	980254.16	980332.85	-78.69	-14.67	1.18
101	-43.6518	170.1855	1373028	5162954	789.385	22.20	980253.93	980320.46	-66.53	-3.65	1.18

Continued on next page

Table A.1 Continued from previous page

Station (ID)	Latitude (WGS84)	Longitude (WGS84)	Easting (NZTM)	Northing (NZTM)	Height (m)	TC (mGal)	g abs (mGal)	g boug (mGal)	g anom (mGal)	g res (mGal)	Error (mGal)
102	-43.6521	170.1866	1373116	5162920	783.251	20.20	980252.86	980323.68	-70.82	-7.87	1.18
103	-43.6523	170.1877	1373210	5162898	773	19.30	980250.07	980326.63	-76.56	-13.54	1.18
104	-43.6524	170.1891	1373323	5162893	795.785	17.40	980245.42	980324.06	-78.65	-15.57	1.18
105	-43.6528	170.1901	1373402	5162851	801.663	16.50	980244.67	980323.86	-79.19	-16.04	1.18
106	-43.653	170.1911	1373488	5162834	784	16.70	980244.75	980327.1	-82.35	-19.15	1.18
107	-43.6533	170.1924	1373591	5162805	772	16.20	980248.36	980330.01	-81.65	-18.37	1.18
108	-43.6535	170.1936	1373691	5162784	772.256	16.00	980249.96	980330.2	-80.24	-16.9	1.18
109	-43.6538	170.1948	1373789	5162755	791.528	15.70	980246.16	980326.68	-80.52	-17.11	1.18
110	-43.654	170.1961	1373890	5162732	807.058	14.50	980243.21	980324.85	-81.64	-18.17	1.18
111	-43.6542	170.1971	1373975	5162718	782.624	14.70	980248.66	980329.47	-80.82	-17.3	1.18
112	-43.6544	170.1983	1374073	5162692	800.461	14.00	980246.38	980326.76	-80.38	-16.8	1.18
113	-43.6547	170.1994	1374162	5162666	812.827	13.90	980244.22	980324.38	-80.16	-16.52	1.18
114	-43.6549	170.2007	1374265	5162651	809.378	13.60	980246.53	980325.38	-78.85	-15.15	1.18
115	-43.6551	170.202	1374376	5162627	803.029	13.80	980250.45	980326.5	-76.05	-12.29	1.18
116	-43.6555	170.203	1374455	5162585	798.599	14.00	980255.49	980327.21	-71.73	-7.9	1.18

Continued on next page

Table A.1 Continued from previous page

Station (ID)	Latitude (WGS84)	Longitude (WGS84)	Easting (NZTM)	Northing (NZTM)	Height (m)	TC (mGal)	g abs (mGal)	g boug (mGal)	g anom (mGal)	g res (mGal)	Error (mGal)
117	-43.6557	170.2042	1374556	5162569	809.328	13.80	980255.16	980325.31	-70.15	-6.27	1.18
118	-43.6559	170.2056	1374670	5162552	782.116	14.60	980263.17	980329.89	-66.72	-2.78	1.18
119	-43.6561	170.2068	1374760	5162534	815.22	14.10	980259.68	980323.86	-64.18	-0.19	1.18
201	-43.6477	170.1869	1373130	5163405	806.852	22.30	980249.5	980316.6	-67.1	-4.63	1.18
202	-43.6478	170.1882	1373235	5163400	791.331	21.90	980245.08	980320.06	-74.98	-12.46	1.18
203	-43.6481	170.1893	1373325	5163366	803.863	19.30	980242.14	980320.22	-78.08	-15.48	1.18
204	-43.6484	170.1906	1373428	5163343	815.427	18.50	980244.8	980318.68	-73.88	-11.22	1.18
205	-43.6485	170.1918	1373522	5163336	808.495	16.90	980239.32	980321.71	-82.39	-19.67	1.18
206	-43.6488	170.1929	1373619	5163307	823.777	16.40	980241.84	980319.26	-77.42	-14.63	1.18
207	-43.6489	170.194	1373704	5163291	799.738	16.00	980241.24	980324.37	-83.13	-20.29	1.18
208	-43.6493	170.1953	1373810	5163251	819.012	17.00	980242.59	980319.59	-77	-14.07	1.18
209	-43.6495	170.1966	1373913	5163240	816.734	16.10	980245.48	980321	-75.52	-12.54	1.18
210	-43.6497	170.1977	1374007	5163219	808.537	14.60	980242.45	980324.06	-81.61	-18.57	1.18
301	-43.6433	170.1887	1373253	5163902	800.669	23.70	980248.77	980315.94	-67.17	-5.15	1.18
302	-43.6435	170.1898	1373346	5163882	803.61	21.10	980244.11	980318.03	-73.92	-11.84	1.18

Continued on next page

Table A.1 Continued from previous page

Station (ID)	Latitude (WGS84)	Longitude (WGS84)	Easting (NZTM)	Northing (NZTM)	Height (m)	TC (mGal)	g abs (mGal)	g boug (mGal)	g anom (mGal)	g res (mGal)	Error (mGal)
303	-43.6437	170.191	1373445	5163862	805.221	19.50	980241.54	980319.31	-77.77	-15.62	1.18
304	-43.644	170.1922	1373539	5163836	809.989	18.20	980241.63	980319.74	-78.11	-15.89	1.18
305	-43.6442	170.1934	1373640	5163816	823.302	16.90	980235.06	980318.43	-83.37	-21.09	1.18
306	-43.6444	170.1946	1373736	5163797	827.278	16.00	980236.14	980318.52	-82.38	-20.04	1.18
307	-43.6447	170.1958	1373834	5163772	835.119	15.70	980239.4	980317.3	-77.9	-15.49	1.18
308	-43.6449	170.197	1373933	5163749	822.861	15.90	980239.28	980319.59	-80.31	-17.83	1.18
309	-43.6451	170.1982	1374029	5163724	831.317	16.40	980239.43	980317.39	-77.96	-15.42	1.18
310	-43.6453	170.1994	1374125	5163712	843.203	15.50	980237.37	980315.98	-78.61	-16.01	1.18
311	-43.6456	170.2006	1374221	5163683	840.867	14.10	980234.74	980317.88	-83.14	-20.48	1.18
312	-43.6459	170.2017	1374312	5163652	831.062	14.60	980234.74	980319.36	-84.62	-21.89	1.18
313	-43.6461	170.2028	1374407	5163634	815.613	14.60	980239.21	980322.37	-83.16	-20.38	1.18
314	-43.6461	170.2039	1374492	5163632	816.391	14.30	980240.11	980322.51	-82.4	-19.57	1.18
315	-43.6465	170.2053	1374610	5163589	826	14.10	980239.74	980320.92	-81.18	-18.27	1.18
316	-43.6467	170.2067	1374718	5163577	814	14.80	980242.69	980322.51	-79.82	-16.86	1.18
317	-43.647	170.2078	1374809	5163546	820	14.10	980245.16	980322.1	-76.94	-13.91	1.18

Continued on next page

Table A.1 Continued from previous page

Station (ID)	Latitude (WGS84)	Longitude (WGS84)	Easting (NZTM)	Northing (NZTM)	Height (m)	TC (mGal)	g abs (mGal)	g boug (mGal)	g anom (mGal)	g res (mGal)	Error (mGal)
318	-43.6472	170.209	1374907	5163521	804	15.00	980250.04	980324.36	-74.32	-11.23	1.18
319	-43.6475	170.2102	1375002	5163499	801	15.20	980252.96	980324.81	-71.85	-8.71	1.18
320	-43.6477	170.2114	1375100	5163472	793	15.70	980256.28	980325.88	-69.6	-6.4	1.18
321	-43.6479	170.2123	1375178	5163457	807.593	16.20	980259.29	980322.54	-63.25	0	1.18
401	-43.6389	170.1898	1373329	5164390	835.227	23.80	980243.66	980308.68	-65.02	-3.47	1.18
402	-43.6392	170.1916	1373471	5164366	841.794	20.80	980238.16	980310.4	-72.24	-10.6	1.18
403	-43.6395	170.1928	1373573	5164340	847.902	19.50	980234.95	980310.57	-75.62	-13.9	1.18
404	-43.6397	170.194	1373669	5164314	823.408	18.80	980238.41	980316.03	-77.62	-15.84	1.18
405	-43.6399	170.1953	1373775	5164303	844.173	18.00	980234.39	980312.75	-78.36	-16.52	1.18
406	-43.6401	170.1963	1373858	5164275	841.982	16.90	980233.95	980314.33	-80.38	-18.47	1.18
407	-43.6403	170.1975	1373951	5164256	831.389	16.80	980235.75	980316.55	-80.8	-18.83	1.18
408	-43.6406	170.1987	1374053	5164231	845.316	16.00	980232.82	980314.67	-81.85	-19.8	1.18
409	-43.6408	170.1999	1374150	5164211	855.23	15.10	980230.75	980313.63	-82.88	-20.78	1.18
410	-43.641	170.2011	1374245	5164189	869.289	14.60	980227.74	980311.35	-83.61	-21.44	1.18
411	-43.6412	170.2023	1374342	5164170	876.259	14.80	980226.57	980309.79	-83.22	-21	1.18

Continued on next page

Table A.1 Continued from previous page

Station (ID)	Latitude (WGS84)	Longitude (WGS84)	Easting (NZTM)	Northing (NZTM)	Height (m)	TC (mGal)	g abs (mGal)	g boug (mGal)	g anom (mGal)	g res (mGal)	Error (mGal)
412	-43.6415	170.2035	1374442	5164146	836.939	15.00	980235.49	980317.36	-81.87	-19.58	1.18
413	-43.6417	170.2047	1374541	5164119	855.398	14.50	980232.42	980314.29	-81.87	-19.51	1.18
414	-43.6419	170.2059	1374640	5164101	830	14.60	980236.57	980319.19	-82.62	-20.2	1.18
415	-43.6422	170.207	1374729	5164080	867.947	14.50	980232.37	980311.87	-79.5	-17.03	1.18
416	-43.6423	170.2082	1374829	5164067	848.331	14.30	980237.66	980315.93	-78.27	-15.75	1.18
417	-43.6426	170.2095	1374928	5164033	840.81	15.00	980241.63	980316.71	-75.08	-12.48	1.18
418	-43.6429	170.2108	1375035	5164011	837.248	16.10	980245.96	980316.31	-70.35	-7.7	1.18
501	-43.6344	170.1916	1373459	5164897	855.321	24.20	980239.5	980303.87	-64.37	-3.29	1.18
502	-43.6346	170.192	1373490	5164873	853.446	23.10	980238.53	980305.38	-66.86	-5.73	1.18
503	-43.6349	170.1931	1373578	5164844	850.018	21.30	980236.34	980307.94	-71.6	-10.4	1.18
504	-43.6352	170.1943	1373676	5164813	858.767	19.80	980233.07	980307.68	-74.61	-13.34	1.18
505	-43.6354	170.1955	1373776	5164803	861.233	18.60	980230.9	980308.44	-77.54	-16.21	1.18
506	-43.6356	170.1968	1373881	5164779	847.806	17.70	980233.02	980312.03	-79.01	-17.61	1.18
507	-43.6359	170.1981	1373985	5164750	855.161	16.90	980232.15	980311.4	-79.25	-17.77	1.18
508	-43.6357	170.1993	1374086	5164774	852.047	16.50	980231.45	980312.41	-80.96	-19.46	1.18

Continued on next page

Table A.1 Continued from previous page

Station (ID)	Latitude (WGS84)	Longitude (WGS84)	Easting (NZTM)	Northing (NZTM)	Height (m)	TC (mGal)	g abs (mGal)	g boug (mGal)	g anom (mGal)	g res (mGal)	Error (mGal)
509	-43.6364	170.2005	1374180	5164706	857.24	15.90	980230.11	980311.99	-81.88	-20.27	1.18
510	-43.6365	170.2016	1374269	5164696	864.285	15.40	980228.34	980311.18	-82.84	-21.19	1.18
511	-43.6366	170.2028	1374369	5164681	862.071	15.10	980229.1	980311.9	-82.8	-21.09	1.18
512	-43.6369	170.2039	1374462	5164650	858.365	15.00	980229.74	980312.76	-83.02	-21.23	1.18
513	-43.6373	170.2053	1374576	5164612	856.486	14.90	980231.31	980313.23	-81.92	-20.05	1.18
514	-43.6373	170.2064	1374657	5164619	876.236	14.50	980227.33	980309.75	-82.42	-20.52	1.18
515	-43.6376	170.2076	1374756	5164586	877.261	14.40	980227.76	980309.68	-81.92	-19.95	1.18
516	-43.6377	170.2087	1374852	5164575	875.668	15.00	980230.08	980309.45	-79.37	-17.35	1.18
517	-43.6381	170.21	1374953	5164540	861.195	15.20	980234.9	980312.1	-77.2	-15.11	1.18
518	-43.6382	170.2113	1375059	5164536	847.335	16.30	980238.45	980313.74	-75.29	-13.15	1.18
519	-43.6385	170.2125	1375154	5164499	869.62	16.70	980238.35	980308.92	-70.57	-8.36	1.18
601	-43.6314	170.1933	1373581	5165234	865.623	23.50	980236.13	980302.36	-66.23	-5.45	1.18
602	-43.6316	170.1948	1373705	5165223	876.114	20.50	980230.9	980303.22	-72.32	-11.47	1.18
603	-43.6316	170.1959	1373795	5165219	867.389	19.60	980231.08	980305.9	-74.82	-13.92	1.18
604	-43.6318	170.1971	1373892	5165207	884.575	18.30	980226.41	980303.83	-77.42	-16.47	1.18

Continued on next page

Table A.1 Continued from previous page

Station (ID)	Latitude (WGS84)	Longitude (WGS84)	Easting (NZTM)	Northing (NZTM)	Height (m)	TC (mGal)	g abs (mGal)	g boug (mGal)	g anom (mGal)	g res (mGal)	Error (mGal)
605	-43.6319	170.1984	1373995	5165193	892.09	17.20	980223.9	980303.44	-79.54	-18.52	1.18
606	-43.6319	170.1996	1374090	5165195	873.116	17.10	980227.17	980307.26	-80.09	-19.03	1.18
607	-43.6321	170.2008	1374189	5165182	893.182	16.40	980222.47	980304.06	-81.59	-20.48	1.18
608	-43.6322	170.202	1374288	5165172	887.643	16.00	980223.17	980305.52	-82.35	-21.17	1.18
609	-43.6323	170.2032	1374388	5165166	871.484	16.00	980226.33	980308.71	-82.38	-21.16	1.18
610	-43.6324	170.2045	1374492	5165162	882.515	15.60	980224.07	980306.94	-82.87	-21.6	1.18
611	-43.6325	170.2057	1374588	5165149	882.13	15.70	980224.39	980307.01	-82.62	-21.3	1.18
612	-43.6327	170.207	1374692	5165132	868.998	15.80	980227.41	980309.48	-82.07	-20.68	1.18
613	-43.6328	170.2081	1374781	5165117	872.723	15.80	980226.91	980308.7	-81.79	-20.36	1.18
614	-43.6329	170.2094	1374887	5165117	893.494	15.60	980223.74	980304.87	-81.13	-19.65	1.18
615	-43.6329	170.2107	1374995	5165114	889.375	15.90	980225.78	980305.34	-79.56	-18.03	1.18
616	-43.633	170.2119	1375090	5165105	890.551	16.40	980227.45	980304.69	-77.24	-15.67	1.18
617	-43.6331	170.2134	1375206	5165107	882.018	17.70	980231.71	980305.01	-73.3	-11.69	1.18
618	-43.6333	170.2143	1375283	5165088	872	18.80	980234.79	980305.97	-71.18	-9.52	1.18
701	-43.628	170.1943	1373652	5165616	860	24.20	980236.13	980302.37	-66.24	-5.83	1.18

Continued on next page

Table A.1 Continued from previous page

Station (ID)	Latitude (WGS84)	Longitude (WGS84)	Easting (NZTM)	Northing (NZTM)	Height (m)	TC (mGal)	g abs (mGal)	g boug (mGal)	g anom (mGal)	g res (mGal)	Error (mGal)
702	-43.6274	170.1949	1373697	5165684	865	23.40	980232.7	980302.16	-69.46	-9.11	1.18
703	-43.6274	170.1962	1373797	5165687	891	20.30	980226.41	980300.15	-73.74	-13.34	1.18
704	-43.6273	170.1974	1373899	5165708	901.113	18.80	980227.69	980299.62	-71.93	-11.5	1.18
705	-43.6276	170.1988	1374014	5165677	909.523	18.10	980221.27	980298.74	-77.47	-16.95	1.18
706	-43.6275	170.1999	1374096	5165692	904	17.40	980219.13	980300.53	-81.4	-20.87	1.18
707	-43.6275	170.201	1374188	5165687	891	17.20	980220.63	980303.23	-82.6	-22.02	1.18
708	-43.6275	170.2024	1374298	5165694	891	16.90	980218.59	980303.61	-85.02	-24.39	1.18
709	-43.6276	170.2036	1374402	5165687	923.545	15.80	980215.98	980298.33	-82.35	-21.67	1.18
710	-43.6278	170.2048	1374498	5165669	916.486	15.70	980217.76	980299.79	-82.03	-21.29	1.18
711	-43.6279	170.206	1374595	5165662	911.238	15.90	980217.86	980300.67	-82.81	-22.02	1.18
712	-43.628	170.2072	1374689	5165655	902.309	16.00	980220.75	980302.28	-81.53	-20.69	1.18
713	-43.628	170.2085	1374797	5165651	881	17.20	980221.32	980305.29	-83.97	-23.08	1.18
714	-43.6281	170.2099	1374906	5165646	888.151	17.00	980224.24	980304.12	-79.88	-18.94	1.18
715	-43.6282	170.2109	1374990	5165636	884	17.30	980222.93	980304.57	-81.64	-20.65	1.18
716	-43.6283	170.2121	1375090	5165634	898	17.30	980221.33	980301.91	-80.58	-19.55	1.18

Continued on next page

Table A.1 Continued from previous page

Station (ID)	Latitude (WGS84)	Longitude (WGS84)	Easting (NZTM)	Northing (NZTM)	Height (m)	TC (mGal)	g abs (mGal)	g boug (mGal)	g anom (mGal)	g res (mGal)	Error (mGal)
717	-43.6284	170.2134	1375196	5165623	897	18.00	980224.46	980301.33	-76.87	-15.79	1.18
718	-43.6286	170.2146	1375292	5165605	893	19.60	980227.44	980300.54	-73.1	-11.96	1.18
719	-43.6282	170.2153	1375345	5165655	877	21.50	980232.18	980301.78	-69.6	-8.49	1.18
801	-43.6236	170.1955	1373731	5166113	899.389	23.60	980232.14	980294.9	-62.76	-2.86	1.18
802	-43.6235	170.1968	1373831	5166119	903.431	21.30	980228.09	980296.39	-68.3	-8.35	1.18
803	-43.6235	170.1978	1373913	5166129	917.704	19.80	980223.01	980295.1	-72.09	-12.12	1.18
804	-43.6235	170.1989	1374006	5166129	896	19.40	980223.32	980299.7	-76.38	-16.35	1.18
805	-43.6235	170.2001	1374099	5166133	884	18.90	980223.12	980302.6	-79.48	-19.41	1.18
806	-43.6235	170.2013	1374201	5166139	905	17.60	980218.47	980299.74	-81.27	-21.17	1.18
807	-43.6235	170.2026	1374302	5166141	912	17.10	980215.72	980298.9	-83.18	-23.03	1.18
808	-43.6234	170.2038	1374397	5166151	904	17.10	980217.3	980300.42	-83.12	-22.94	1.17
809	-43.6234	170.2051	1374504	5166159	918.697	16.80	980215.82	980297.88	-82.06	-21.84	1.18
810	-43.6234	170.2063	1374602	5166165	917	16.90	980213.93	980298.1	-84.17	-23.91	1.18
811	-43.6234	170.2075	1374700	5166168	937	16.20	980211.71	980294.86	-83.15	-22.86	1.18
812	-43.6234	170.2088	1374802	5166172	934	16.60	980212.05	980295	-82.95	-22.61	1.18

Continued on next page

Table A.1 Continued from previous page

Station (ID)	Latitude (WGS84)	Longitude (WGS84)	Easting (NZTM)	Northing (NZTM)	Height (m)	TC (mGal)	g abs (mGal)	g boug (mGal)	g anom (mGal)	g res (mGal)	Error (mGal)
813	-43.6233	170.21	1374902	5166179	908	17.40	980215.99	980299.34	-83.36	-22.98	1.18
814	-43.6233	170.2112	1374999	5166186	893	18.20	980220.39	980301.48	-81.09	-20.68	1.18
815	-43.6233	170.2126	1375106	5166190	903	18.80	980219.99	980298.91	-78.92	-18.48	1.18
816	-43.6232	170.2137	1375201	5166199	908	19.80	980221.78	980296.95	-75.17	-14.69	1.18
817	-43.6232	170.2151	1375310	5166208	889	22.30	980229.06	980298.21	-69.15	-8.64	1.18
901	-43.6192	170.1956	1373719	5166600	934	24.30	980224.62	980287	-62.38	-3.01	1.18
902	-43.6192	170.1959	1373743	5166605	935.79	23.30	980225.79	980287.61	-61.82	-2.45	1.18
903	-43.619	170.1966	1373805	5166619	934.769	22.40	980222.28	980288.7	-66.42	-7.03	1.18
904	-43.619	170.198	1373913	5166626	938.708	20.50	980218.38	980289.83	-71.46	-12.02	1.18
905	-43.619	170.1991	1374007	5166631	936.746	19.50	980217.25	980291.17	-73.92	-14.44	1.18
906	-43.6189	170.2005	1374114	5166650	952.129	18.40	980212.79	980289.22	-76.43	-16.92	1.18
907	-43.6189	170.2017	1374211	5166646	943	18.30	980210.71	980291.2	-80.49	-20.93	1.18
908	-43.6189	170.2029	1374309	5166648	936.052	18.00	980212.86	980292.84	-79.98	-20.38	1.18
909	-43.6189	170.2042	1374412	5166656	903	19.10	980215.69	980298.22	-82.54	-22.89	1.18
910	-43.6189	170.2054	1374511	5166656	954.688	17.60	980208.15	980289.55	-81.4	-21.72	1.18

Continued on next page

Table A.1 Continued from previous page

Station (ID)	Latitude (WGS84)	Longitude (WGS84)	Easting (NZTM)	Northing (NZTM)	Height (m)	TC (mGal)	g abs (mGal)	g boug (mGal)	g anom (mGal)	g res (mGal)	Error (mGal)
911	-43.6189	170.2066	1374607	5166658	939.924	17.30	980211.16	980292.8	-81.64	-21.91	1.18
912	-43.6188	170.2078	1374706	5166675	943.038	17.30	980210.85	980292.14	-81.29	-21.54	1.18
913	-43.6188	170.2091	1374810	5166676	922	17.80	980213.22	980295.75	-82.53	-22.73	1.18
914	-43.6187	170.2105	1374919	5166691	930.049	18.10	980215.23	980293.86	-78.63	-18.8	1.18
915	-43.6188	170.2113	1374991	5166690	936.904	18.50	980216.58	980292.1	-75.52	-15.66	1.18
916	-43.6188	170.2129	1375113	5166694	923.061	19.90	980220.23	980293.45	-73.23	-13.31	1.18
917	-43.6187	170.2141	1375214	5166700	931.683	21.40	980220.28	980290.28	-70	-10.05	1.18
918	-43.6187	170.2148	1375273	5166705	927.251	22.70	980225.29	980289.8	-64.51	-4.54	1.18
1001	-43.6148	170.1958	1373718	5167089	984.173	22.90	980210.38	980278.12	-67.74	-8.92	1.18
1002	-43.6147	170.197	1373815	5167098	974.866	21.60	980210.8	980281.17	-70.37	-11.51	1.18
1003	-43.6147	170.1982	1373918	5167104	974.101	20.90	980209.54	980282.09	-72.55	-13.65	1.18
1004	-43.6146	170.1994	1374015	5167118	969.902	19.90	980208.47	980283.92	-75.45	-16.51	1.18
1005	-43.6146	170.2007	1374117	5167121	960	19.80	980206.74	980285.96	-79.22	-20.23	1.18
1006	-43.6145	170.2019	1374216	5167138	955.673	19.50	980208.56	980287.03	-78.47	-19.46	1.18
1007	-43.6145	170.2032	1374318	5167144	944.596	19.40	980210.21	980289.34	-79.13	-20.07	1.18

Continued on next page

Table A.1 Continued from previous page

Station (ID)	Latitude (WGS84)	Longitude (WGS84)	Easting (NZTM)	Northing (NZTM)	Height (m)	TC (mGal)	g abs (mGal)	g boug (mGal)	g anom (mGal)	g res (mGal)	Error (mGal)
1008	-43.6146	170.2044	1374416	5167138	954.048	18.70	980207.84	980288.24	-80.4	-21.29	1.18
1009	-43.6144	170.2055	1374505	5167160	965.645	18.40	980206.02	980286.25	-80.23	-21.1	1.18
1010	-43.6144	170.2069	1374619	5167158	959.434	18.20	980206.79	980287.62	-80.83	-21.64	1.18
1011	-43.6144	170.2082	1374718	5167162	977.231	17.70	980203.71	980284.59	-80.88	-21.66	1.18
1012	-43.6144	170.2093	1374813	5167164	966.038	17.90	980206.6	980286.64	-80.04	-20.77	1.18
1013	-43.6144	170.2106	1374911	5167176	968.941	18.40	980207.64	980285.55	-77.91	-18.61	1.18
1014	-43.6143	170.2119	1375015	5167192	957.95	19.30	980211.64	980286.78	-75.14	-15.81	1.18
1015	-43.6141	170.213	1375110	5167210	944.249	20.70	980216.27	980288.13	-71.86	-12.51	1.18
1016	-43.614	170.2143	1375213	5167228	949.317	22.80	980219.18	980285.03	-65.85	-6.47	1.18

Appendix B

Synthetic models

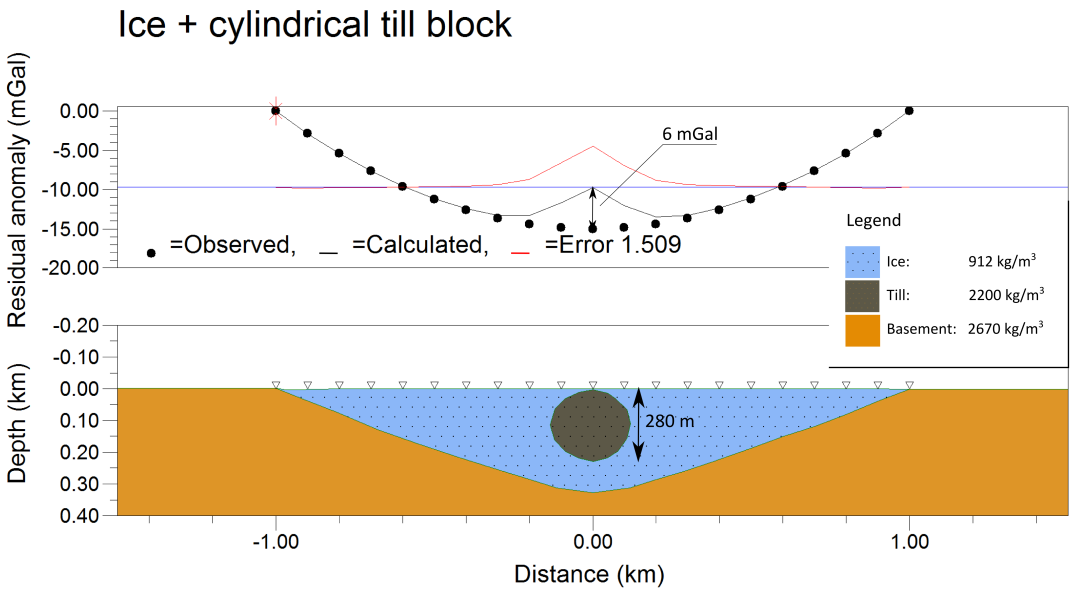

FIGURE B.1: A synthetic model demonstrates the effect a cylindrical tube has on the residual anomaly. Vertical exaggeration is 1.

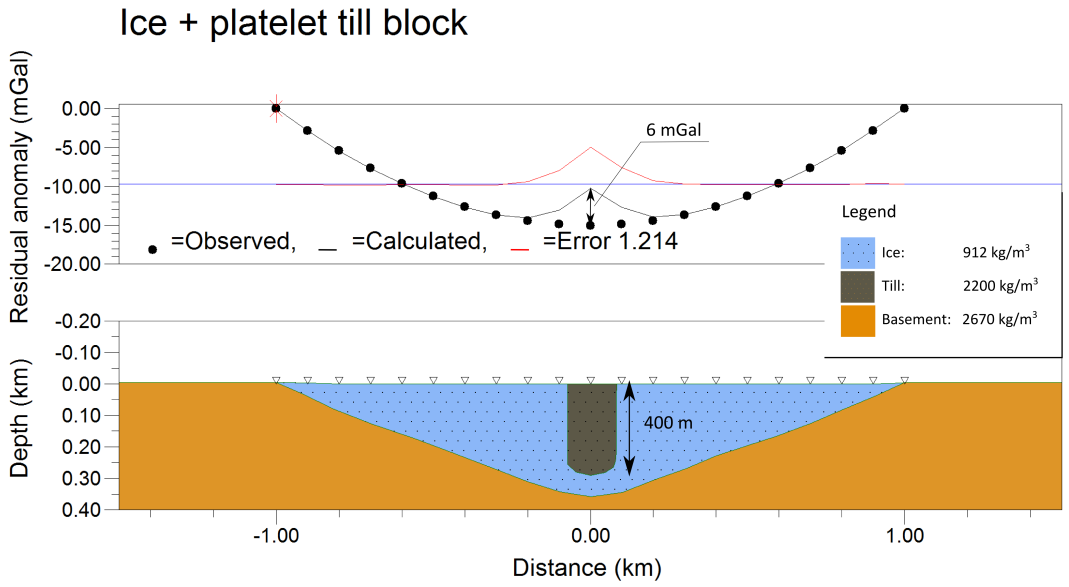

FIGURE B.2: A synthetic model demonstrates the effect a platelet structure has on the residual anomaly. Vertical exaggeration is 1.

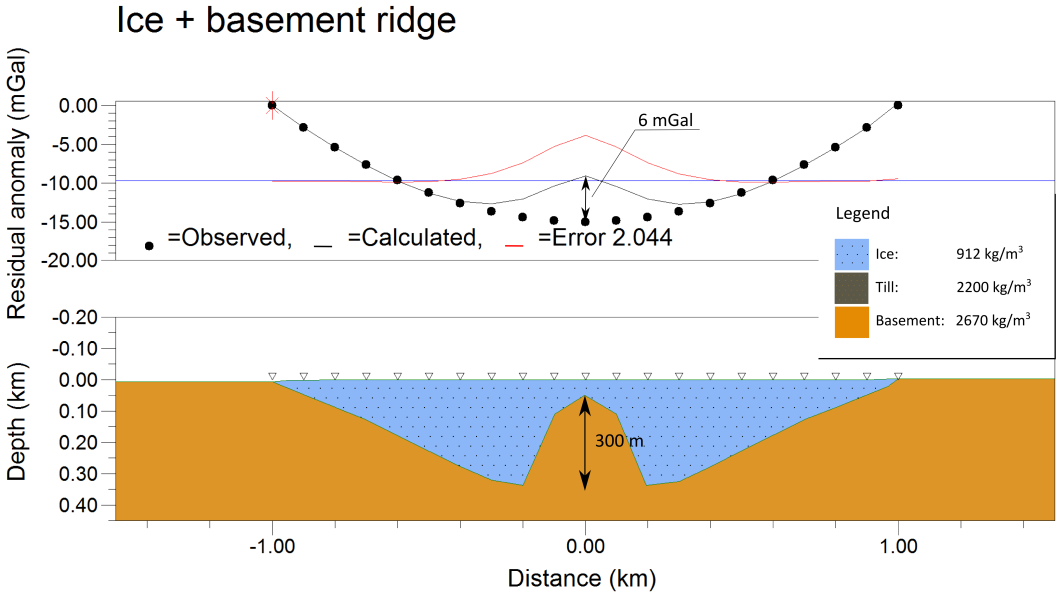

FIGURE B.3: A synthetic model demonstrates the effect a basement ridge has on the residual anomaly. Vertical exaggeration is 1.

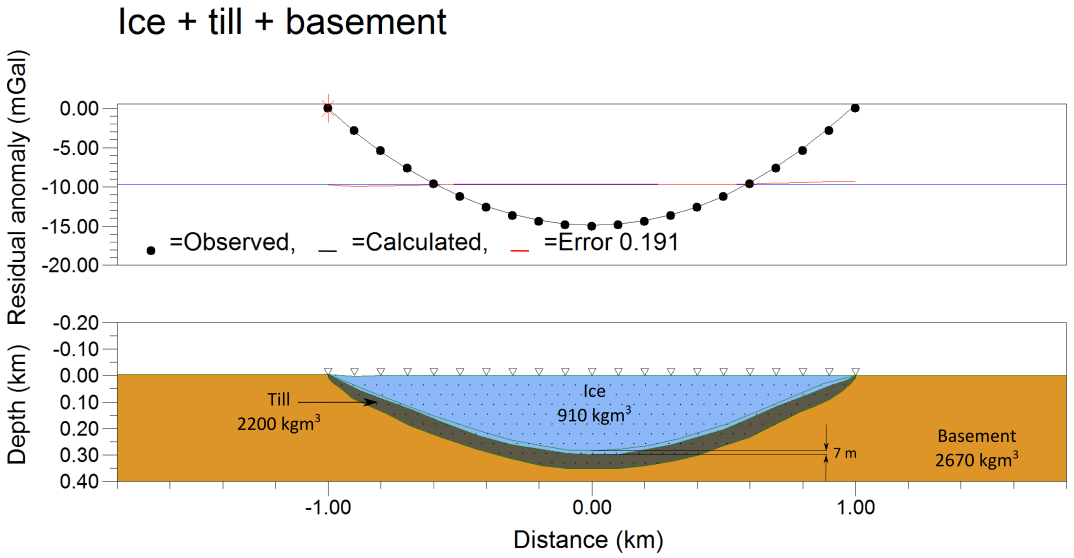

FIGURE B.4: A synthetic model demonstrates the effect of a 50 m till layer on the changes in ice-thickness. Adding a 50 m layer of till causes an decrease in ice-thickness of 7 metres in the centre of the glacier. Vertical exaggeration is 1.

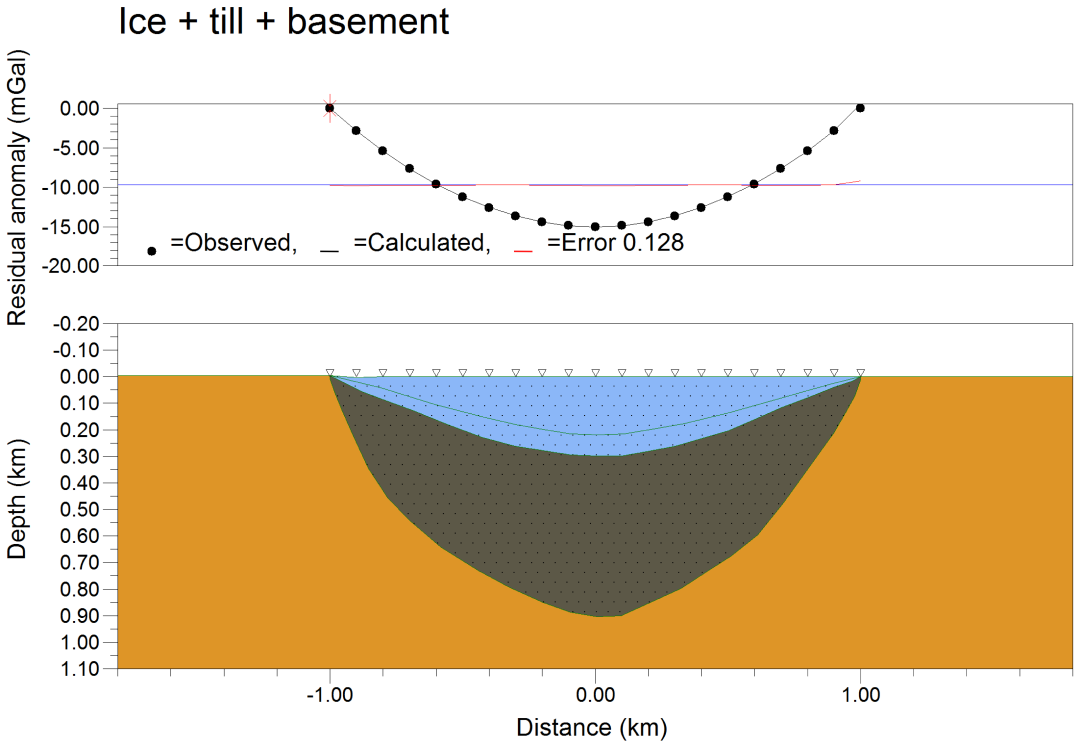

FIGURE B.5: A synthetic model demonstrates the effect of a 620 m till layer on the changes in ice-thickness. Adding a 620 m layer of till causes an decrease in ice-thickness of 71 metres in the centre of the glacier. Vertical exaggeration is 1.

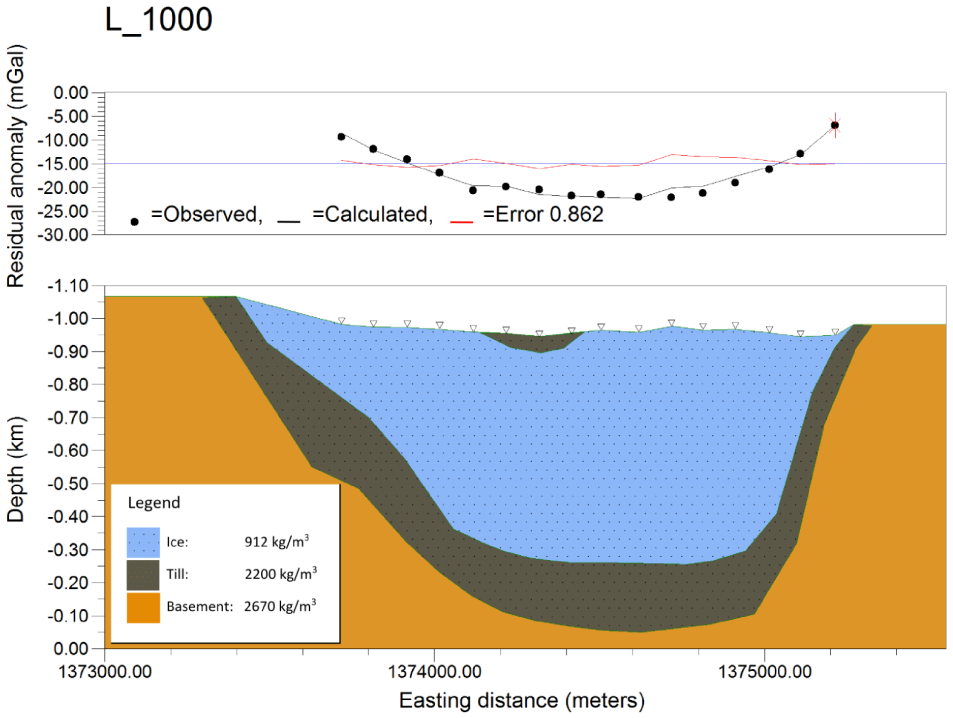

FIGURE B.6: Forward gravity model for line 1000 on the Tasman Glacier. Observed gravity is shown by black circles, calculated gravity is shown by a solid black line and the root-mean-squared error (red line) represents the difference between the observed and calculated anomalies (top inset). Vertical exaggeration is 1.

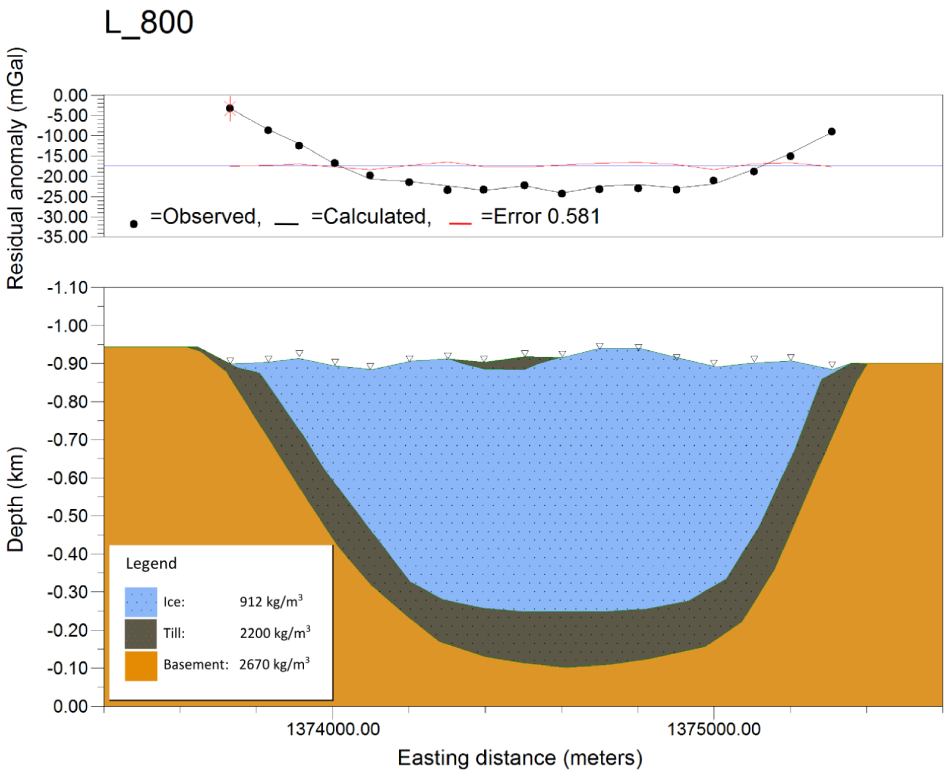

FIGURE B.7: Forward gravity model for line 800 on the Tasman Glacier. Observed gravity is shown by black circles, calculated gravity is shown by a solid black line and the root-mean-squared error (red line) represents the difference between the observed and calculated anomalies (top inset). Vertical exaggeration is 1.

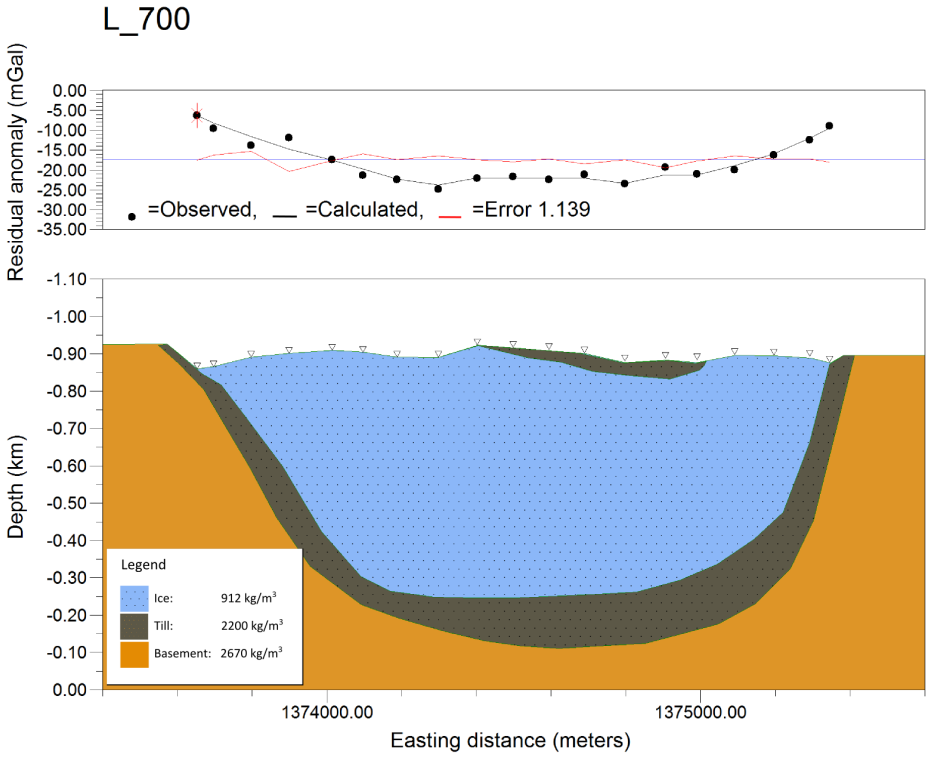

FIGURE B.8: Forward gravity model for line 700 on the Tasman Glacier. Observed gravity is shown by black circles, calculated gravity is shown by a solid black line and the root-mean-squared error (red line) represents the difference between the observed and calculated anomalies (top inset). Vertical exaggeration is 1.

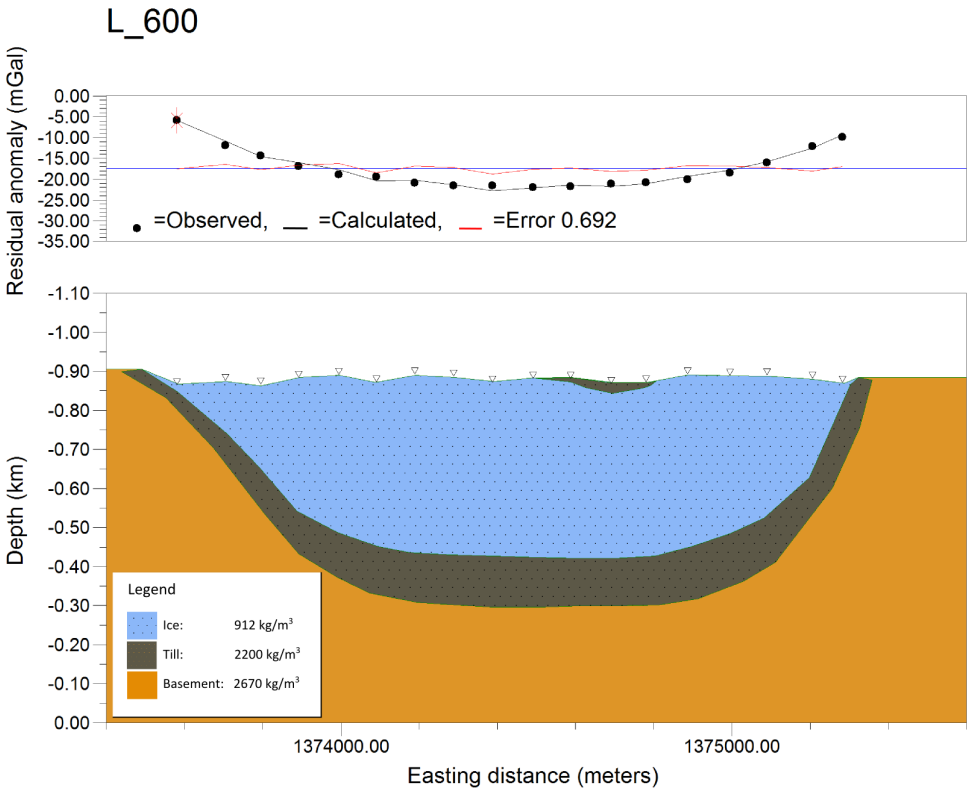

FIGURE B.9: Forward gravity model for line 600 on the Tasman Glacier. Observed gravity is shown by black circles, calculated gravity is shown by a solid black line and the root-mean-squared error (red line) represents the difference between the observed and calculated anomalies (top inset). Vertical exaggeration is 1.

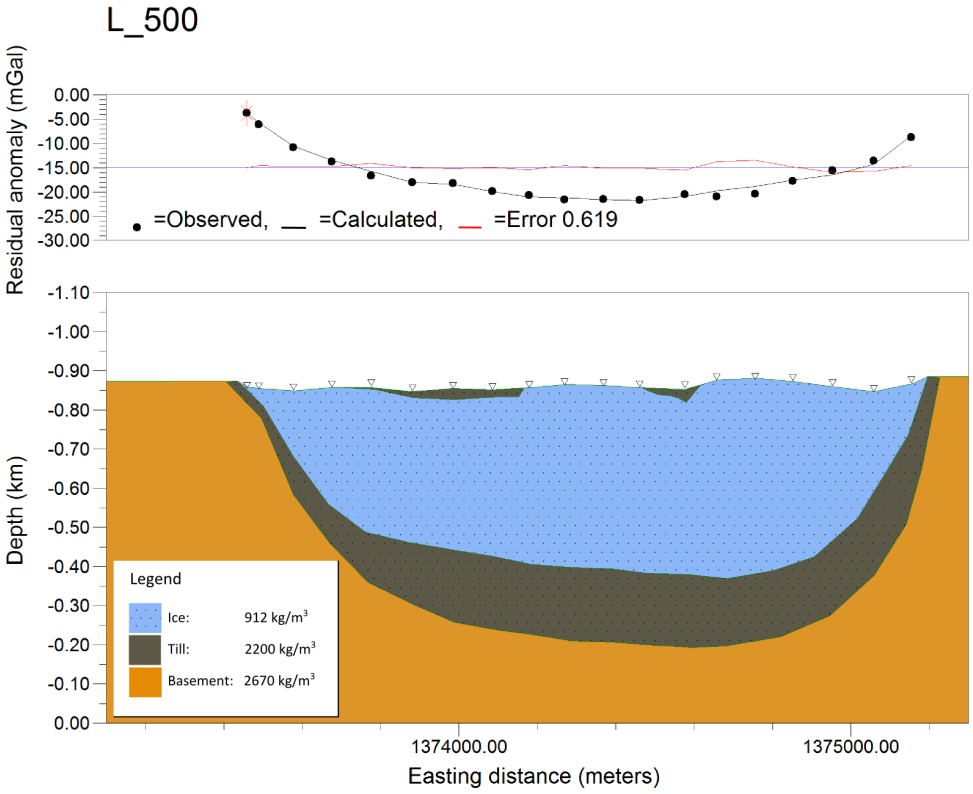

FIGURE B.10: Forward gravity model for line 500 on the Tasman Glacier. Observed gravity is shown by black circles, calculated gravity is shown by a solid black line and the root-mean-squared error (red line) represents the difference between the observed and calculated anomalies (top inset). Vertical exaggeration is 1.

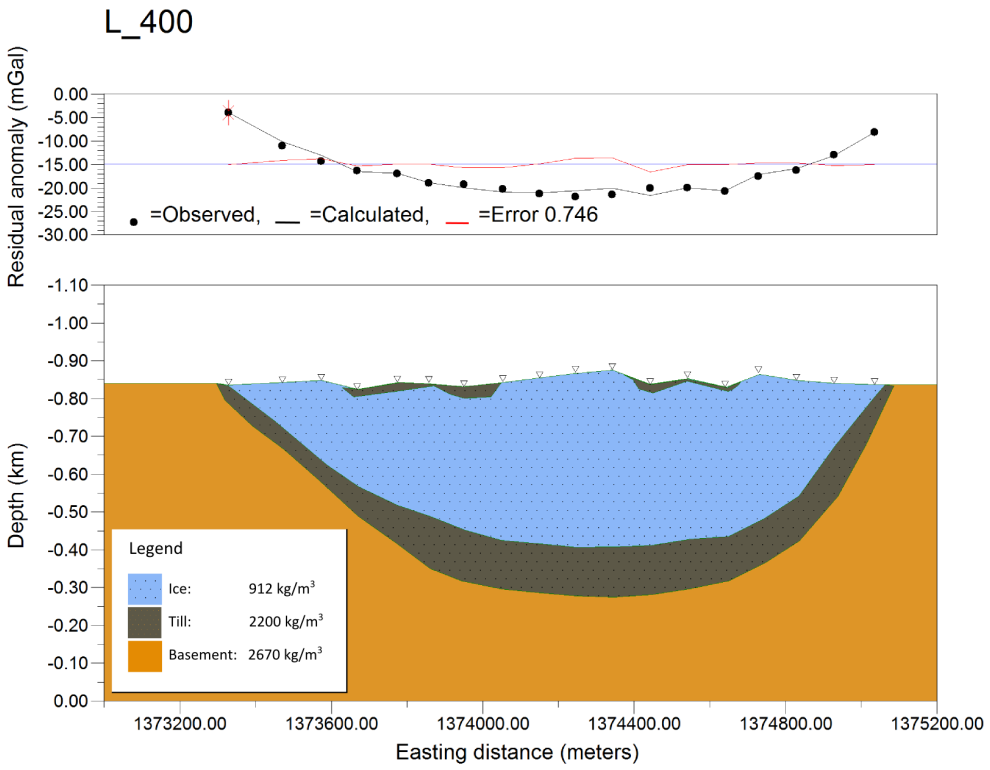

FIGURE B.11: Forward gravity model for line 400 on the Tasman Glacier. Observed gravity is shown by black circles, calculated gravity is shown by a solid black line and the root-mean-squared error (red line) represents the difference between the observed and calculated anomalies (top inset). Vertical exaggeration is 1.

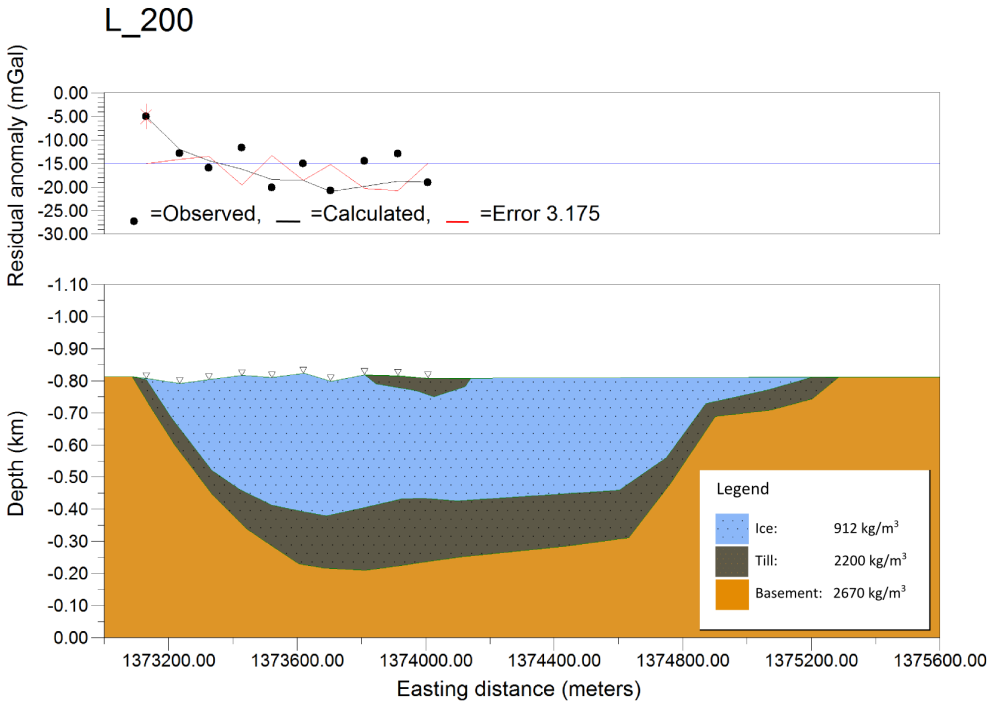

FIGURE B.12: Forward gravity model for line 200 on the Tasman Glacier. Observed gravity is shown by black circles, calculated gravity is shown by a solid black line and the root-mean-squared error (red line) represents the difference between the observed and calculated anomalies (top inset). Vertical exaggeration is 1.

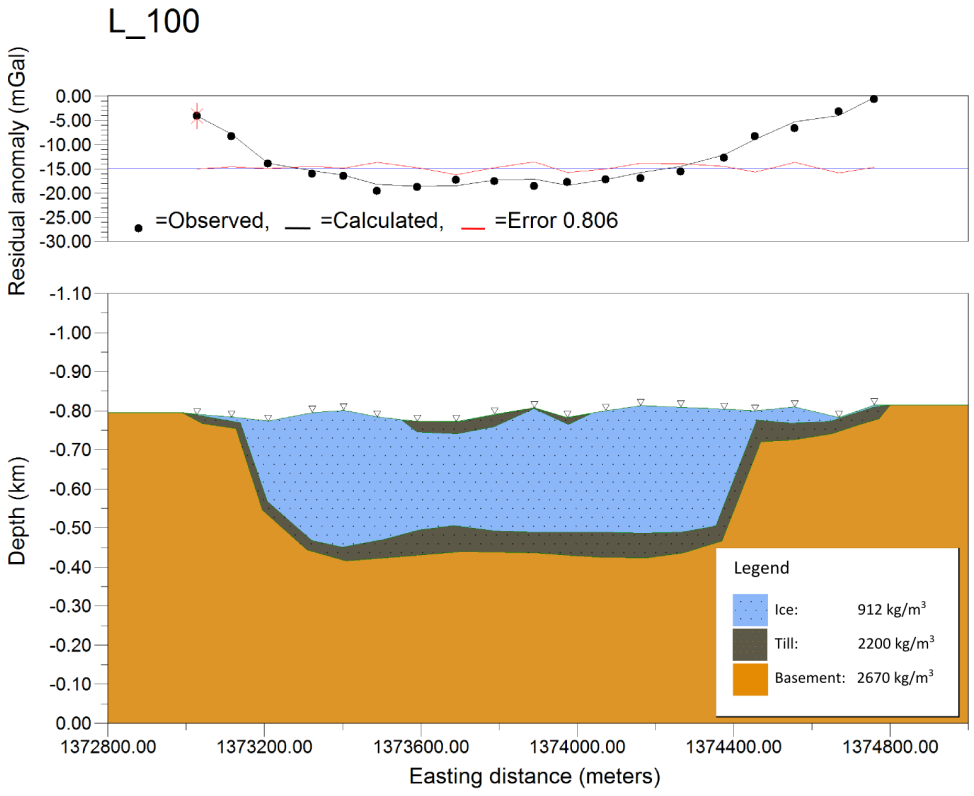

FIGURE B.13: Forward gravity model for line 100 on the Tasman Glacier. Observed gravity is shown by black circles, calculated gravity is shown by a solid black line and the root-mean-squared error (red line) represents the difference between the observed and calculated anomalies (top inset). Vertical exaggeration is 1.

References

Alley, R., Lawson, D., Larson, G., Evenson, E., and Baker, G. (2003a). Stabilizing feedbacks in glacier-bed erosion. *Nature*, 424(6950):758–760.

Alley, R. B., Allison, I., Carrasco, J., Flato, G., Fujii, Y., Kaser, G., Mote, P., Thomas, R. H., and Zhang, T. (2007). Observations: Changes in snow, ice and frozen ground. climate change 2007: The physical science basis. contribution of working group i to the fourth assessment report of the intergovernmental panel on climate change. *Cambridge University Press, Cambridge, United Kingdom and New York, NY, USA*.

Alley, R. B., Lawson, D. E., Evenson, E. B., and Larson, G. J. (2003b). Sediment, glaciohydraulic supercooling and fast glacier flow. *Annals of Glaciology*, 36:135–141.

Anderson, B. (2013). Personal communication regarding a simple mass flux model. Victoria University, Wellington.

Anderson, B. and Mackintosh, A. (2012). Controls on mass balance sensitivity of maritime glaciers in the Southern Alps, New Zealand: The role of debris cover. *Journal of Geophysical Research*, 117(F1):F01003.

Anderton, P. W. (1973). Tasman Glacier, 1971-1973. Hydrological Research: Annual Report No. 33 Ministry of Works and Development.

Arendt, A., Bolch, T., Cogley, G., Gardner, A., Hagen, J., Hock, R., Kaser, G., Paul, F., Radic, V., Bliss, A., Fountain, A., Mercer, A., Negrete, A., Giffen, B., Menounos, B., Kienholz, C., Mayer, C., Nuth, C., Burgess, D., Hall, D., Kriegel,

D., Berthier, E., Burgess, E., Cawkwell, F., Wyatt, F., Hartmann, G., Wolken, G., Frey, H., Brown, I., H. I., Lund, J., Rich, J., Filbert, K., Andreassen, L., Copland, L., Beedle, M., Koenig, M., Sharp, M., Moelg, N., Sigurdsson, O., Rastner, P., Forester, R., LeBris, R., Pettersson, R., Wheate, R., Herreid, S., Vorogushin, S., Winsvold, S., Chinn, T., Hagg, W., and Manley, W. (2012). Randolph Glacier Inventory: A dataset of Global Glacier Outlines. *Global Land Ice Measurements from Space (GLIMS), Boulder Colorado, USA, digital Media*, pages 1–35.

Bahr, D. B., Meier, F., and Peckham, S. D. (1997). The physical basis of glacier volume-area scaling. *Journal of Geophysical Research*, 102:20355–20362.

Bahr, D. B. and Radic, V. (2012). The Cryosphere Significant contribution to total mass from very small glaciers. *The Cryosphere*, 6:763–770.

Bassis, J. N. and Jacobs, S. (2013). Diverse calving patterns linked to glacier geometry. *Nature Geoscience*, 6(0):1–4.

Benn, D. I., Bolch, T., Hands, K., Gulley, J., Luckman, A., Nicholson, L. I., Quincey, D., Thompson, S., Toumi, R., and Wiseman, S. (2012). Response of debris-covered glaciers in the Mount Everest region to recent warming, and implications for outburst flood hazards. *Earth Science Reviews*, 114:156–174.

Benn, D. I., Kirkbride, M. P., Owen, L. A., and Brazier, V. (2003). *Glaciated Valley Landsystems*. A Hodder Arnold Publication.

Benn, D. I., Warren, C. R., and Mottram, R. H. (2007). Calving processes and the dynamics of calving glaciers. *Earth Science Reviews*, 82:143–179.

Bennett, G. L. and Evans, D. J. A. (2012). Glacier retreat and landform production on an overdeepened glacier foreland: the debris-charged glacial landsystem at Kvíárjökull, Iceland. *Earth Surface Processes and Landforms*, 37:1584–1602.

Bentley, R. (1973). Seismic refraction and reflection measurements at Byrd Station, Antarctica. *Journal of Glaciology*, 12(64).

Birch, F. (1961). The Velocity of Compressional Waves in Rocks to 10 Kilobars, Part 2. *Journal of Geophysical Research*, 66(7).

Booth, A. D., Mercer, A., Clark, R., Murray, T., Jansson, P., and Axtell, C. (2013). A comparison of seismic and radar methods to establish the thickness and density of glacier snow cover. *Annals of Glaciology*, 54(64):73–82.

Boulton, G. S. and Hindmarsh, R. C. A. (1987). Sediment deformation beneath glaciers: Rheology and geological consequences. *Journal of Geophysical Research*, 92:9059–9082.

Boyce, E. S., Motyka, R. J., and Truffer, M. (2007). Flotation and retreat of a lake-calving terminus, Mendenhall Glacier, southeast Alaska, USA. *Journal of Glaciology*, 53(181):211–224.

Bozhinskiy, A. N., Krass, M. S., and Popovnin, V. V. (1986). The role of debris cover in the thermal physics of glaciers. *Journal of Glaciology*, 32(I).

Broadbent, M. J. (1973). A preliminary report on the seismic and gravity surveys on the Tasman Glacier 1971-1972. Report No. 91, Geophysics Division, Department of Scientific and Industrial Research, Wellington.

Burger, H. R., Sheehan, A. F., and Jones, C. H. (2006). *Introduction to applied geophysics: Exploring the shallow subsurface*. WW Norton and Company, Inc., New York.

Chen, C. and Yue, T. (2010). A method of DEM construction and related error analysis. *Computers and Geosciences*, 36(6):717–725.

Chen, J. and Ohmura, A. (1990). Estimation of Alpine glacier water resources and their change since the 1870s. *Hydrology in mountainous regions*, (193):127–136.

Chinn, T. (2001). Distribution of the glacial water resources of New Zealand. *Journal of Hydrology*, 40(2):139–187.

Chinn, T., Fitzharris, B. B., Willsman, A., and Salinger, M. J. (2012). Annual ice volume changes 1976 – 2008 for the New Zealand Southern Alps. *Global and Planetary Change*, 92-93:105–118.

Claridge, D. (1983). A geophysical study of the termini of the Mount Cook National Park glaciers. Master's thesis, Auckland University.

Clarke, G. K. C., Berthier, E., Schoof, C. G., Jarosch, A. H., and Columbia, B. (2009). Neural Networks Applied to Estimating Subglacial Topography and Glacier Volume. *Journal of Climate*, (1997):2146–2160.

Columbus, J., Sirguey, P., and Tenzer, R. (2011). A free, fully assessed 15-m DEM for New Zealand. Survey Quarterly 66, 16-19.

Cox, S. and Barrell, D. (2007). Geology of the Aoraki area: Institute of Geological Nuclear Sciences 1:250,000 geological map.

Cox, S. C. and Findlay, R. H. (1995). The Main Divide Fault Zone and its role in formation of the Southern Alps, New Zealand. *New Zealand Journal of Geology and Geophysics*, 38(4):489–499.

Cuffey, K. and Paterson, W. (2010). *The Physics of Glaciers*. Elsevier Science Ltd, Oxford, 4th ed.

Davey, F., Eberhart-Phillips, D., Kohler, M., Bannister, S., Caldwell, G., Henrys, S., Scherwath, M., Stern, T., and van Avendonk, H. (2007). Geophysical structure of the Southern Alps orogen, South Island, New Zealand. *A Continental Plate Boundary: Tectonics at South Island, New Zealand, Geophys. Monogr. Ser*, 75.

Davies, R. (2005). Using Rob Davies terrain correction software 'TopCor'. Terrain Correction Instructions, Victoria University, Wellington.

Davy, R. (2012). Glaciotectonic processes associated with the central Alpine Fault: a gravity study of the central West Coast, South Island, New Zealand. Master's thesis, Victoria University of Wellington.

Dowdeswell, J. A., Bassford, R. P., Gorman, M. R., Williams, M., Glazovsky, A. F., Macheret, Y. Y., Shepherd, A. P., Vasilenko, Y. V., Savatyuguin, L. M.,

Hubberten, H., and Miller, H. (2002). Form and flow of the Academy of Sciences Ice Cap, Severnaya Zemlya, Russian High Arctic. *Journal of Geophysical Research*, 107.

Dykes, R. C. and Brook, M. S. (2010). Terminus recession, proglacial lake expansion and 21st century calving retreat of Tasman Glacier, New Zealand. *New Zealand Geographer*, 66(3):203–217.

Dykes, R. C., Brook, M. S., and Winkler, S. (2010). The contemporary retreat of Tasman Glacier, Southern Alps, New Zealand, and the evolution of Tasman proglacial Lake since AD 2000. *Erdkunde*, 2010(2):141–154.

Farinotti, D. and Huss, M. (2013). An upper-bound estimate for the accuracy of volume-area scaling. *The Cryosphere*, 7:2293–2331.

Farinotti, D., Huss, M., Bauder, A., Funk, M., and Truffer, M. (2009). A method to estimate the ice volume and ice-thickness distribution of alpine glaciers. *Journal of Glaciology*, 55(191):422–430.

Fowler, C. (2005). *The Solid Earth: An Introduction to Global Geophysics*. Cambridge University Press.

Gardner, G., Gardner, L., and Gregory, A. (1974). Formation velocity and density - The diagnostic basis for stratigraphic traps. *Geophysics*, 39(6):770–780.

Glen, J. W. (1955). The creep of polycrystalline ice. *Proceedings of the Royal Society of London. Series A. Mathematical and Physical Sciences*, 228(1175):519–538.

Grinsted, A. (2013). An estimate of global glacier volume. *The Cryosphere*, 7:141–151.

Hambrey, M. J. and Glasser, N. F. (1978). Glacial sediments: Processes, environments and facies. In *Sedimentology*, Encyclopedia of Earth Science, pages 513–531. Springer Berlin Heidelberg.

Hammer, S. (1938). Terrain corrections for gravimeter stations. *Geophysics*, 4:184–194.

Hinze, W. J. (2003). Bouguer reduction density, why 2.67? *Geophysics*, 68(5):1559–1560.

Hirano, M. and Aniya, M. (1988). A rational explanation of cross-profile morphology for glacial valleys and of glacial valley development. *Earth Surface Processes and Landforms*, 13(8):707–716.

Hochstein, M. P., Claridge, D., Leary, S. F., Henrys, S. A., Pyne, A., and David, C. (1995). Downwasting of the Tasman Glacier, South Island, New Zealand: Changes in the terminus region between 1971 and 1993. *New Zealand Journal of Geology and Geophysics*, 38:37–41.

Huss, M. and Farinotti, D. (2012). Distributed ice thickness and volume of all glaciers around the globe. *Journal of Geophysical Research*, 117:1–10.

Huss, M., Farinotti, D., Bauder, A., and Funk, M. (2008). Modelling runoff from highly glacierized alpine drainage basins in a changing climate. *Hydrological Processes*, 22(19):3888–3902.

Jansson, P. and Iiolmlund, P. (2000). Debris entrainment and polythermal structure in the terminus of Storglaciàren. *IAHS Publication*, (264):143–152.

King, E. C. and Jarvis, E. P. (2007). Use of Shear Waves to Measure Poisson's Ratio in Polar Firn. *Journal of Environmental and Engineering Geophysics*, 12:15–21.

Kirkbride, M. P. (1993). The temporal significance of transitions from melting to calving termini at glaciers in the central Southern Alps of New Zealand. *The Holocene*, 3(3):232–240.

Kirkbride, M. P. and Warren, C. R. (1999). Tasman Glacier, New Zealand: 20th-century thinning and predicted calving retreat. *Global and Planetary Change*, 22:11–28.

Kleffmann, S., Davey, F., Melhuish, A., Okaya, D., and Stern, T. (1998). Crustal structure in the central South Island, New Zealand, from the Lake Pukaki seismic experiment South Island - New Zealand. *New Zealand Journal of Geology and Geophysics*, 41:39–49.

Leclercq, P. W., Oerlemans, J., and Cogley, J. G. (2011). Estimating the Glacier Contribution to Sea-Level Rise for the Period 1800–2005. *Surveys in Geophysics*, 32(4-5):519–535.

Li, H., Ng, F., Li, Z., Qin, D., and Cheng, G. (2012). An extended "perfect-plasticity" method for estimating ice thickness along the flow line of mountain glaciers. *Journal of Geophysical Research*, 117:1–11.

McSaveney, M. (2002). *Recent rockfalls and rock avalanches in Mount Cook National Park, New Zealand*, volume 15. Reviews in Engineering Geology XV. Geological Society of America.

Meier, M. F., Dyurgerov, M. B., Rick, U. K., O'Neel, S., Pfeffer, W. T., Anderson, R. S., Anderson, S. P., and Glazovsky, A. F. (2007). Glaciers Dominate Eustatic Sea-Level rise in the 21st century. *Science*, 317(5841):1064–1066.

Mercer, J. H. (1961). The response of fjord glaciers to changes in the firn limit. *Journal of Glaciology*, 3(29):850–858.

Mishra, D. (2011). *Gravity and Magnetic Methods for Geological Studies: Principles, Integrated Exploration and Plate Tectonics*. BS Publications.

Montgomery, D. R. (2002). Valley formation by fluvial and glacial erosion. *Geology*, 30(11):1047–1050.

Nobes, D. C., Leary, S., Hochstein, M., and Henry, S. (1994). Ground-penetrating radar profiles of rubble-covered temperate glaciers: Results from the Tasman and Mueller glaciers of the Southern Alps of New Zealand. In *Annual meeting of the Society of Exploration Geophysicists*, volume 64, pages 826–829.

Nolan, M., Motkya, R. J., Echelmeyer, K., and Trabant, D. E. C. (1995). Ice-thickness measurements of Taku Glacier, Alaska, U.S.A., and their relevance to its retreat behaviour. *Journal of Glaciology*, 41(139):541–553.

Norris, R. J. and Cooper, A. F. (2001). Late Quaternary slip rates and slip partitioning on the Alpine Fault, New Zealand. *Journal of Structural Geology*, 23(2000):507–520.

Nye, B. J. F. (1952). The mechanics of glacier flow. *Journal of Glaciology*, 2(12):82–93.

Oerlemans, J., Anderson, B., Hubbard, A., Huybrechts, P., Jóhannesson, T., Knap, W. H., Schmeits, M., Stroeven, A. P., van de Wal, R. S. W., Wallinga, J., and Zuo, Z. (1998). Modelling the response of glaciers to climate warming. *Climate Dynamics*, 14(4):267–274.

Owens, I. F. (1992). A Note on the Mount Cook Rock Avalanche of 14 December 1991. *New Zealand Geographer*, 48(2):74–78.

Purdie, J. and Fitzharris, B. (1999). Processes and rates of ice loss at the terminus of Tasman Glacier, New Zealand. *Global and Planetary Change*, 22:79–91.

Quincey, D. J. and Glasser, N. F. (2009). Morphological and ice-dynamical changes on the Tasman Glacier, New Zealand, 1990—2007. *Global and Planetary Change*, 68(3):185–197.

Radić, V. and Hock, R. (2010). Regional and global volumes of glaciers derived from statistical upscaling of glacier inventory data. *Journal of Geophysical Research*, 115:1–10.

Rattenbury, M., Jongens, R., and Cox, S. (2010). Geology of the Haast area, Institute of Geological and Nuclear Sciences, scale 1:250,000, geological map.

Redpath, T. A. N. (2011). Utilising Optical Satellite Imagery to derive Multi-Temporal Flow Fields for the Tasman Glacier. Master's thesis, Otago University.

Redpath, T. A. N., Sirguey, P., Fitzsimons, S. J., and Kääb, A. (2013). Remote Sensing of Environment Accuracy assessment for mapping glacier flow velocity and detecting flow dynamics from ASTER satellite imagery: Tasman Glacier, New Zealand. *Remote Sensing of Environment*, 133:90–101.

Rege, R. B. and Godio, A. (2011). Geophysical investigation for mechanical properties of a glacier. In *Geophysical Research Abstracts*, volume 13.

Reid, T. D., Carenzo, M., Pellicciotti, F., and Brock, B. W. (2012). Including debris cover effects in a distributed model of glacier ablation. *Journal of Geophysical Research*, 117:1–15.

Reilly, W. (1972). New Zealand gravity map series. *New Zealand Journal of Geology and Geophysics*, 15(1):3–15.

Reynolds, J. (2011). *An Introduction to Applied and Environmental Geophysics*. Wiley.

Röhl, K. (2006). Thermo-erosional notch development at fresh-water-calving Tasman Glacier, New Zealand. *Journal of Glaciology*, 52(177):203–213.

Röhl, K. (2008). Characteristics and evolution of supraglacial ponds on debris-covered Tasman Glacier, New Zealand. *Journal of Glaciology*, 54(188):867–880.

Schrott, L. and Sass, O. (2008). Application of field geophysics in geomorphology: Advances and limitations exemplified by case studies. *Geomorphology*, 93(1–2):55 – 73.

Skinner, B. E. (1964). New Zealand Journal of Geology and Geophysics Measurement of Twentieth Century Ice Loss on the Tasman Glacier, New Zealand. *New Zealand Journal of Geology and Geophysics*, 7(4):796–803.

Stein, S. and Wysession, M. (2003). *An Introduction to Seismology, Earthquakes, and Earth Structure*. Wiley.

Stern, T. (1978). *Gravity Survey of the Taylor Glacier, Victoria Land, Antarctica*. Antarctic data series. Victoria University of Wellington.

Sturman, A. and Tapper, N. (2006). *The Weather And Climate Of Australia And New Zealand*. Oxford University Press.

Talwani, M., Worzel, J. L., and Landisman, M. (1959). Rapid gravity computations for two-dimensional bodies with application to the mendocino submarine fracture zone. *Journal of Geophysical Research*, 64(1):49–59.

Taylor, B. (1717). *Methodus incrementorum directa et inversa*. Impensis Gulielmi Innys.

Taylor, J. (1997). *An Introduction to Error Analysis: The Study of Uncertainties in Physical Measurements*. 2nd ed. University Science Books, USA.

Tenzer, R., Sirguey, P., Rattenbury, M., and Nicolson, J. (2011). A digital rock density map of New Zealand. *Computers & Geosciences*, 37(8):1181–1191.

Van der Veen, C. J. (2002). Calving glaciers. *Progress in Physical Geography*, 26(1):96–122.

Vivero, S., Sirguey, P., Fitzsimons, S. J., Strong, D., and Soruco, A. (2013). Recent Ice Wastage on the Tasman Glacier Obtained from Geodetic Elevation Changes. Master's thesis, University of Otago.

Walcott, R. I. (1998). Modes of oblique compression: Late Cenozoic tectonics of the South Island of New Zealand. *Reviews of Geophysics*, 36(1):1–26.

Warren, C. R. (1991). Terminal environment, topographic control and fluctuations of West Greenland glaciers. *Boreas*, 20(1):1–15.

Warren, C. R. and Glasser, N. F. (1992). Contrasting Response of South Greenland Glaciers to Recent Climatic Change. *Arctic and Alpine Research*, 24(2):124–132.

Watson, M. (1995). Geophysical and Glaciological Studies of the Tasman and Mueller Glaciers. Master's thesis, University of Auckland.

Yde, J. C. and Paasche, O. (2010). Reconstructing Climate Change: Not All Glaciers Suitable. *Eos*, 91(21):189–190.